NOTICE

The quality of this microform is heavily dependent upon the quality of the original thesis submitted for microfilming. Every effort has been made to ensure the highest quality of reproduction possible.

If pages are missing, contact the university which granted the degree.

Some pages may have indistinct print especially if the original pages were typed with a poor typewriter ribbon or if the university sent us an inferior photocopy.

Reproduction in full or in part of this microform is governed by the Canadian Copyright Act, R.S.C. 1970, c. C-30, and subsequent amendments.

AVIS

La qualité de cette microforme dépend grandement de la qualité de la thèse soumise au microfilmage. Nous avons tout fait pour assurer une qualité supérieure de reproduction.

S'il manque des pages, veuillez communiquer avec l'université qui a conféré le grade.

La qualité d'impression de certaines pages peut laisser à désirer, surtout si les pages originales ont été dactylographiées à l'aide d'un ruban usé ou si l'université nous a fait parvenir une photocopie de qualité inférieure.

La reproduction, même partielle, de cette microforme est soumise à la Loi canadienne sur le droit d'auteur, SRC 1970, c. C-30, et ses amendements subséquents.

ANALYSIS OF HF ANTENNAS ON A HELICOPTER BY SCALE-MODEL MEASUREMENTS AND COMPUTER MODELLING

Shahram Esfandiari

A THESIS

IN

THE FACULTY

OF

ENGINEERING

AND

COMPUTER SCIENCE

Presented in Partial Fulfilment of the Requirements
for the degree of Master of Applied Science at
Concordia University
Montreal, Quebec, Canada

March 1992

ISBN 0-315-73633-X

ABSTRACT

ANALYSIS OF HF ANTENNAS ON A HELICOPTER BY SCALE-MODEL MEASUREMENTS AND COMPUTER MODELLING

Shahram Esfandiari

HF shorted loop (Tranline) and open-ended wire antenna (Zig-Zag) installations on BELL CH-135 helicopter are described. Numerical models of both antennas are developed and guidelines used in model development are mentioned. The Numerical Electromagnetic Code (NEC) is employed to obtain input impedance and radiation characteristics of the antenna/airframe system. Scale model measurements of the system radiation patterns are carried out. Power related performance parameters, which are computed from the radiation patterns, are used to arrive at a meaningful evaluation of antenna performance. They are also employed to compare the measured and computed data in order to obtain a validated computer model. The predictions of the numerical model exhibit a fair degree of consistency with measured results. Since HF communication of a helicopter is influenced by its rotor modulation, the rotor effects for both installations are discussed. The effects of variation in height and ground parameters are mentioned. Modes of longitudinal resonances are identified on the airframe. The results of a brief comparison between zig-zag and tranline antennas are given.

ACKNOWLEDGMENTS

I wish to thank my supervisor Dr. S. J. Kubina for his continuous encouragement and support throughout this work. I also wish to thank DR. R. Paknys for his patience and informative discussions which greatly contributed to this work. I appreciate the efforts of Mike Marak and David Guadine in maintaining the EMC Laboratory facilities which made this work possible.

The greatest contributors to this work however, are my parents. Their vision, understanding and devotion have always been and always will be a great source of inspiration to me. I therefore dedicate this work to my parents.

TABLE OF CONTENTS

LIST OF SYMBOLS

E^p	Primary field
E^s	Secondary field
β	Phase constant or wave number
g_n	Basis function
G	Free space Green's function
W_m	Weighting function
a	Wire radius
l	Wire length
η	Intrinsic impedane
λ	Wave length
Δ	Segment length
γ	Euler's constant
E_ϕ	Horizontal component of radiated field
E_θ	Vertical component of radiated field
η_p	Radiation pattern efficiency
$\%E_\theta$	Percentage of E_θ power
SUB-$\%E_\theta$	Percentage of useful E_θ power
σ	Conductivity
R_v	Vertical reflection coefficient
R_h	Horizontal reflection coefficient

LIST OF TABLES

LIST OF FIGURES

CHAPTER 1

INTRODUCTION

There are several reasons why the subject of aircraft HF antennas merits discussion separately from the general subject of antennas[1]. An airborne transmitting antenna installed on an airframe tends to excite a system of RF currents on the conducting surface of the aircraft whenever major dimensions of the airframe are comparable with the operating wavelength. These currents determine the performance of an antenna by influencing its impedance and radiation pattern. Therefore, to determine the electromagnetic response of an antenna in the HF band, (2 to 30 MHz), the entire aircraft must be considered as a radiating structure.

The radiation patterns of an airborne antenna may either be obtained through measurements or by numerical computations. Measurements may be performed either on a scale model of the aircraft, or on the actual aircraft. The numerical computations are performed on a three dimensional computer model of the aircraft.

1.1 Computer Model

Generating a wire grid computer model of an aircraft is accomplished by first dividing the surface of the airframe into imaginary rectangular or triangular surface patches. These patches are then represented by an equivalent grid of "thin wires" and hence a wire grid model of the aircraft is created. The antenna is represented by a wire of corresponding length and radius. In constructing a wire grid model, certain rules, known as modelling guidelines, must be obeyed so that the current on the wire grid meshes simulate the local variations in surface current density, i.e. the model represents an electromagnetic approximation of the airframe's continuous surface. A numerical method, known as the Moment Method[2], utilizes the Electric Field Integral Equation (EFIE) to find the current distribution on the airframe and the resulting radiated field.

The advantages of using a computer model, over experimental measurements, in obtaining information regarding the electromagnetic behavior of the aircraft, as a radiating structure, are numerous. With the recent advances in digital computers, calculating the radiation pattern characteristics of an airborne antenna including the magnitude and phase of the RF current on the airframe

is accomplished in a few minutes, if not seconds. Extensive measurements on the other hand, are time consuming, very costly, and often very difficult. For instance, unlike the computer model, it is not an easy task to measure the electromagnetic response of an aircraft to varying certain parameters such as, antenna location and ground properties.

A computer model however, does not eliminate the need for some measurements. This is due to the fact that the numerical and physical credibility of the computed results must be determined, i.e. the model must be validated[14]. Model validation involves comparing the numerical results to either full scale or scale model measurements.

1.2 Scale Model Measurements

Scale models of HF airborne antennas are often used to investigate the properties of such antennas and have proven to be reliable replacements for costly full scale measurements. The possibility of constructing a model of a given electromagnetic system is a direct consequence of the linearity of Maxwell's equations[34,36]. A scale model is derived from a full scale system by dividing all dimensions of the latter by a constant scale factor, ρ. The relation between scale model and full scale quantities

are given in Chapter 3.

As a direct consequence of the reciprocity theorem, radiation pattern measurements may be made under either transmitting or receiving conditions[36]. Radiation patterns of BELL CH-135 were measured at the National Research Council under transmitting condition by placing a battery-operated oscillator inside the scale model. The model was then mounted on a tower and the radiated field was detected by a receiving antenna oriented to measure the desired polarization, as shown in Figure 3-7.

1.3 Previous Work And Objective

An old wire grid model of the BELL CH-135 helicopter, which was developed at the Electromagnetic Compatibility Laboratory, had certain deficiencies which made its validation doubtful over the HF frequency range. The discrepancies between the measured and computed results in the 6 to 10 MHz region, which is of great importance to helicopter HF communication, were of some concern. It therefore became the first objective of this thesis to develop a valid wire grid computer model of BELL CH-135 Twin/Huey helicopter. The validated model was then used for a systematic study of the effect of ground parameters and height above ground on the radiation patterns of the

antennas being modelled.

Subsequently the model was used for a detailed examination of the variation of radiation patterns and current distributions with frequency. Here it was possible to identify possible modes of longitudinal resonances on the airframe. A part of this analysis also included comparisons of measured and computed input impedances of the antennas being modelled. The model was further used to study the effect of rotor modulation on HF communication of a helicopter.

Finally the results were used for a comparison of the communication system performance parameters of the two antennas, the Tranline or shorted transmission line and the "Zig-Zag". This comprehensive analysis has revealed important aspects of HF antenna performance on helicopters that have herebefore not been reported elsewhere.

CHAPTER 2

MOMENT METHODS

In the study of antenna theory, a knowledge of current distribution is of fundamental importance. The performance of an aircraft antenna is influenced by the currents induced on the airframe. In particular at HF frequencies where the aircraft is small in terms of wavelength, the entire structure acts as a radiator or antenna and it is desirable to be able to predict the antenna performance so that the design may be optimized.

Although, due to the complexity of the structure, exact analysis of the interaction between antenna and aircraft is impossible, current distribution data may be obtained in two different ways. First by means of scale model measurements, which were and still remain one of the main sources of design information. Secondly the use of approximate techniques, which are made possible with the advancement of computers. One of such techniques, which often employ numerical methods, is called the moment method. This method is associated with the solution of an

integral equation technique which casts the solution for the induced current in the form of an integral equation where the unknown induced current density is part of the integrand. The moment method procedure produces a solution for the current density. Then the fields scattered by the structure can be found using the traditional radiation integrals [1,2].

2.1 Integral Equations

Most radiation problems in electromagnetic scattering of thin wires may be expressed as an integral equation of the general form shown in (1)

$$\int I(z') K(z,z')\, dz' = -E^i(z) \tag{1}$$

with an inhomogeneous source term on the right and the unknown within the integral[3]. Two classic integral equations in electromagnetics, namely Pocklington's and Hallen's and their derivatives are demonstrated in the following section.

2.1.1 Pocklington's Integral Equation

One of the most useful equations to find the current distribution on a cylindrical wire was derived by Pocklington. Although this equation is derived for wires

with a finite diameter, certain restrictions apply to the physical size of the wire. These restrictions or so called "thin-wire" approximation require that the radius of the wire be much less than the wavelength[4], and still not be infinitesimally thin. This implies that the current on the wire be negligible in the direction of azimuthal angle ϕ, that the current density be almost uniform in the axial direction and tangential component of the total field would also be taken along the axial direction. Shown in Figure 2-1 is a wire of radius a and length 1, lined up along the z axis. The wire is subjected to a primary or excitation field which is either an incoming plane wave or caused by a voltage source feeding the wire. This field induces a current density which in turn radiates what is known as a secondary or induced field[5,6]. Considering a free space condition, with no magnetic current, Lorentz gauges yields;

$$\bar{\nabla}.\bar{A}=-j\omega\mu_{o}\varepsilon_{o}V \qquad (2)$$

where V and $\bar{A}$ are scalar and vector potentials respectively. The field intensity also may be expressed as:

$$\bar{E}=-j\omega\bar{A}-\bar{\nabla}V \qquad (3)$$

Now as a result of the thin wire approximation all electric

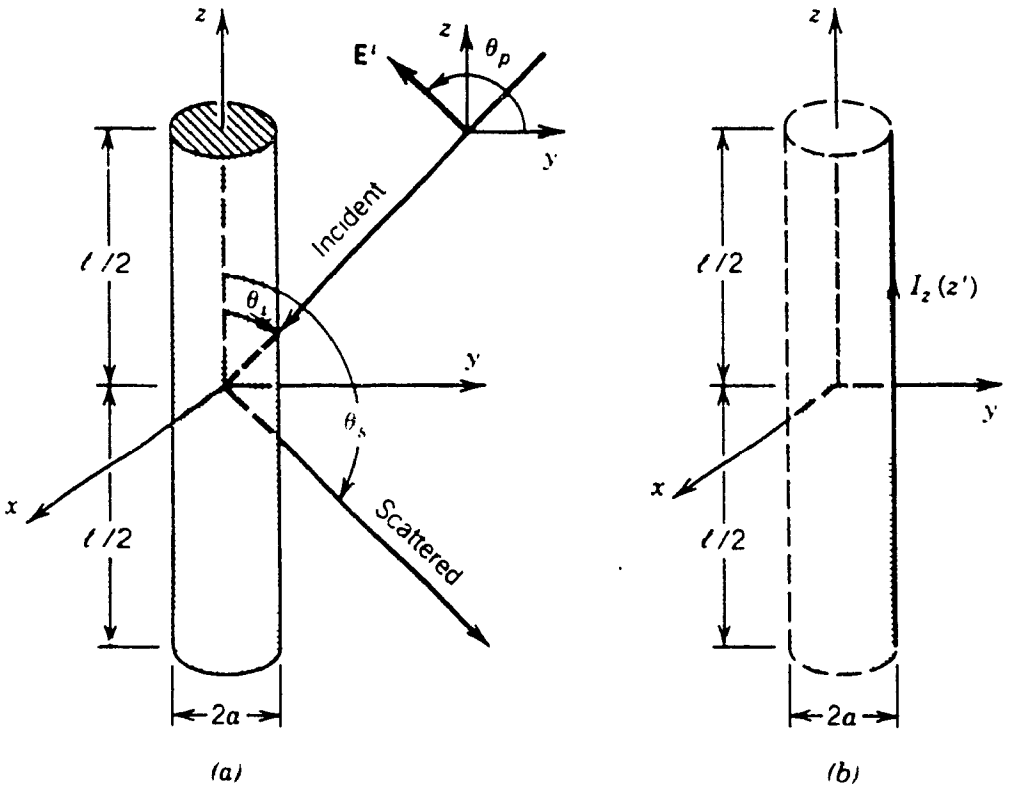

Figure 2-1 (a)Uniform plane wave obliquely incident on a conducting wire and (b) equivalent current[1].

currents are considered to be in the z direction and hence;

$$\frac{\partial A_z}{\partial Z} = -j\omega\mu_0\varepsilon_0 V \qquad (4)$$

and from eqn.(3) we have

$$E_z = -j\omega A_z - \frac{\partial V}{\partial Z} \qquad (5)$$

substituting eqn.(4) in (5) yields

$$E_z = -j\omega A_z + \frac{1}{j\omega\mu_o\varepsilon_o}\frac{\partial^2 A_z}{\partial Z^2} \tag{6}$$

by enforcing the boundary condition, which requires the tangential component to vanish at the surface of a conductor, we get;

$$E_t^p(\rho=a) + E_t^s(\rho=a) = 0 \tag{7}$$

$$E_t^s(\rho=a) = E_z^s(\rho=a) = -E_z^p(\rho=a) \tag{8}$$

where the tangential components of both primary and secondary fields are in the axial direction. If one considers a current element J dV′, then[7]

$$A_z = \mu\iiint \frac{J_z(x', y', z')\, e^{-j\beta r}}{4\pi r} dV' \tag{9}$$

where source coordinates are primed and $\beta^2 = \omega^2\mu_o\varepsilon_o$. As assumed before, for a thin wire the current density J_z is in the axial direction, hence

$$J_z = \frac{I_z(z')}{2\pi a} \tag{10}$$

employing (8), (9) and (10) in (6)

$$\frac{1}{j\omega\varepsilon_o}\iiint \left[\frac{\partial^2 G(z, z')}{\partial Z^2} + \beta^2 G(z, z')\right]\frac{I_z(Z')}{2\pi a} dV' = -E_z^p(\rho) \tag{11}$$

where G(z,z′) is free space Green's function[3], given as

$$G(z, z') = \frac{e^{-j\beta r}}{4\pi r} \tag{12}$$

and r is the distance between observation point (unprimed)

and the source point, or

$$r=\sqrt{(x-x')^2+(y-y')^2+(z-z')^2} \tag{13}$$

Now assuming that the current is restricted to the surface of the wire, with radius a, eqn.(11) reduces to a double integral. Furthermore, if a << λ (which is a consequence of the thin wire approximation), there would be uniform axial distribution. The surface current distribution may now be replaced by an equivalent filamentary line source which is located a radial distance "a" from the observation point on the wire axis , as shown in Figure 2-1(b). This would further reduce eqn.(11) to

$$\int_{-\frac{l}{2}}^{\frac{l}{2}} I(z')\left[\frac{\partial^2 G(z,z')}{\partial z^2}+\beta^2 G(z,z')\right]dz'=-j\omega\varepsilon.E_z^p(\rho=a) \tag{14}$$

where r in eqn.(12) is now defined as:

$$r=\sqrt{(z-z')^2+a^2} \tag{15}$$

Equation (14) is the type of integral equation derived by Pocklington and may be used to find the equivalent filamentary line-source current of the wire. This knowledge could then be used to find the current density once the primary field is known[1].

2.1.2 Hallen's Integral Equation

Another classic three-dimensional integral equation

used to solve for current distribution on conducting wires is Hallen's equation. Unlike Pocklington's approach, which incorporated the boundary conditions in the integral equation itself, Hallen's method uses the usual differential equation approach. That is, the independent variable ranges over all space with a solution being sought to the differential equation that satisfies the boundary conditions[8]. Referring again to Figure 2-1a, we assume that the length of the wire l is much larger than the radius a ($l >> a$) and the radius is much smaller than the wavelength λ ($a << \lambda$), so that the end effects may be neglected[1]. Therefore, the boundary conditions are; i) The total tangential component of the electric field at the surface of the wire approaches zero, and ii) The current at both ends of the wire approaches zero, i.e.; $[I_z(z' = l/2)=0]$ [1].

As in the previous section, the electric current density only has an axial component which gives rise to the vector potential having only a Z component. Enforcing the electric field boundary condition on the surface of a perfectly conducting cylinder, we get

$$[\frac{d^2}{dz^2}+\beta^2]A_z(z)=0 \qquad (16)$$

which is the one dimensional wave equation. Considering the symmetrical condition of a current density on a

dipole[8]

$$J_z(-z) = J_z(z) \tag{17}$$

and therefore

$$A_z(z') = A_z(-z') \tag{18}$$

Thus the solution of eqn.(16) is given by

$$A_z(z) = -j\sqrt{\mu\varepsilon}\,[C_1\cos(\beta z) + C_2\sin(\beta|z|)] \tag{19}$$

where C_1 and C_2 are arbitrary constants. For a perfectly conducting thin wire, the potential is given as;

$$A_z(z) = \mu_\circ \int_{-\frac{l}{2}}^{\frac{l}{2}} I_z(z')\,G(z,z')\,dz' \tag{20}$$

where G(z,z´) is given by eqn.(12) and r by eqn.(15). Equating eqns.(19) and (20)

$$\int_{-\frac{l}{2}}^{\frac{l}{2}} I_z(z')\,G(z,z')\,dz' = -j\sqrt{\frac{\varepsilon_\circ}{\mu_\circ}}\,[C_1\cos(\beta z) + C_2\sin(\beta|z|)] \tag{21}$$

The above equation is known as Hallen's (1938) integral equation for a wire shown in Figure 2-1. The constant is evaluated from the boundary condition which requires the current to vanish at the end of the wire. If V_i is the terminal voltage of the antenna, then it could be shown that $C_2 = V_i / 2$.

Although both Hallen's and Pocklington's equations may be used in treatment of wire antennas, the latter enjoys a

particular popularity. This is due to several factors such as i) exhibition of rapid convergence, ii) only well-behaved kernels (exact) need be calculated numerically, iii) it admits the use with equal ease any form of excitation, and iv) the simplicity is retained[9]. Furthermore, for a wire of N divisions, Hallen's equation requires the inversion of an N+1 matrix whereas Pocklington's equation requires the inversion of an N order matrix[1]. Also as mentioned before, Hallen's equation exclusively uses a delta gap voltage generator, but Pocklington's equation is more adaptable and allows a different variety of sources[10].

2.2 Point Matching

The next step is to numerically solve the chosen integral equation. Pocklington's equation will be used throughout this work for reasons described above. The integral equation will be solved numerically by writing N equations in N unknowns. This is exactly analogous to solving Kirchhoff's network equations for N nodes[3],

$$\sum_{n=1}^{N} Z_{mn} I_n = V_m \quad , \quad m=1,2,\ldots,N \tag{22}$$

if we rewrite eqn.(1), which is the general form of an integral equation, for a thin wire of length l, we get

$$\int_{-\frac{l}{2}}^{\frac{l}{2}} I(z')\,K(z,z')\,dz' = -E_z^p(z) \tag{23}$$

The unknown current I(z´) may be approximated by a finite series such that

$$I(z') = \sum_{n=1}^{N} I_n g_n(z') \tag{24}$$

where $g_n(z')$ are the basis or expansion functions[11,12], and I_n's are complex coefficients. Equation (23) changes to

$$\sum_{n=1}^{N} I_n \int_{-\frac{l}{2}}^{\frac{l}{2}} g_n(z')\,K(z,z')\,dz' \approx -E_z^p(z) \tag{25}$$

The approximate equality sign is due to the fact that we are approximating the current with a finite number of segments on the wire. There would be an equal sign as N approaches infinity. Figure 2-2 shows the segmentation of the wire. The integral equation is enforced at N points (a different Z_m at each point), and hence N independent equations with N unknowns are created[3]. This process is called point matching. As shown in Figure 2-2a, the matching points may be chosen to be along the axis of the wire with $I_z(z')$ flowing on the surface. Figure 2-2b however, is analogous to that of Fig. 2-2a, considering the reciprocity of the situation and hence the matching points could be selected on the surface and an equivalent

filamentary line-source current could be placed along the centre axis of the wire[1]. Considering eqn.(25), we let

$$g(z_m, z'_m) = \int_{-\frac{l}{2}}^{\frac{l}{2}} g_n(z')\, K(z, z')\, dz' \qquad (26)$$

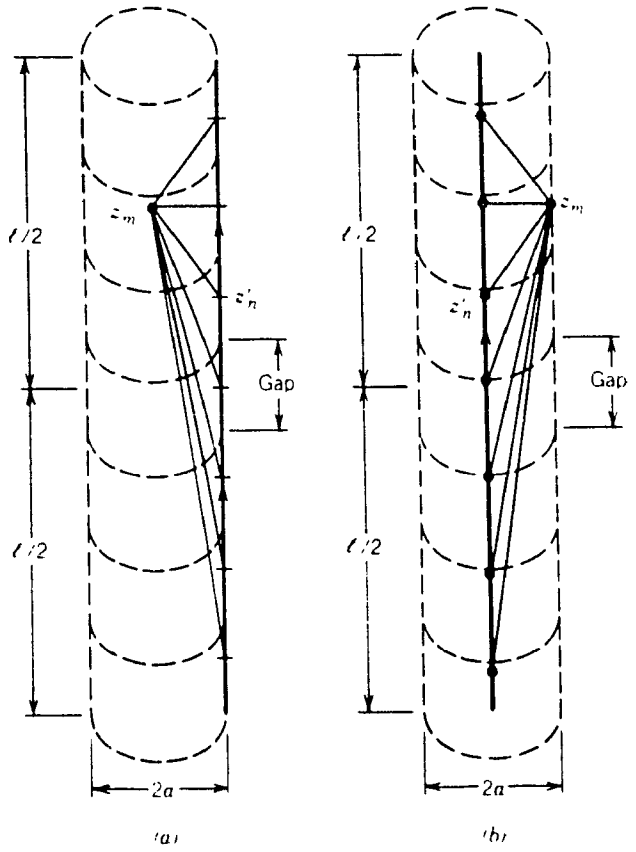

Figure 2-2 Dipole segmentation and its equivalent current (a) on the surface and (b) along its centre[1].

then using (26) in (25) yields

$$I_1\ g(z_m, z_1') + I_2\ g(z_m, z_2') + \ldots + I_N\ g(z_m, z_N') \approx -E_z^p(z_m) \tag{27}$$

which may be written as

$$\sum_{n=1}^{N} Z_{mn}\ I_n = V_m \tag{28}$$

where

$$Z_{mn} = g(z_m, z_n') \tag{29}$$

and

$$V_m = -E_z^p(Z_m) \tag{30}$$

Equation (28) is a network formulation of the electromagnetic problem obtained by point-matching method.

In the method of point-matching or collocation[1], the boundary conditions are enforced only at discrete points z_m (fig.2-2), and may not be satisfied at other points. Therefore, a deviation or a residual term is introduced such that

$$R = E_{tan}^{pri} + E_{tan}^{sec} \tag{31}$$

where R is the residual term. Employing eqn.(27) in (31) yields

$$R(z) = \sum_{n=1}^{N} I_n\ g(z, z_n') + E_z^p(z) \tag{32}$$

From eqn.(32) it is apparent that point-matching procedure is a special case of the above situation and evaluates the residual at the points z_m, m=1,2,...,N. In the residuals

(or weighted residuals[3]) method the I_n's are found such that the residual is forced to zero in an average sense[3]. So, for the boundary conditions to be satisfied, we require

$$\int_{-\frac{l}{2}}^{\frac{l}{2}} W_m(z) R(z)\, dz = 0 \quad , \quad m = 1, 2, \ldots, N \tag{33}$$

where $W_m(z)$ are weighting functions. Employing (32) in (33), we get

$$\int_{-\frac{l}{2}}^{\frac{l}{2}} W_m(z) \sum_{n=1}^{N} I_n g(z, z_n')\, dz + \int_{-\frac{l}{2}}^{\frac{l}{2}} W_m(z) E_z^p(z)\, dz = 0 \tag{34}$$

which then could be solved for the current. There are, however, inadequacies regarding collocation solutions to Pocklington-type integral equations. One of the important ones, which needs some consideration, is that match-points cannot be spaced sufficiently densely in the feed region of a wire antenna to accurately sample the highly local driving field when the feed diameter is very small[13].

It is obvious that the choice of basis and weighting functions is an important one, for they play an important role in determining the accuracy and efficiency of the results. Generally, it is desirable to choose basis functions that closely resemble the anticipated form of the current on the wire[3]. One goal of the basis-and weight-function selection is to minimize computer time while maximizing accuracy for the problem set. Another

might be to replace problem's physical behaviour with as few samples as possible[14].

2.2.1 Basis Functions

The kind of basis function used, ultimately determines how well the numerical results approximate the true behaviour of the unknown for a given order of matrix. Basis functions are chosen on the basis of how closely a candidate function resembles the physical behaviour of the unknown it represents[14]. There are two types of bases used in moment method modelling, namely subdomain and entire-domain functions.

Subdomain functions are more commonly used due to the fact that a prior knowledge of the nature of the function represented by them is not needed. It involves the use of bases which are applied in a repetitive fashion over subdomains or sections of the object being modelled[14]. The simplest example of a subdomain basis is the pulse or stairstep function. More common functions however, are piecewise linear and piecewise sinusoid basis functions. Piecewise linear functions[1] are defined by $g_n(x')$, where

$$g_n(x') = \frac{x'-x'_{n-1}}{x'_n-x'_{n-1}} \quad if \quad x_{n-1} \leq x' \leq x'_n \tag{35a}$$

$$g_n(x') = \frac{x'_{n+1} - x'}{x'_{n+1} - x'_n} \quad if \quad x'_n \le x' \le x'_{n+1} \tag{35b}$$

$$g_n(x') = 0 \qquad elsewhere \tag{35c}$$

Another function, which may improve accuracy over linear function and is useful for other reasons, such as advantages in computation time and resistance to error, is piecewise sinusoid[1], where in this case $g_n(x')$ is defined as

$$g_n(x') = \frac{\sin[\beta(x' - x'_{n-1})]}{\sin[\beta(x'_n - x'_{n-1})]} \quad if \quad x'_{n-1} \le x' \le x'_n \tag{36a}$$

$$g_n(x') = \frac{\sin[\beta(x'_{n+1} - x')]}{\sin[\beta(x'_{n+1} - x'_n)]} \quad if \quad x'_n \le x' \le x'_{n+1} \tag{36b}$$

$$g_n(x') = 0 \qquad elsewhere \tag{36c}$$

Both of these functions, in the forms of multiple and functional representations, are displayed in Figure 2-3.

The entire-domain basis functions, use multiterm expansions extending over the entire object and are nonzero. A common entire domain sinusoidal function would be[1]

$$g_n(x') = \cos\left[\frac{(2n-a)\pi x'}{l}\right] \quad where \quad \frac{-l}{2} \le x' \le \frac{l}{2} \tag{37}$$

As shown in eqn.(37), entire-domain functions are not segmented.

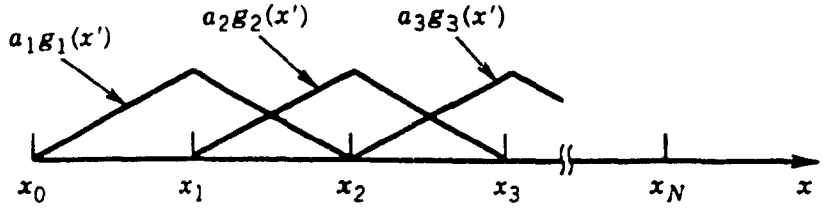

(a)

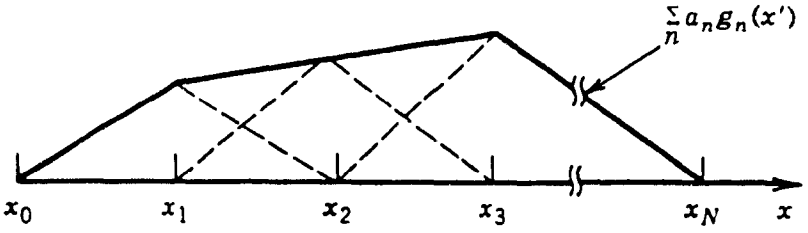

(b)

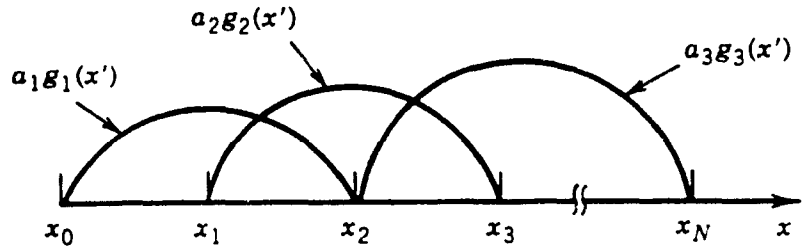

(c)

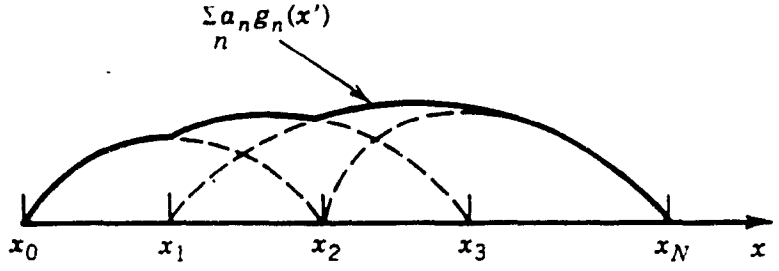

(d)

Figure 2-3 Piecewise linear and sinusoid subdomain function (a) Multiple linear (b) Linear function representation (c) Multiple sinusoid (d) Sinusoid function representation[1].

Although subdomain bases are probably more flexible in terms of their applicability, they have a disadvantage generally not exhibited by the entire-domain form, which is the discontinuity that occurs at the domain boundaries. This discontinuity arises because an n_s term subdomain function can provide at most $(n_s - 1)$th continuity to an adjacent basis of the unknown it represents assuming one of the n_s constants is reserved for the unknown itself[14].

2.2.2 Weighting Function

Weighting functions play an important role in the evaluation procedure, and are linearly independent. Dirac delta function is a common and simple weighting function and leads to a point sampled system of equations. Distributed multiterm weight functions can also be employed on both types of basis functions and would cause the resultant equations to be smoother. One example of this is the special case where the same functions are used for both the bases and weights, a procedure known as Galerkin's method[14]. The Moment method employs techniques involving weighting functions in its procedure[2,11].

2.3 Numerical Electromagnetics Code (NEC)

One of the most favoured computer codes to analyze the

interaction of electromagnetic waves with an arbitrary surface and wire structures is Numerical Electromagnetics Code (NEC). It combines an integral equation for smoothness with one for wires to provide for convenient and accurate modelling of a wide range of structures[15].

2.3.1 The Electric Field Integral Equation (EFIE)

Program NEC uses the electric field integral equation (EFIE) for thin wires and magnetic field integral equation (MFIE) for surfaces. An EFIE-MFIE hybrid equation is used for cases containing both surfaces and wires. Due to the fact that throughout this work we exclusively deal with thin wire structures, only EFIE need be mentioned. The EFIE is preferred for thin wires and structures where there is little separation between a front and back surface. The assumptions in the case of thin wire approximation are[15];

a. Transverse currents can be neglected relative to axial currents on the wire.

b. The circumferential variation in the axial current can be neglected.

c. The current can be represented by a filament on the wire axis.

d. The boundary condition on the electric field need be enforced in the axial direction only.

Once the above assumptions are taken into consideration, the final scalar equation derived is[15]

$$-\hat{Z}\cdot\bar{E}^{i}(\bar{r}) = \frac{-j\eta}{4\pi\kappa}\int_{L} I(z')\,(\kappa^{2}\ \hat{Z}\cdot\hat{Z}' - \frac{\partial^{2}}{\partial Z\ \partial Z'})\,G(\bar{r},\bar{r}')\,dZ' \qquad (38)$$

where

$\bar{r}$= *observation point vector*

$\bar{r}'$= *source point vector*

2.3.2 NEC Basis and Weighting Functions

As mentioned before, basis and weighting functions directly effect the efficiency and accuracy of the solution. When the basis and weighting functions are the same, the procedure is known as Galerkin's method[16]. In NEC however, the basis and weight functions are not the same. The weight function is a set of delta functions[15], denoted by $W_{i}(\bar{r})$ where

$$W_{i}(\bar{r}) = \delta\,(\bar{r}-\bar{r}_{i}) \qquad (39)$$

with $\bar{r}_{i}$ denoting a set of points on the conducting surface. This would result in wires being divided into short straight segments with each segment having a sample point at its centre. A point sampling of the integral equation takes place and is known as collocation method of solution[15].

The expansion function in NEC represents current on wire by three terms; a constant, a sine and a cosine - with the sinusoidal term having the free space wavelength[15]. The total current on a segment j is

$$I_j(s) = A_j + B_j \sin \kappa(z-z_j) + C_j \cos \kappa(z-z_j) \quad , \quad |z-z_j| < \frac{\Delta_j}{2} \qquad (40)$$

where Z is the distance parameter along the wire, Z_j is the value of Z at the center of the segment j and Δ_j is the length of segment j. Two of the three unknowns A_j, B_j and C_j are eliminated by local conditions on the current. The third, which relates to the current amplitude, is determined by the matrix equation[15]. This expansion function causes the solution to rapidly converge and the fields of sinusoidal currents are easily evaluated in closed form[15,17]. It provides continuous charge density, but produces a discontinuous first derivative in charge equivalent to a tripole charge at each junction[14].

2.3.3 Wires at Junctions and Free-ends

The program NEC is usually applied to wire grid structures which contain numerous wires. These wires either create junction points, where two or more wires are connected together, or cases in which some have free ends. For each situation corresponding boundary conditions should

be considered.

For an ideal thin wire, one may assume the current to vanish at the end of the wire. But for a wire with a finite radius the current at the end point may be nonzero[15]. For a wire of radius a, the restriction on the current at the end cap of the wire, shown in Figure 2-4, is[15]

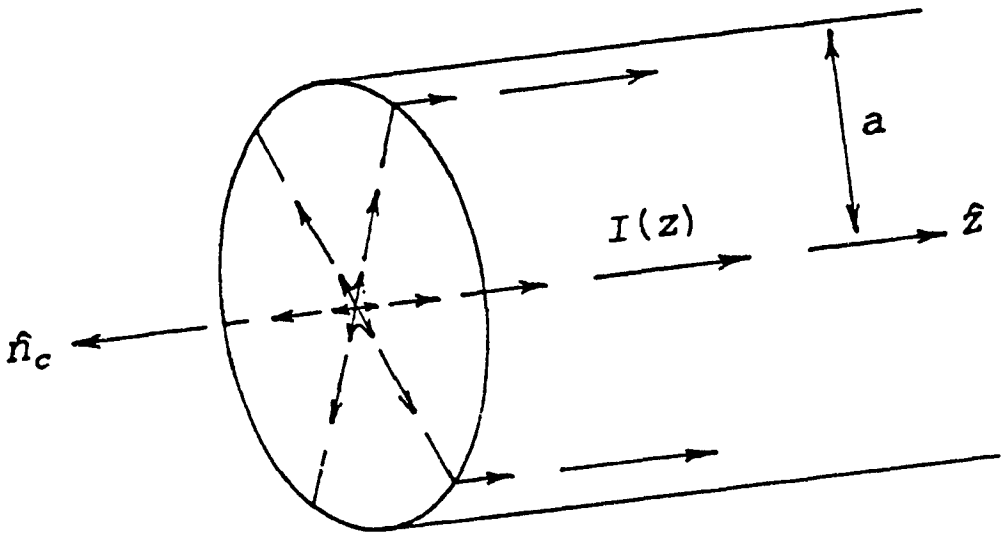

Figure 2-4 Current flow at the end cap of a segment with finite radius[18].

$$I(z)\big|_{z \text{ at end}} = \frac{-(\hat{z}\cdot\hat{n}_c)\,J_1(\kappa a)}{\kappa J_0(\kappa a)} \frac{\partial I(z)}{\partial z}\Big|_{z \text{ at end}} \qquad (41)$$

where

$$\kappa = 2\pi/\lambda.$$

J_0 and J_1 are Bessel functions of order 0 and 1

$\hat{n}_c$ and $\hat{z}$ are unit vectors shown in Fig. 2-4.

As seen in Figure 2-4, the dot product of $\hat{z}$ and $\hat{n}_c$ would be positive, if $\hat{z}$ is directed toward the end. And if Z is directed away from the end, it would yield a negative result.

Treatment of junction discontinuities in wire antennas usually involves the use of continuity equation in the vicinity of the junction to obtain the constraint on the current on the junction[19,23,24]. In this work, the method used in NEC theory to arrive at a complete current basis function is discussed. In order to determine the total axial current in a junction of n wires, n conditions must be imposed on the currents and their derivatives at the junction. These conditions are created by Kirchhoff's current law and (n-1) restraints on their derivatives[19]. The equation of continuity for wire i (Figure 2-5), which relates linear charge density and current is

$$\frac{\partial I_i}{\partial z} + i\omega q_i = 0 \qquad (42)$$

The restrictions on wires with different radii at a junction require that

$$\frac{\partial I(z)}{\partial z}\Big|_{z \text{ at junction}} = \frac{Q}{P} \qquad (43)$$

where Q is a constant for all wires at the junction and is

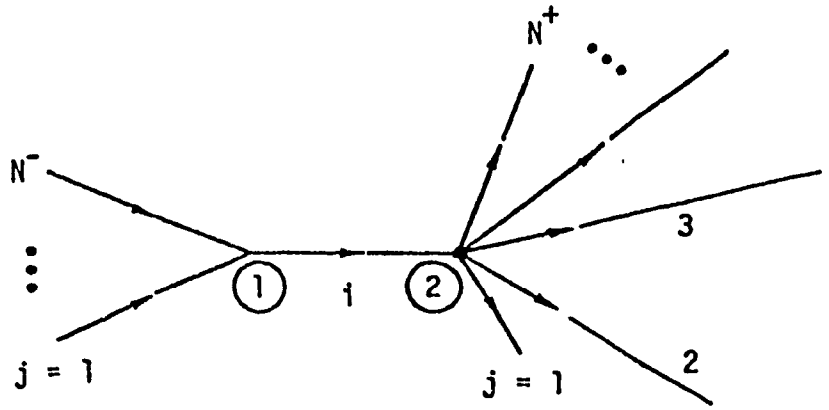

Figure 2-5 Segments covered by the i th basis function[15].

related to the total charge in the vicinity of the junction[15], and P is a proportionality factor that depends on the wire radius, a, and defined to be

$$P_i = \ln\left[\frac{2}{\kappa a_i}\right] - \gamma \qquad (44)$$

where

$$\kappa = 2\pi/\lambda \ ,$$

and $\gamma = 0.5722$ (Euler's constant).

This condition, which is also known as King-Wu condition[19], ensures that the current derivative is continuous across the junction, ie;

$$\left(\frac{\partial I_1(z)}{\partial z}\right) P_1 = \left(\frac{\partial I_2(z)}{\partial z}\right) P_2 = \ldots = \left(\frac{\partial I_n(z)}{\partial z}\right) P_n \qquad (45)$$

Considering segment i in Figure 2-5, it is considered that the current basis function has a peak on segment i and residual effect on every other segment connecting to i and vanishing at the outer ends of connected segments[15]. The portion of basis function on segment i is

$$f_i^{\circ}(z) = A_i^{\circ} + B_i^{\circ} \sin \kappa(z - z_i) + C_i^{\circ} \cos \kappa(z - z_i) \tag{46}$$

where $|z - z_i| < \Delta_i/2$ and Δ_i is the length of segment i.

In Figure 2-5 either N^- or N^+ may be equal to zero, which implies that in either case segment i may have one free end. Thus, the equations obtained are

$$f_i^{\circ}\left(z_i \pm \frac{\Delta_i}{2}\right) = \mp \frac{1}{\kappa} \frac{J_1(\kappa a_i)}{J_0(\kappa a_i)} \frac{\partial f_i^{\circ}(z)}{\partial z}\Big|_{z = z_i \pm \frac{\Delta_i}{2}} \quad (free\text{-}end) \tag{47}$$

and

$$\frac{\partial}{\partial z} f_i^{\circ}(z)\Big|_{z = z_i \pm \frac{\Delta_i}{2}} = \frac{Q_i^{\pm}}{P_i} \quad (at\ junction) \tag{48}$$

where Q_i are associated with the junction and may be eliminated using Kirchhoff's equation[15]. For end 1 of segment i , the basis function is

$$f_j^{-}(z) = A_j^{-} + B_j^{-} \sin \kappa(z - z_j) + C_j^{-} \cos \kappa(z - z_j) \tag{49}$$

where
$|z - z_j| < \frac{\Delta_j}{2}$, $j = 1, \ldots, N^-$

and subjected to the conditions

$$f_j^-(z_j-\frac{\Delta_j}{2})=0 \tag{50a}$$

$$\frac{\partial}{\partial z}f_j^-(z)\,|_{z=z_j-\frac{\Delta_j}{2}}=0 \tag{50b}$$

and

$$\frac{\partial}{\partial z}f_j^-(z)\,|_{z=z_j+\frac{\Delta_j}{2}}=\frac{Q_i^-}{P_j} \tag{50c}$$

for end 2 of segment i, the basis function is

$$f_j^+(z)=A_j^++B_j^+\sin\,\kappa(z-z_j)+C_j^+\cos\,\kappa(z-z_j) \tag{51}$$

where

$$|z-z_j|<\frac{\Delta_j}{2}\quad,\ j=1,\ldots,N'$$

with the following end conditions

$$\frac{\partial}{\partial z}f_j^+(z)\,|_{z=z_j-\frac{\Delta_j}{2}}=\frac{Q_i^-}{P_j} \tag{52a}$$

$$f_j^+(z_j+\frac{\Delta_j}{2})=0 \tag{52b}$$

and

$$\frac{\partial}{\partial z}f_j^+(z)\,|_{z=z_j+\frac{\Delta_j}{2}}=0 \tag{52c}$$

The complete current basis function has a total of

[3($N^+ + N^- + 1$)] unknown constants[15], and is defined by equations (46), (49) and (51). Of these constants, all but one are eliminated in terms of Q_i^- and Q_i^+ by use of end conditions. The charges are then determined by applying Kirchhoff's current equations,

$$\sum_{j=1}^{N^-} f_j^-\left(z_j+\frac{\Delta_j}{2}\right)=f_i^\circ\left(z_i-\frac{\Delta_i}{2}\right) \tag{53a}$$

$$\sum_{j=1}^{N^+} f_j^+\left(z_j-\frac{\Delta_j}{2}\right)=f_i^\circ\left(z_i+\frac{\Delta_i}{2}\right) \tag{53b}$$

The only one remaining constant, which is related to current expansion coefficient, would be solved by moment method.

2.3.4 The Kernel of EFIE

The Numerical Electromagnetic Code uses a series expansion to approximate the full kernel equation for the cases of thin-wire and extended thin-wire kernel. Extended kernel is used when the wire is thick enough to invalidate the filamentary thin-wire approximation. The thin-wire kernel approximates the source current by a filament on the segment axis with the observation point on the surface of the segment[15]. The full kernel equation, as used in magnetic vector potential is given as

$$G=\frac{1}{2\pi}\int_{\phi'=0}^{2\pi}\frac{\exp[-j\kappa(\rho^2+a^2-2a\rho\cos\phi'+(z-z')^2)^{\frac{1}{2}}]}{[\rho^2+a^2-2a\rho\cos\phi'+(z-z')^2]^{\frac{1}{2}}}d\phi' \qquad (54)$$

The above integral can not be evaluated in closed form, but could be approximated by a series expansion in powers of a^2, as explained in Appendix of reference [15]. The first term in the series expansion, which is a Maclaurin series about a=0 [20], is known as the reduced thin-wire kernel. Extended thin-wire kernel uses terms of order a^2, and terms of order a^4 are neglected. The NEC program provides the user with both choices and uses them as follows; if the observer is placed on the axis of the wire carrying current, or on the axis of a collinear wire, the extended kernel approximation is employed. But, when the observer is placed on the surface of the wire, other than the one carrying the current, the thin-wire kernel option is used[21].

2.3.5 The Effect Of A Ground Plane

The problem of a radiating structure operating near the interface between two semi-infinite media with different electrical properties has been considered for a very long time. A special case would be the operation of an antenna above a perfect ground, as illustrated in Figure

2-6. Sommerfeld provided a rigorous solution to treat

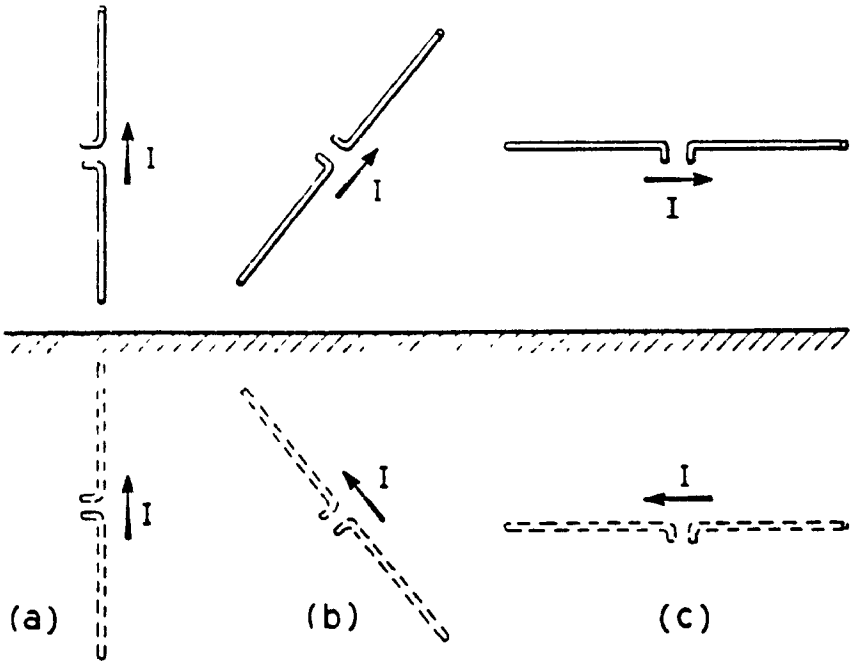

Figure 2-6 Antennas and their images [7].

arbitrarily oriented antennas of various geometries by properly combining his integrals for vertically and horizontally oriented infinitesimal electric and magnetic sources[70]. The rigorous solution provided by Sommerfeld however, is very cumbersome and time consuming even when high speed computers are used. In order to achieve a reasonable balance, a popular option in NEC uses an approximation based on the Fresnel plane-wave reflection coefficients[71,72]. This is the option used to obtain the computed results throughout this work. As mentioned by

Miller[72], "the approximate method to account for the ground-reflected fields using the Fresnel plane-wave reflection coefficients has been found to produce results generally within 10% of those obtained using the rigorous Sommerfeld integrals, but at approximately 1% of the computer cost. It is therefore concluded that the reflection coefficient approach provides a viable and economical alternative to the Sommerfeld theory for the analysis of arbitrary oriented wire antennas over lossy half-spaces". Although this approximation is a viable and economical alterative, the NEC user must remember that it is also inaccurate for structures very near to the ground[15].

CHAPTER 3

COMPUTER MODEL DEVELOPMENT AND VALIDATION

The advancement of computers in the past several years and availability of codes, such as NEC, have made computer models an almost ideal replacement for costly measurements. For instance, wire grid models of aircraft, which are used as input to the NEC code, are a popular example. Wire grid models are used to represent solid conducting surfaces of aircraft and replace them with a grid of wires. When constructing a wire grid model, one has to ensure that, from a geometrical and electrical point of view, the model follows the original surface as closely as possible. This will allow a current distribution similar to that of the aircraft. In order to derive an accurate model, one has to abide by rules known as "Modelling Guidelines".

3.1 Model Generation and Guidelines

Modelling guidelines are either the direct result of assumptions made in deriving electric field integral equation (EFIE) and solving it with moment method[15,25], or due to the dimensional limitations in the NEC code on

lengths and radii of segments. The ratios of length to radius of a single segment, length to length and radius to radius of adjoining segments also contribute to these guidelines. Even though a small deviation is allowed in certain cases, a general failure to observe these guidelines may result in computation of field and current flow that are not supported by actual measurements, for the program NEC does not check for violations in modelling guidelines.

As mentioned before, two main factors which must be considered in constructing a wire grid model are geometrical and electrical. In case of the former, one designs the segments to follow the paths of conductors as closely as possible by using a piece-wise linear fit on curves. This is a relatively simple task of geometrical consideration and the designer has no other option but to follow the shape of the aircraft. It is not possible to establish a *priori* what number of segments will yield acceptably accurate results for a given structure, but it is desirable to use as few segments as possible without altering the electromagnetic characteristic of the model. This is to reduce the computation time in NEC, which varies as N^3 for a model of N segments[15]. In areas where more current is suspected to flow, such as feed points, denser segmentation is required at the junctions. As a wire

segment is defined by the coordinates of its two end points and its radius[15], adjacent segments must have coincident end points to satisfy boundary conditions at these points. Experience gained in the analysis of various structures, such as aircraft, indicates that maximum solution efficiency and accuracy is obtained using nearly equal length for all segments[22].

The length of the segment, Δ, its radius, a, and their respective ratios to wavelength, λ, are the main electrical considerations. The length of a segment is generally required by NEC to be less than $\lambda/10$ at the desired frequency. This is due to the fact that when computing far field results, using collocation method with sinusoidal current interpolation, the numerical accuracy for a typical thin-wire structure can be expected to be in the range 10^{-1} - 10^{-2} using 6 to 18 segments per wavelength, depending upon structure complexity[14,22]. Segments shorter than $\lambda/1000$ are considered invalid and lead to numerical inaccuracy[15].

Guidelines resulted from approximations used in the kernel of EFIE that place certain limitations on the wire radius, relative to wavelength, λ, and segment length, Δ. These approximations give rise to the thin-wire kernel option in the NEC code. As mentioned before, the thin-wire kernel reduces the current on the surface of a segment to

a filament on its axis, where as the extended thin-wire approximates the current using a series expansion of the exact field in terms of a^2. In both cases the circumferential component is ignored and only the axial component of the current is considered. The NEC code requires that $2\pi a/\lambda$ be much less than one, and restrictions be placed on Δ/a ratio, so that the accuracy of numerical solution is improved[15,43]. These restrictions limit the value of Δ/a to be greater than 8 for thin-wire option and as small as 2 for extended thin-wire option to warrant a field solution with errors of less 1%. A current solution yielding errors smaller than a field solution requires Δ/a to be greater than 2 for thin-wire option and as small as 0.5 for extended thin-wire kernel option, which would be activated by inclusion of an EK card in the data deck[15]. A circuit approach to wire grid modelling requires similar limits on the value of Δ/a. In this approach the wire radius is chosen such that the difference between the impedance of a closed surface and its corresponding wire grid model is minimized. This difference, ΔL, eqn.55,

$$\Delta L = L_{\text{wire grid}} - L_{\text{closed surface}}$$

$$\approx \frac{\mu\Delta}{2\pi} \ln\left(\frac{\Delta}{2\pi a}\right) \qquad (55)$$

is obtained using the impedance equation of a transmission

line, with infinity as ground[26]. In the above equation ΔL is minimized when $\Delta/a > 0.608$, which is in agreement with the NEC restrictions.

The relationship between Δ and a may also be determined by another method known as the "adapted equal-area rule", derived by Trueman[21], which relates the areas of the meshes with the length and radius of their wire components.

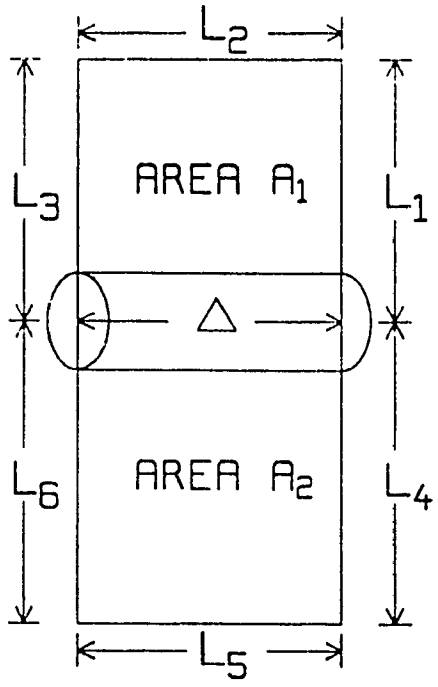

Figure 3-1 A wire of length Δ is part of a grid, and subtends meshes of areas A_1 and A_2 [21].

The adapted equal-area rule, illustrated in Figure 3-1, states that;

$$a=\left[\frac{A_1}{\pi L_{t1}}+\frac{A_2}{\pi L_{t2}}\right] \qquad (56)$$

where;

A_1 = area of mesh #1.

A_2 = area of mesh #2.

$L_{t1} = L_1 + L_2 + L_3 + \Delta$ = length of periphery of mesh #1.

$L_{t2} = L_4 + L_5 + L_6 + \Delta$ = length of periphery of mesh #2.

At junctions, where two or more wires are joined, the guidelines place restrictions on the radius and segment length ratios of connecting wires. The radius ratios must lead to an equitable distribution of accumulated charges at junctions amongst participating wires[15,19]. This is to accurately model the local behaviour of physical currents and to increase the accuracy. It is recommended that the radius ratio not exceed 5, and severe errors would result if the ratio is greater than 10[21]. One way of avoiding this problem is to change the radius in steps over several segments. The segment ratio on the other hand may not exceed 5, so that a maximum solution accuracy and efficiency is reached. The segment to radius ratio, Δ/a, depends on the selection of kernel option. At junctions however, the normal thin-wire kernel is always used and hence, segments with small Δ/a should be avoided[15]. Another problem encountered at wire junctions is the

shallow angle of intersection between wires. This causes the match point of one wire to be placed in the volume of another. Since NEC does not restrict the value of this angle, overlapping leads to physically meaningless results[15].

Generic modelling guidelines and issues regarding individual wires, which must be kept in mind when developing a numerical model for NEC, are listed in table 1. At junctions, where two or more wires are involved, radius to radius and segment to segment ratios must be considered. The guidelines regarding these ratios are listed in Table 2.

3.1.1 Programs Utilized In Model Generation

The three dimensional numerical wire-grid model is derived using various software modules. These modules determine coordinates of the two end vertices for each wire and aid in conforming to the modelling guidelines. The end product is a valid input file (NECIN) for the program NEC.

3.1.1.1 DIDEC

The DIDEC module is the first program used in deriving the wire-grid model of an structure, such as aircraft. DIDEC (DIgitize, Display, Edit and Convert)[29,30] uses

orthogonal views of the structure for marking and

TABLE 1. SUMMARY OF GUIDELINES FOR INDIVIDUAL WIRES

MODELLING PARAMETER	EXPECTED RANGE	JUSTIFICATION
Wire radius, a	Adapted equal area rule	To obtain the best accuracy[21,27].
As related to wavelength, λ	$2\pi a/\lambda < 1$	Due to axial flow of current[14,15].
Wire segment length, Δ as related to radius a	$\Delta/a \rangle 2$ (Thin-wire Kernel) $\Delta/a \rangle 0.5$ (Extended Thin-wire Kernel)	To avoid oscillation in the current value near voltage sources, lumped loads or free wire ends[15].
As related to wavelength, λ	$\Delta \rangle \lambda/2\pi$	To sample current densely enough per unit wavelength[14,28].
Angle of intersection of wires, α	Larger than any angle which causes overlapping	Avoid placing the observation point of one wire segment within the volume of another wire[15].
Axial separation of wires, r_a	Several radii apart	Division of current between two overlapping segments is indeterminent[15,21].
Maximum no. of wires at a junction, N_j	$N_j \langle 30$	Due to dimension limitation in NEC[15].
Source location	Not on an open-ended segment	To avoid non physical situation of driving wire at open end[1,14,27].

digitization. Figure 3-2 illustrates orthogonal views of BELL CH-135 helicopter. Using a digitization tablet and orthogonal drawings, the wire-grid model of CH-135 was

digitized in two parts. The port side of the front fuselage section was first digitized. Taking advantage of the symmetry of the model, the starboard side was then created using DIDEC commands[31]. The tail section was similarly digitized and stored in a separate file.

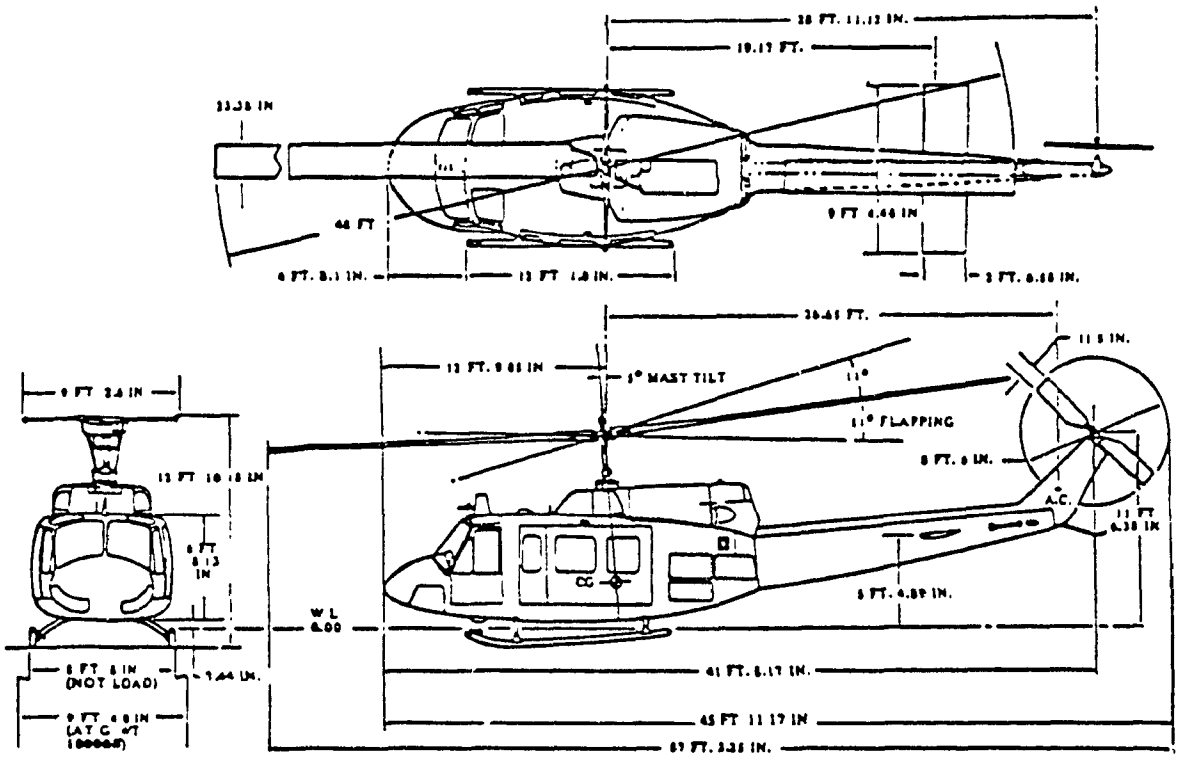

Figure 3-2 Orthogonal views of BELL CH-135 helicopter.

The two files were then merged to obtain the complete digitized model shown in Figure 3-3. Each wire in the grid model was assigned a radius value from a specified diameter table and hence the model was fully constructed. The model did not contain an antenna element, so that any desired

antenna may easily be installed. DIDEC is a powerful and user-friendly program which allows construction and display of three dimensional models using simple commands such as, REFLECT, MERGE, JOIN, CHAIN, and CUT[29].

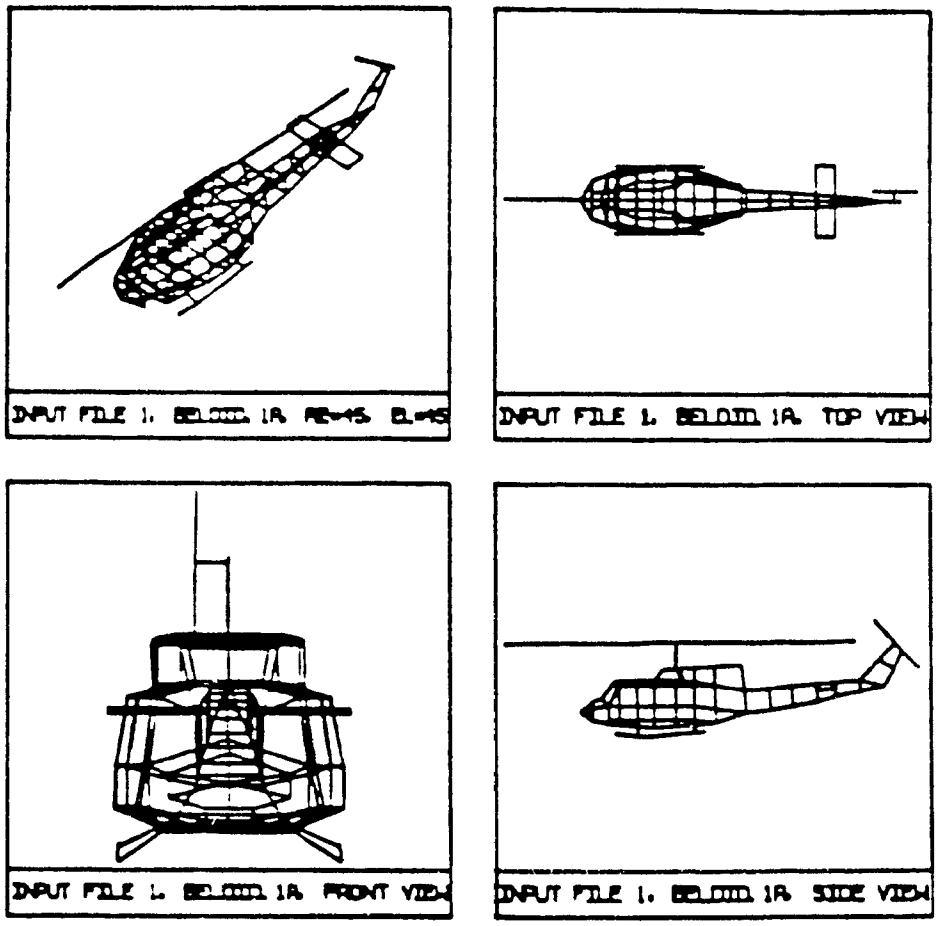

Figure 3-3 Orthogonal views of wire-grid model[31].

3.1.1.2 MESHES

Once the input file to NEC or (NECIN) file is

generated by DIDEC, it has to be revised to ensure modelling guidelines are implemented and model integrity is achieved. The first attempt is to find wire radii using equal area rule. But to do that one has to first identify the area of each individual mesh and its wire elements. Module MESHES[21] scans a NECIN file for meshes and produces an output file containing the vertices and elements involved in each mesh. This output file is then used as input to another module (FNDRAD) to find the radius of each wire. Other files are produced to indicate shortcomings such as, wires which are not members of any meshes in wire-grids. These files contain valuable information which may be utilized to modify the model in accordance with modelling guidelines.

3.1.1.3 RADIUS and FNDRAD

Once the area and size of a mesh is determined, The radii of wires involved may be found. Program RADIUS, written by Lan Nguyen, uses the "same surface area" rule of thumb to find the radius. The "same surface area rule" sets the total surface area of the wires to twice the area of the solid surface of a square grid[27,32]. The computed wire radii are then written to a NECIN file. Module FNDRAD[21], which is a continuation of MESHES in finding

wire radii, is a new module introduced at the EMC Laboratory of Concordia University. It uses the adaptive equal area rule, equation (56), to find wire radii. The radius values in most cases are close to those calculated by RADIUS. There are however several differences between RADIUS and FNDRAD. The most important difference is the limitation of RADIUS which checks for meshes of up to five wires at most, whereas MESHES and FNDRAD are capable of finding meshes of up to eight wires[21]. MESHES produces output files to display shortcomings in wire-grid and FNDRAD generates graphics files used to display mesh parameters such as mesh area, periphery and resonant frequency distributions.

Figure 3-4 illustrates four graphic files generated by FNDRAD for BELL CH-135. Part (a) shows that the CH-135 grid meshes have peripheries from about 0.65 to 1.55 of the mean, with two large meshes of approximate peripheries of about 2.1 of the mean. These meshes were located on the fuselage of the helicopter and due to geometrical construction further reduction of mesh periphery would have caused major errors. It was later proved that this particular case did not cause any inaccuracy in the model. Inaccuracies caused by meshes of large periphery are due to the fact that these meshes may accommodate frequencies at which large resonant currents are produced. The lowest

resonant frequency is where the mesh periphery equals one free space wavelength[21]. In part (b) of Figure 3-4, where resonant frequency of each mesh with respect to mean resonant frequency is computed and displayed, it is noted that the worst case cell has a resonant frequency of about 0.4 times the mean, or about 45.2 MHz. This is the upper limit for testing frequency and the wire grid model should not be tested at or above this frequency. Since the NEC runs are in the HF band with an upper frequency limit of 30 MHz, which is much less than 45.2 MHz, it is concluded that no inaccuracies are caused by these large meshes. Part (c) of Figure 3-4 shows that mesh area distribution for the BELL CH-135 wire grid. The wide distribution of mesh areas is due to several factors and limitations, the most important of which is the geometrical configuration of the helicopter. Feed and join regions of the HF antenna on BELL CH-135, which must be finely modelled, are at such locations many small cells must be used. These small cells appear as peak at a cell area of about one-half of the mean. Since the BELL wire-grid model has successfully passed the CHECK examination (described in the next section) with no errors, the wide distribution of its mesh area does not pose a significant problem. At this point one must remember that wire-grid modelling guidelines are meant to be a basis for compromise and not unbroken rules.

Sometimes satisfaction of one guideline may mean violation of another one, and hence it is up to the designer to make the right choice. In part (d) of

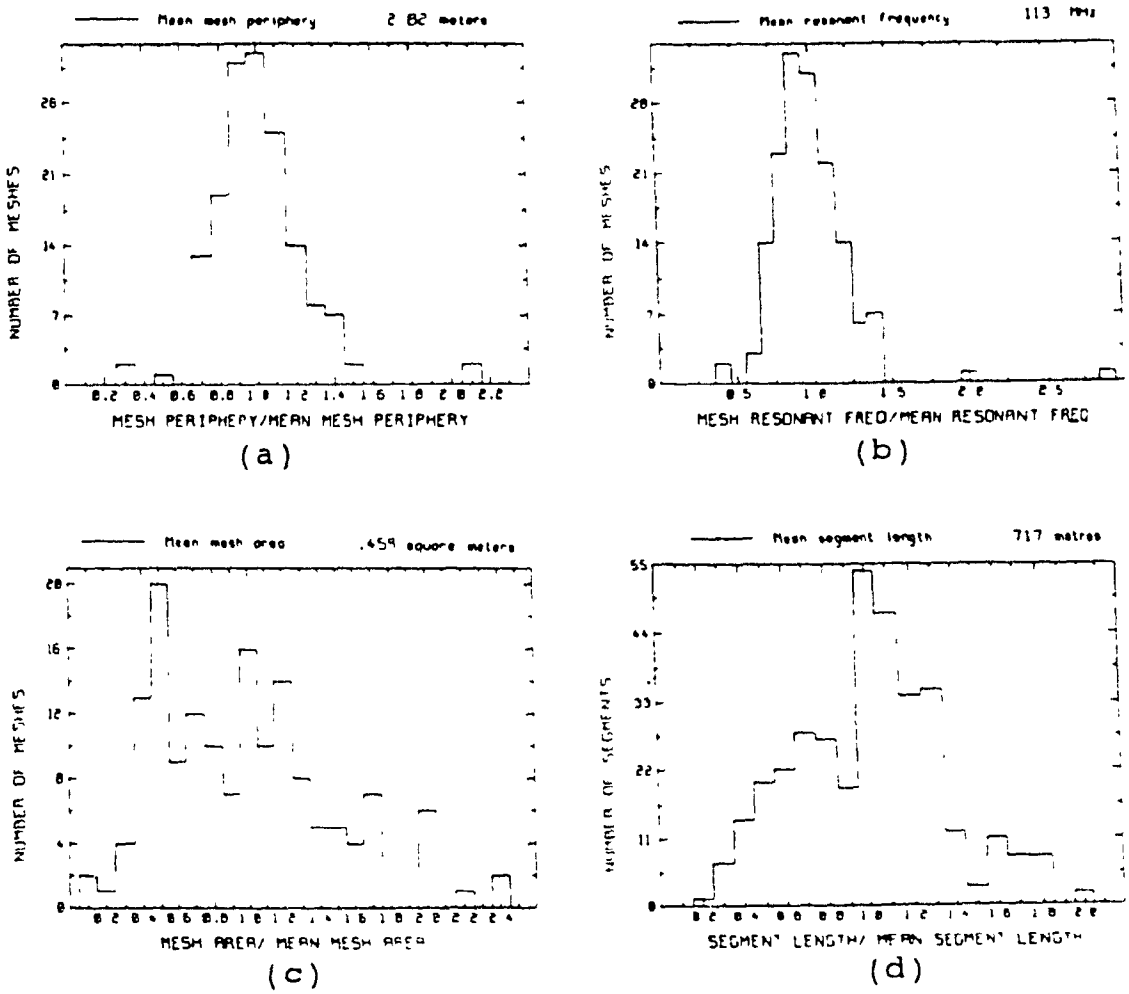

Figure 3-4 Wire-grid model parameters regarding (a) mesh periphery (b) mesh resonant frequency (c) mesh area (d) segment length.

Figure 3-4, a bar-graph distribution of segment lengths is shown. An ideal situation would be to have all segments to

be of the same length, which means a high concentration of segments with a single peak at the mean. In practice however, such concentration is rarely observed. As demonstrated by the nearly bell-shaped graph of part (d), most segments in the grid model are at or very close to the mean value.

3.1.1.4 CHECK and CLEAN

The module CHECK serves as the last step to verify the integrity of the wire-grid model. Developed and revised at the EMC laboratory, CHECK scans the model to assure that both individual and junction compatibilities with the guidelines are satisfied[18,21]. Discrepancies are detected in several degrees; Notes, Warnings and Errors. In a table formed by CHECK, a note (denoted by N) is issued if the wire parameter is approaching the boundaries of violating guidelines. A warning (denoted by W) is issued if the parameter does not have an ideal value and violates the lower limit. A serious breach of guidelines results in an error (denoted by E). The tag number of wire or wires involved along with the degree of discrepancy is stored in an output file. Table 2 lists the parameters and corresponding limits. The user must make sure all the wires for which an error is issued are reset to their

allowed values. A NECIN file must be absolutely free of errors., or else physically meaningless results are computed by NEC.

Correcting discrepancies detected by CHECK in the

TABLE 2. SUMMARY OF GUIDELINES AT JUNCTION

PARAMETER	TYPE OF DISCREPANCY	LIMIT
	JUNCTION DISCREPANCY	
Coincidence error	Error	Two coincident wires.
RAD/RAD	Warning Error	Longer/Shorter radius ⟩ 5.0 Longer/shorter radius ⟩ 10.0
Match point error	Error	Volume of one segment contains the centre of another.
SEG/SEG	Error	Longer /shorter segment ⟩ 5.0
SEG/RAD	Warning Error	2.0 ⟨ SEG/RAD ⟨ 8.0 2.0 ⟩ SEG/RAD.
	INDIVIDUAL DISCREPANCIES	
wire length	Error	Length ⟨ 0.01 M.
SEG/RAD	Warning	2.0⟨SEG/RAD⟨8 0.5 ⟨ SEG/RAD ⟨ 2 EK option
	Error	SEG/RAD ⟨ 2 SEG/RAD ⟨ 0.5 EK option
SEG/λ	Note Warning Error	0.05 ⟨ SEG/WAV ⟨ 0.1 0.1 ⟨ SEG/WAV ⟨ 0.2 SEG/WAV ⟩ 0.2 OR ⟨ 0.001
λ/RAD	Error	WAV/RAD ⟨ 30

NECIN file may be done manually. This however, may prove cumbersome. Module CLEAN, written by V. Tarantino, is

designed to remove detected incompatibilities at all three levels. Once the NECIN file is corrected, either manually or using CLEAN, an error free NEC input file is created and ready to be used by NEC.

3.2 Antenna Measurement

Measurement of the radiation patterns of antennas has long been a standard practice to determine antenna performance. A full-scale measurement performed under ideal conditions usually yields the best results. In the case of aircraft however, the immense amount of time, equipment and personnel required to perform even the simplest test makes it important to be able to use other methods of measuring radiation patterns. Scale model measurement is a proven and acceptable practice to study the properties of antennas[33].

The possibility of constructing a scale model of a given electromagnetic system is a direct consequence of linear properties of Maxwell's differential equations. Hence the model is only valid for linear media and nonlinear media such as ferromagnetic or ionized media must be excluded. Both homogeneous and nonhomogeneous medias may be used, for Maxwell equations are valid in both cases[34]. When constructing a scale model all dimensions

of the full-scale or prototype system must be divided by a constant scaling factor ρ. Theoretically ρ may be any arbitrary number, but it must also be practical. A reasonable choice of scale factor must yield reasonable diameter for antenna wire, so that it is easy to construct and does not go beyond the realm of reality. A typical full-scale HF antenna wire of about 0.125 inch diameter, and a scale factor of 1:100, would yield a scale model diameter of only 0.00125 inch. Such wire is not easily obtained and is, moreover, very fragile, making construction and handling of true scale model very difficult[35]. Hence the choice of the scale factor, ρ, must be a practical and logical one. Once a scale factor is chosen, all model parameters must be properly scaled. The conditions to be satisfied for a model in air are summarized in Table 3. As shown in Table 3, the values of dielectric constant and permeability are the same in both cases. Therefore the material used in the scale model must have the same property as in the real aircraft. For this purpose plywood may be used to replace insulating materials. The conductivity of the scale model however, is ρ times that of the full-scale value. Therefore modelling conductors using a large scale factor is a difficult task. A good conductor, such as copper, is used to replace metallic structures[36].

TABLE 3. CONSIDERATIONS FOR A GEOMETRICAL MODEL[34].

NAME OF QUANTITY	FULL-SCALE SYSTEM	MODEL SYSTEM
Length	l	$l' = l/\rho$
Conductivity	σ	$\sigma' = \rho\sigma$
Dielectric Constant	ε	$\varepsilon' = \varepsilon$
Permeability	μ	$\mu' = \mu$
Frequency	f	$f' = \rho f$
Wavelength	λ	$\lambda' = \lambda/\rho$
Phase Velocity	v	$v' = v$
Propagation Constant	κ	$\kappa' = \rho\kappa$
Resistance	R	$R' = R$
Reactance	X	$X' = X$
Impedance	Z	$Z' = Z$
Antenna Gain	g	$g' = g$

ρ = ratio of any full-scale length to the corresponding model length

3.2.1 Transmitting and Receiving Systems

Once the value of scale factor is decided, a scale model is constructed for the purpose of measurement. In the case of BELL CH-135, a scale factor of 24 was chosen and the model was constructed using a solid metallic block. The entire aircraft was then copper plated to provide an ideal condition for current distribution. Due to the fact that minimum amount of composite material was used in the construction of outer surface, it was decided that the

electromagnetic characteristic of the helicopter is negligibly altered if a conductor is used throughout the scale model construction. The model, shown in Figure 3-5, could be equipped with either a TRANLINE (shorted loop) or a ZIG-ZAG (open-ended zig-zag shaped) antennas. Separate measurements of the radiation patterns of both antennas

Figure 3-5 Scale model (1:24) of BELL CH-135 mounted on NRC range with arrow showing the connecting rod.

mounted on BELL CH-135 were carried out at the National Research Council (NRC) in Ottawa. Before discussing the measurement procedure, it is important to discuss the coordinate system used in the measurement.

In pattern measurements both the magnitude as well as

the polarization of the radiated signal must be known. The reference coordinate system, used both in the EMC laboratory and measurements, is shown in Figure 3-6.

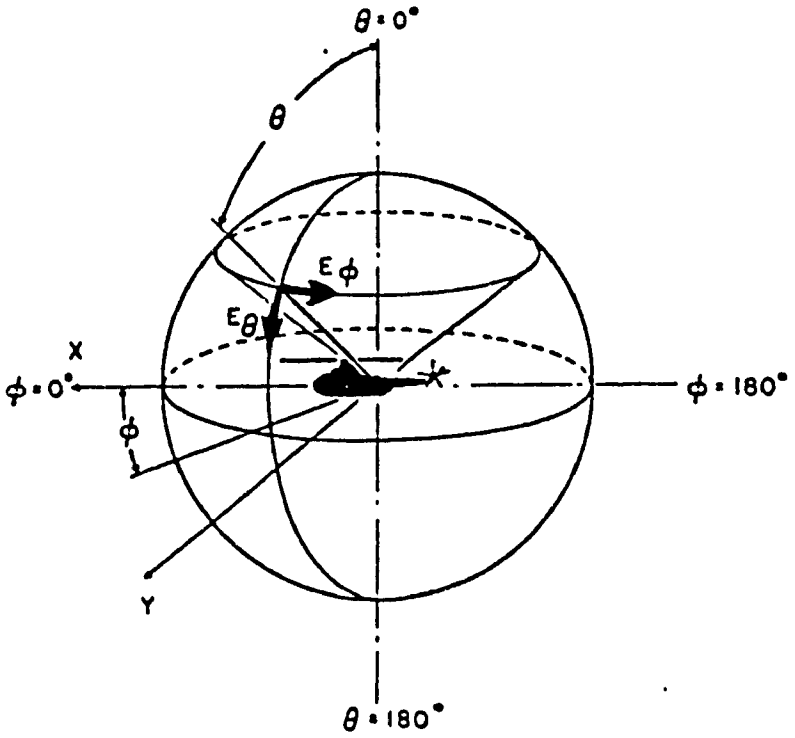

Figure 3-6 Reference coordinate system[37].

Due to the fact that a helicopter during the course of its flight may assume arbitrary positions with respect to the earth, the spherical coordinate system is fixed to the helicopter rather than to the earth. In the far field region, which is the region of interest for all aircraft, the relative angular distribution of the field becomes essentially independent of distance and the field at any

point in space may be resolved into two components E_ϕ and E_θ, as shown in Figure 3-6. The amplitude of the field, in the limit, is then given by the reciprocal of the first power of distance. The reason for this behaviour is that the relative phase and amplitude relationship between the field contributions from different elements of the antenna approach a fixed relationship[38].

In measuring antenna properties, the reciprocity principle is of fundamental importance[39]. It allows the determination of these properties in either transmitting or receiving conditions. For example, radiation pattern measurements of antennas could be made during either reception or transmission mode, whichever proves to be more convenient. The reciprocity theorem does not imply that antenna current distributions are the same for transmitting as for receiving[38].

The radiation patterns of CH-135, as a transmitting system, were measured using the NRC range, which is best suited for scale model measurements of aircraft[40]. The helicopter model was mounted on the tower spindle by means of a joining rod (shown by arrow in Figure 3-5).

The rod used for measurement of CH-135 TRANLINE antenna was a metallic conductor, and was later discovered to effect the radiation pattern at certain frequencies. This was an undesirable effect and was eliminated, when

measuring patterns of ZIG-ZAG antenna, by using a rod of composite material. The effects of the rod are discussed in future chapters. A block diagram of the NRC range is shown in Figure 3-7. The transmitting component of CH-135 model composed of a battery-operated frequency oscillator which was placed in a compartment constructed in the model and used to drive the antenna for signal generation. A set of oscillators was used to generate the desired frequency range, from 48 MHz to 720 MHz (unscaled frequency range is 2 MHz to 30 MHz) at frequency steps of 48 MHz (unscaled step size of 2 MHz). Due to battery drainage (a 9 volt battery was used), a frequency variation of about 0.6 MHz was observed in a two hour period. As a result, fine tuning adjustment had to be done if the measurement at a certain frequency lasted more than two hours.

The receiving component of the measurement system is composed of a dipole antenna mounted in a corner reflector as shown in Figure 3-8. The distance between the transmitter and receiver is adjusted on the basis that the field produced by the dipole antenna, if transmitting, would be essentially a plane wave in the region occupied by the model[36]. Otherwise, the distance is chosen to arrange for a maximum direct signal detection and uniform illumination. The receiving dipole may be removed and the user is provided with the option of installing a suitable

dipole for a particular frequency range.

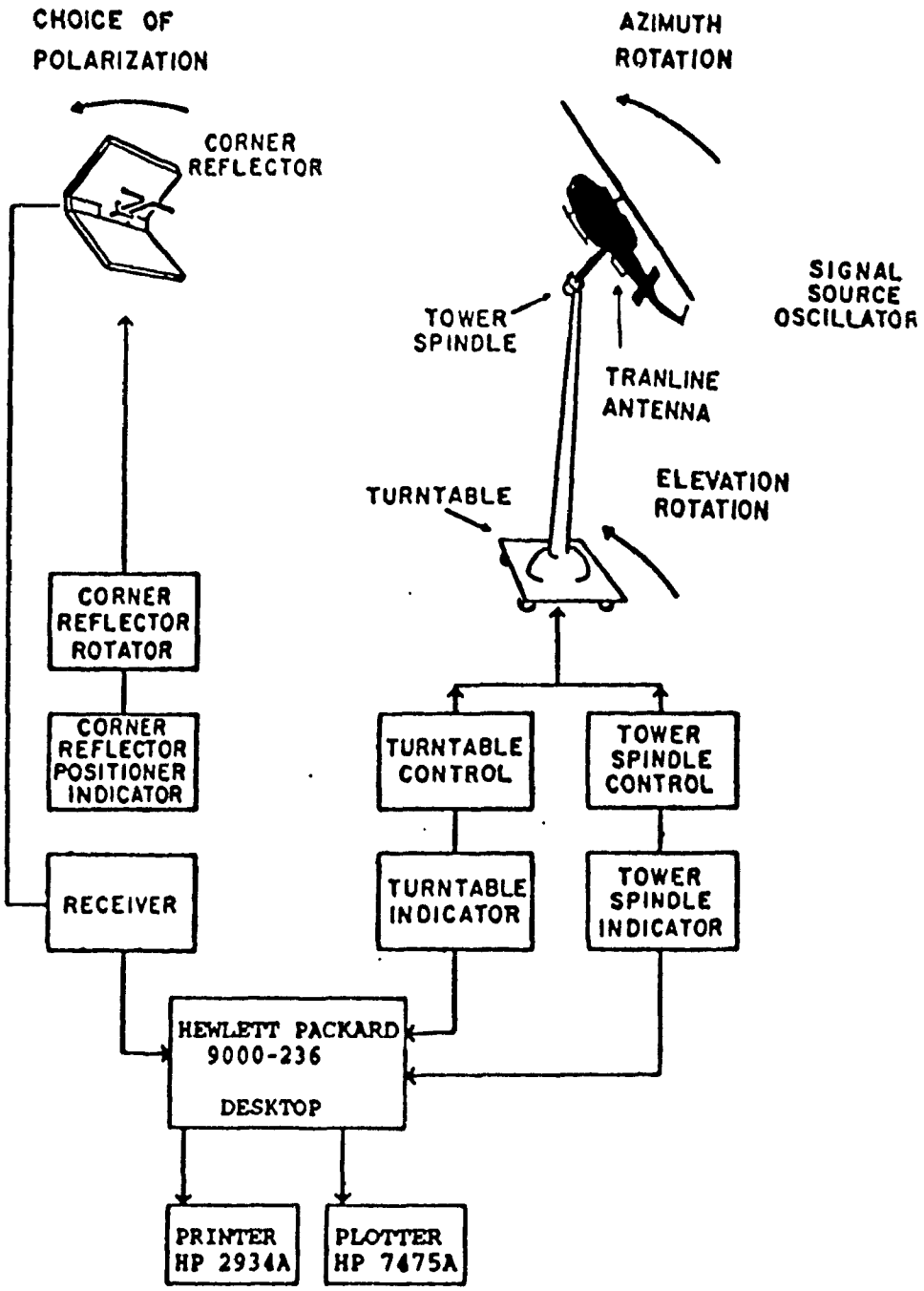

Figure 3-7 NRC antenna measurement range block diagram.

3.2.2 Measurement Setup

A common problem encountered during radiation pattern measurements of test-antennas is distortion of patterns due to stray reflections from the ground and near-by objects. The shielding used for ground reflections was a metallic mesh screen with mesh size of less than $\lambda/10$ over a wooden platform. A mesh is placed at locations where the received signal from a square metallic sheet would have a large amplitude[41]. To shield against reflections from near-by objects, microwave absorbers were used. The absorbers are made up of materials which attenuate the reflected wave by 20 dB in the 0.3 to 40 GHz range[37]. Experimentation is required in setting up the absorbers, so that an optimum level of shielding may be achieved.

Once the transmitter and receiver are setup and operational, radiation pattern measurements are taken in accordance with MIL-A-9080(USAF)[42]. It requires three principal plane patterns and conical cuts for θ= 0, 25, 37, 45, 53, 60, 66, 72, 84, 96, 102, 108, 114, 120, 127, 135, 143, 155, 180 degrees for both E_θ and E_ϕ. Figures 3-9, 3-10 and 3-11 illustrate measurement setup for the three principal plane axes. Please note however that the model used in these figures is that of CHSS-2 Sea-King

helicopter[37]. These figures are official photographs of

Figure 3-8 Receiver antenna of NRC range (official photograph of NRC, print no. 9536C).

NRC and were only provided for the Sea-King helicopter.

They are used to demonstrate the measurement setup, which is the same for all models. The description for each figure is included in the figure itself.

3.3 Model Validation

The last step in completion of a numerical wire-grid model is its validation. This is the step in which the theoretical basis of modelling guidelines and the wire-grid model, which is derived according to these guidelines, is tested and certified. Once the model is validated, it is verified that it has the same electromagnetic response as that of the actual helicopter. Model validation is done in two steps; internal and external. Internal validation is evaluating the results on the basis of its own merit[14]. This consists of examining the results, such as current distribution or radiation patterns, to find obvious incompatibilities with actual physical behaviour. Parasitic currents on wire-grids are an example of this situation. External validation on the other hand, is performed by comparing the results of either full scale[44] or scale-model measurements with that of the wire-grid model. Various display programs developed at EMC laboratory are utilized for this purpose. Outputs from these programs, for both measured and computed data,

Figure 3-9 PRINCIPLE PLANE-PITCH AXIS

The helicopter was mounted on the model tower as shown. Looking from the receiving antenna, the top of the craft is seen; the turntable (ϕ) is set at 0° and represented at the top of the polar chart by 0°. The helicopter is mounted on the stand so that the fore-aft axis is horizontal with the nose to the left. The spindle angle is referred to as ψ, and this position is ψ=0°. The initial pattern is taken with ψ=0° (fixed) and ϕ varied through 360°. The turntable is rotated in a counterclockwise direction so that at 0° we are looking at the top; at 90° - forward; at 180° -bottom; and at 270° -aft on the polar chart. In this configuration, the aircraft is being rotated about its pitch axis.

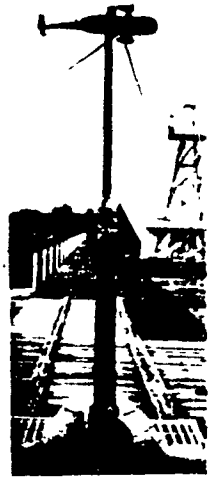

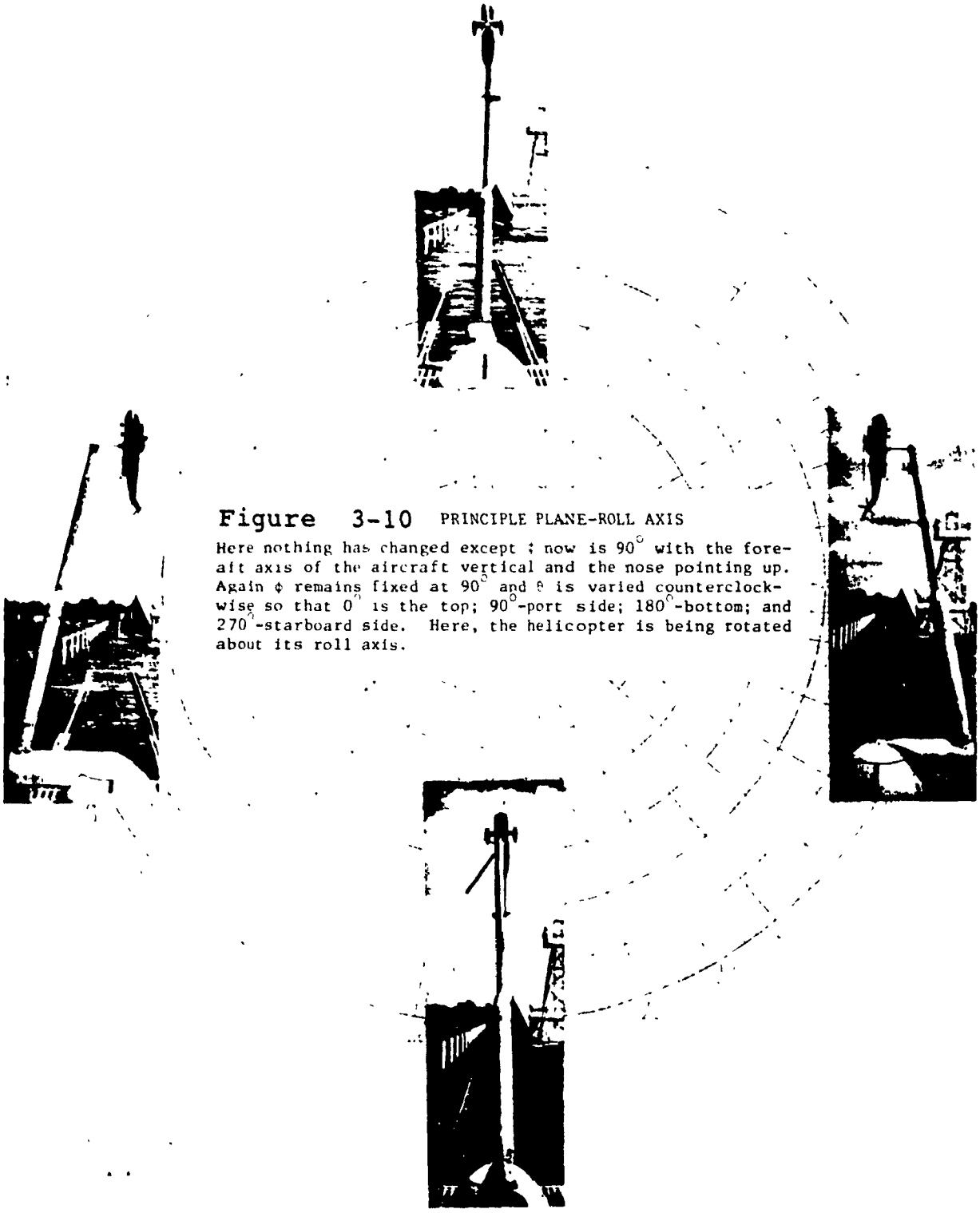

Figure 3-10 PRINCIPLE PLANE-ROLL AXIS

Here nothing has changed except ψ now is 90° with the fore-aft axis of the aircraft vertical and the nose pointing up. Again ϕ remains fixed at 90° and θ is varied counterclockwise so that 0° is the top; 90°-port side; 180°-bottom; and 270°-starboard side. Here, the helicopter is being rotated about its roll axis.

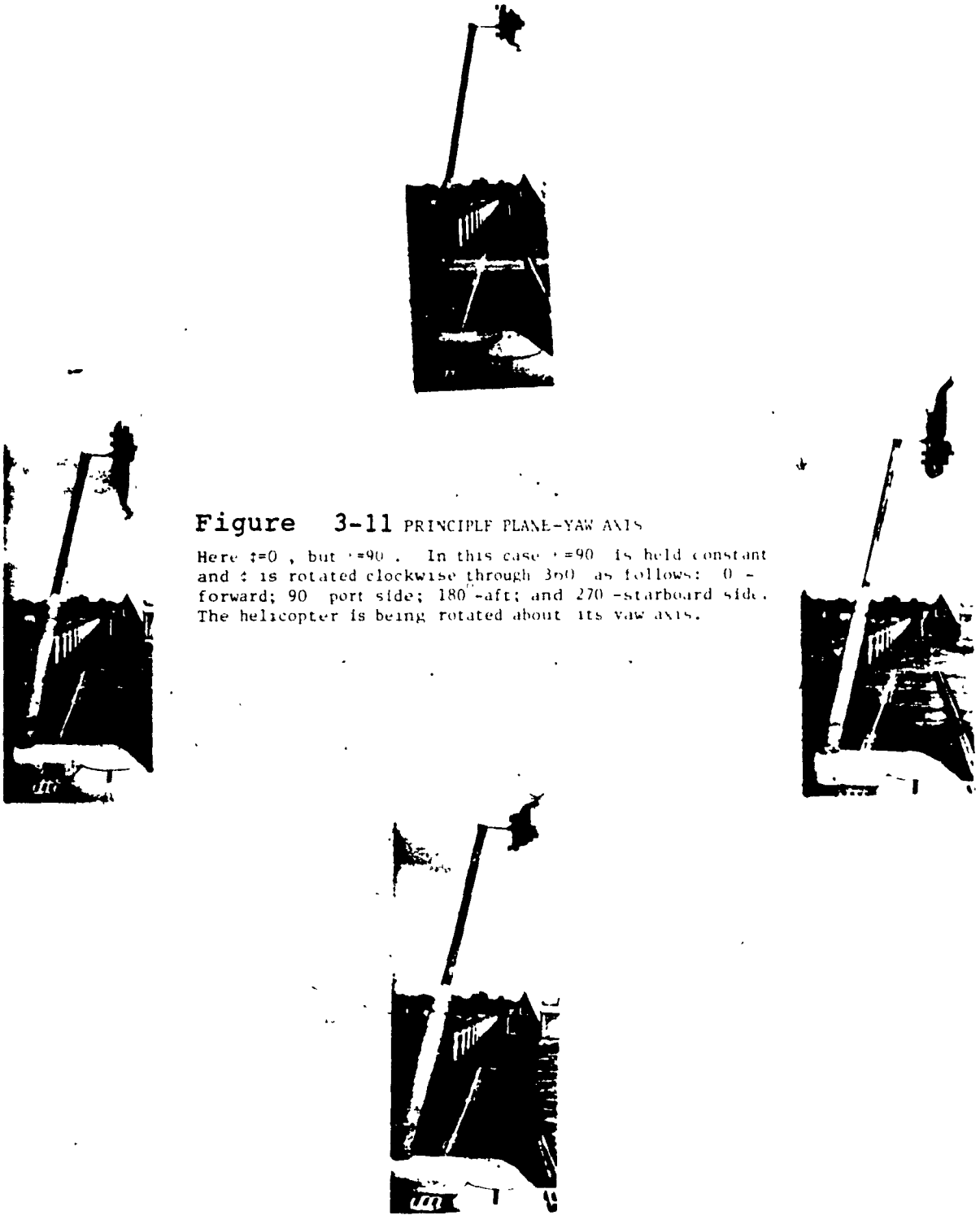

Figure 3-11 PRINCIPLE PLANE-YAW AXIS

Here ‡=0 , but ·=90 . In this case ·=90 is held constant and ‡ is rotated clockwise through 360 as follows: 0 - forward; 90 port side; 180 -aft; and 270 -starboard side. The helicopter is being rotated about its yaw axis.

provide the tools for a meaningful comparison. Almost all display programs at EMC laboratory display their patterns relative to what is knows as "isotropic level". Therefore, before describing these programs, the concept of isotropic level must be mentioned.

3.3.1 Isotropic Level and Radiated Power

Any meaningful comparison between the computed and measured patterns must be done with respect to a certain criteria. This criteria, known as the Isotropic Level, is the field radiated by an isotropic antenna[45]. It is an omnidirectional field, radiated in only one polarization, with the same total radiated power as the antenna being measured. This parameter, amongst other parameters, is calculated by the program ISOLEV.

3.3.1.1 ISOLEV

The program ISOLEV [46], which is used extensively at EMC laboratory, requires a NEC solution file as input and calculates the radiated power, isotropic level and a set of performance parameters for HF aircraft antennas. The calculated parameters are then reinserted into the solution file to be used later for comparison purposes.

The total radiated power is obtained by taking the

closed surface integral of the average Poynting vector over any surface enclosing the antenna[45], and is given by

$$P_r = \oint_S \bar{S}_{avg} \cdot d\bar{S} \qquad (57)$$

using a closed spherical surface, of radius one meter, centered on the helicopter, (Figure 3-6), eqn.(57) may be reduced to

$$P_r = \frac{1}{2\eta} \int_{\phi=0}^{2\pi} \int_{\theta=0}^{\pi} [|E_\theta(\theta,\pi)|^2 + |E_\phi(\theta,\pi)|^2] SIN\theta \; d\theta d\phi \qquad (58)$$

where η is the characteristic impedance of the medium, which is 120π ohms[37]. E_θ and E_ϕ are measured or computed field values. ISOLEV computes the value of radiated power from a set of azimuth patterns available in the solution file.

The radiated power may also be expressed in terms of the isotropic field magnitude, $|E|$;

$$P_r = \frac{1}{2\eta} \oint_S |E|^2 dS \qquad (59)$$

since isotropic field is omnidirectional, for a sphere of one meter radius, equation (59) may be written as

$$P_r = \frac{2\pi |E|^2}{\eta} \qquad (60)$$

the isotropic level is derived to be

$$|E| = [\frac{1}{4\pi} \int_{\phi=0}^{2\pi} \int_{\theta=0}^{\pi} (|E_\theta(\theta,\phi)|^2 + |E_\phi(\theta,\phi)|^2) SIN\theta \; d\theta d\phi]^{\frac{1}{2}} \qquad (61)$$

In addition to isotropic level and total radiated power, a set of performance parameters for HF aircraft antennas is evaluated by ISOLEV. These parameters are used to assess the electromagnetic performance of the aircraft as a radiator. They are calculated at a single frequency and are usually plotted for the entire HF band. The theoretical derivation of performance parameters is on the basis of the aircraft flight habits and the nature of HF communication beyond the line of sight.

HF communication is accomplished using both ionospheric skywave and ground-wave propagation modes. In the skywave mode of propagation, which is the dominant mode, the electromagnetic wave from the antenna is transmitted towards an ionic level at an oblique angle. The incident wave then is reflected, at the same oblique angle, from the ionic layer back toward the receiving antenna[47]. This is shown in Figure 3-12. Although the term reflection is commonly used for convenience, the wave is not reflected and is bent backwards toward the earth by refraction, just as a prism refracts light. The bending process is in accordance with Snell's law and is a function of the refractive index of the ionic layer in the ionosphere[47]. The ionosphere is a sparse region which extends from around 50 Km to around 400 Km in altitude, and during daylight hours is bombarded by solar radiation so

that the rarefied air becomes ionized by the ultra-violet and X-ray emissions[48]. Several layers are formed as a result of ionization. The upper layers reflect radio waves

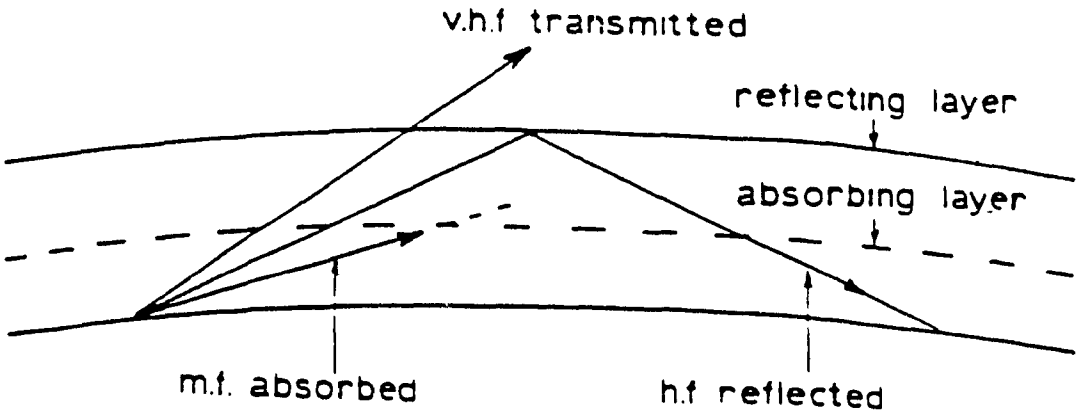

Figure 3-12 Reflections from the ionosphere[48].

while the lower layers attenuate the wave passing through them[48]. In the ground-wave mode of communication the energy is propagated along the curved surface of the earth. When propagating beyond the line of sight, the conductivity of the earth surface acts as a waveguide and bends the wave around the curved surface[47]. It is important to note that the ground-wave, which most commonly occurs at HF, is not a true surface wave and is not bound to the surface in the same way as a microwave surface wave over a corrugated dielectric-clad conducting sheet[48]. Since horizontal

polarization results in extremely high losses due to a short circuit effect of the earth[47], this ground wave is vertically polarized, and is automatically launched by any vertically polarized radiator having a significant field component at zero elevation angle[48]. Figure 13-3

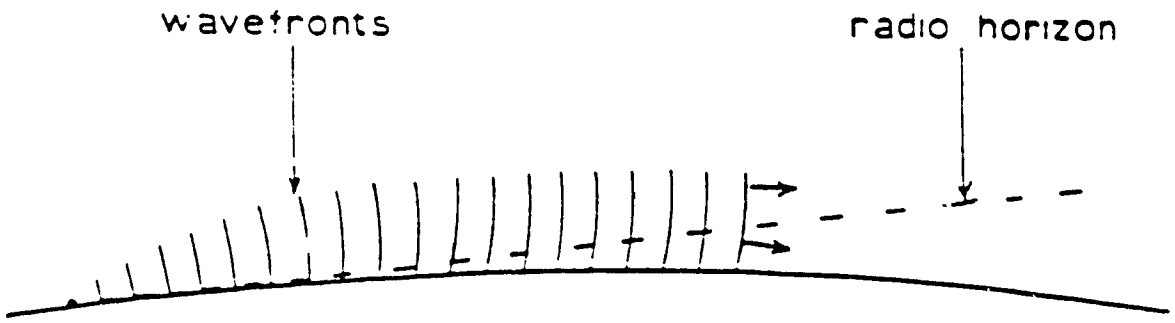

Figure 3-13 Ground-wave propagation at HF [48].

illustrates the ground-wave propagation at HF. It should be noted that since the velocity of the wave in free space is slightly more than that in the earth's surface, the phase fronts are tilted slightly forward, as in Figure 3-13, and the direction of propagation is curved downwards[48].

The analysis of energy distribution requirements of HF antennas for long distance communication on aircraft, leads to the introduction of a parameter called Radiation Pattern Efficiency, η_r. It is defined as the ratio of power

radiated in the sector $60° < \theta < 120°$ in both E_θ and E_ϕ, to the total power radiated by the antenna[49]. It is expressed as

$$\eta_p = \frac{\int_0^{2\pi} \int_{60}^{120} (|E_\theta|^2 + |E_\phi|^2) SIN\ \theta\ d\theta d\phi}{\int_0^{2\pi} \int_0^{\pi} (|E_\theta|^2 + |E_\phi|^2) SIN\ \theta\ d\theta d\phi} \times 100\% \qquad (62)$$

As mentioned before, in the ground-wave mode of HF propagation, the vertical polarization is the dominant factor. Therefore, in order to achieve an optimum level of efficiency in ground-wave propagation, the vertical component of radiation must be maximized. The performance parameter used to define the ratio of radiated power in the vertical component to the total power radiated by the antenna[42], denoted by $\%E_\theta$, is defined as

$$\%\ E_\theta = \frac{\int_0^{2\pi} \int_0^{\pi} |E_\theta|^2 SIN\ d\theta d\phi}{\int_0^{2\pi} \int_0^{\pi} (|E_\theta|^2 + |E_\phi|^2) SIN\ \theta d\theta d\phi} \times 100\% \qquad (63)$$

The last HF performance parameter, calculated by ISOLEV, is the ratio of power radiated in the vertical polarization in the solid angle of $60° < \theta < 120°$ to the total radiated power[50], called SUB-$\%E_\theta$, is defined as

$$\%E_{\theta}^{\circ} = \frac{\int_{0}^{2\pi}\int_{60}^{120} |E_{\theta}|^{2} SIN\,\theta d\theta d\phi}{\int_{0}^{2\pi}\int_{0}^{\pi} (E_{\theta}^{2} + E_{\phi}^{2}) SIN\,\theta d\theta d\phi} \times 100\% \qquad (64)$$

3.3.2 Validation of Wire-Grid Model

The parameters, calculated by ISOLEV, are incorporated in various display programs to produce graphics hardcopies, through which computed data could be compared with measured results. Performance parameters are the first set of parameters which provide meaningful results in terms of comparison. They are displayed by the program RPLOT.

The most common program used at the EMC laboratory to produce graphics is RPLOT. Both linear and logarithmic scaling options are provided. Figure 3-14 shows three plots produced by RPLOT for the case of TRANLINE installation on BELL CH-135 helicopter. Figure 3-14(a) is a comparison between the measured and computed radiation pattern efficiencies for the HF band. Figures 3-14(b) and 3-14(c) show comparisons of $\%E_{\theta}$ and SUB-$\%E_{\theta}$, respectively. As demonstrated by the figures, a very good agreement exists between the measured and computed results. In the case of R.P.Efficiency, a maximum difference of 4% exists at 10 MHz. The results of $\%E_{\theta}$ and SUB-$\%E_{\theta}$ are somewhat

similar. A maximum difference of 15% is noted at 12 MHz in $\%E_\theta$ plot, where as a maximum difference of only 10% is noted at 12 MHz in SUB-$\%E_\theta$ plot. From all three plots, it is noted that in the lower (2 to 10 MHz) and higher (26 to 30 MHz) portions of the HF band, an excellent agreement exists between measured and computed results. This indicates that most of the modelling guidelines requirements are satisfied. In the mid region (12 to 24 MHz) of the HF band, a maximum difference of 7% is observed (Fig 3-14(c)).

A comparison between the far field radiation patterns of measured and calculated results may be done by the program SURPAT (surface pattern). SURPAT is the flat representation of three dimensional radiation patterns, very much like a flat map of the entire earth. It represents the variation in amplitude of either E-theta or E-phi with respect to both phi and theta angles. Shown in Figure 3-15, are both field components of calculated and measured values at 16 MHz, which is the mid range of the HF band. When comparing SURPAT plots, one must look for the differences between amplitudes and the existence of hills and valleys (lobes and nulls) at a certain theta and phi angle. Looking at Figures 3-15(a) and 3-15(b), it is seen that the patterns, with the exception of minor differences, are very similar. An apparent difference in amplitude is

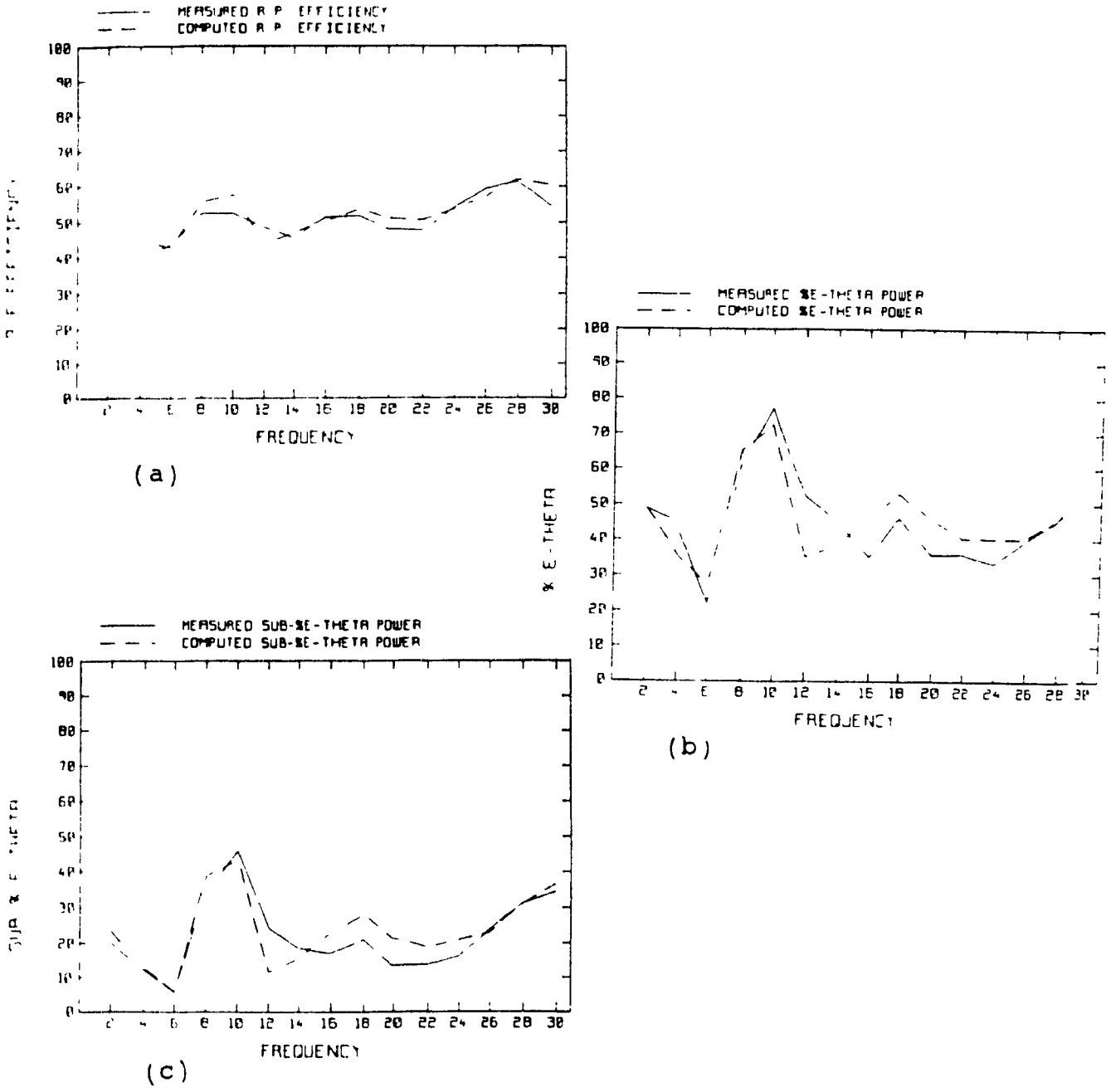

Figure 3-14 Measured and computed performance parameters of BELL CH-135. (a) R.P. Efficiency (b) $\%E_\theta$ (c) SUB-$\%E_\theta$

due to the use of two different isotropic levels. Minor differences in patterns are observed at θ=180, ϕ=180 and θ=90, ϕ=0 degrees. The last mentioned anomaly contributes to the difference in SUB-$\%E_\theta$ values at 16 MHz, as shown in Figure 3-14(c). The phi components of the fields, shown in Figures 3-15(c) and 3-15(d), are quite similar to each other. The overall similarity of patterns reveal how closely the electromagnetic characteristics of the helicopter are imitated by the numerical model. It would be a very long and cumbersome task to compare and comment on all SURPAT plots in the HF band, but for the sake of completeness all the plots are included in Appendix A.

A detailed two dimensional view of the radiation patterns at a certain angle is provided by the program PATCMP (pattern comparison). The user has the option of choosing a conical or an elevation cut. When viewing a conical cut, theta is fixed and phi varies from 0 to 360 degrees. In the case of an elevation cut, phi is fixed and theta varies through 360 degrees in free space, and 180 degrees when over a ground plane. Using navigational terms, the positive x-axis is FWD, the negative x-axis is AFT, the positive y-axis is PORT, the negative y-axis is STB and the positive z-axis is designated as TOP[42]. Keeping the above information in mind, Figure 3-16 shows a PATCMP representation of both measured and computed

results. The theta components of the fields, Figure

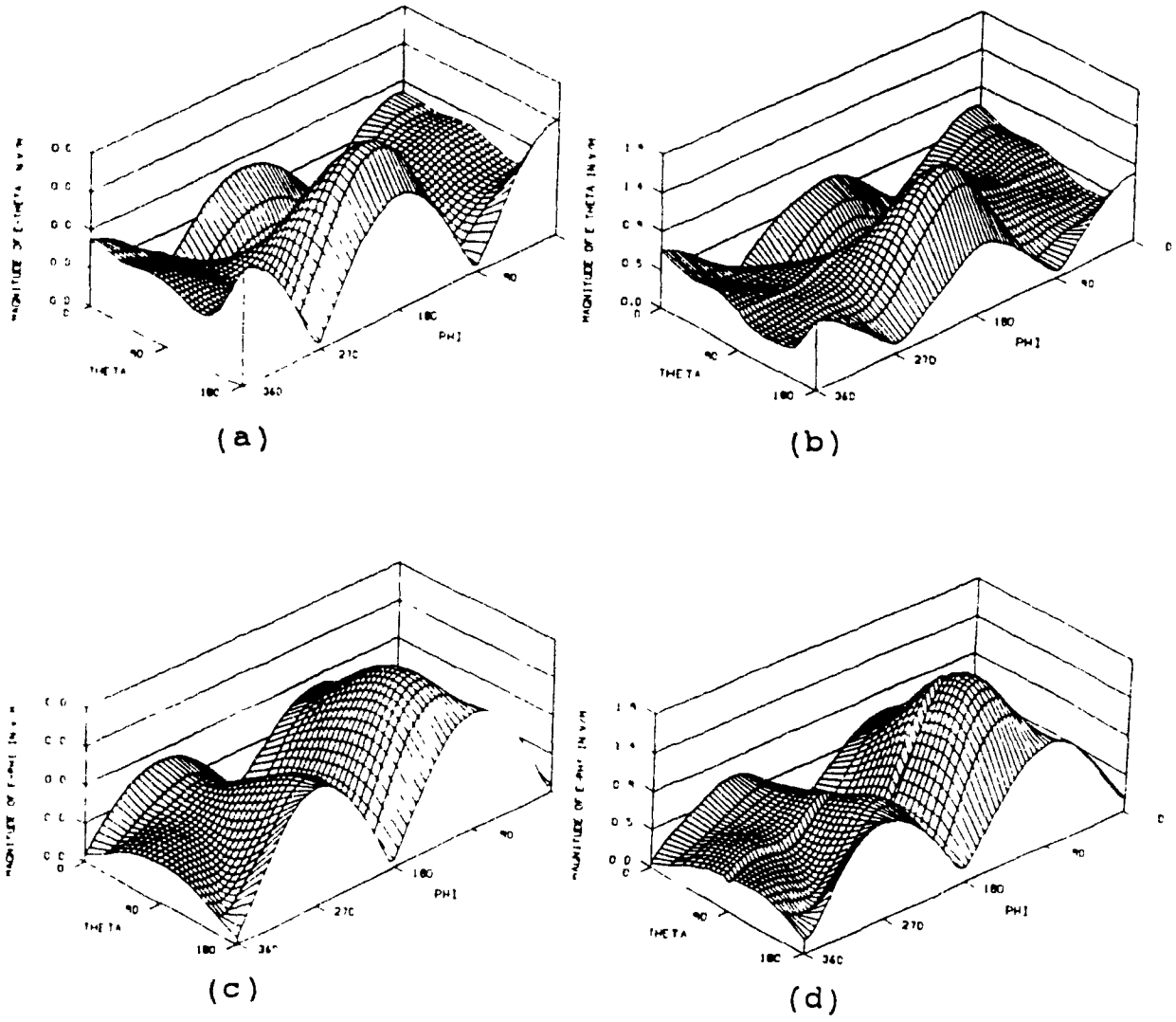

Figure 3-15 SURPAT patterns at 16 MHz. (a) computed E_θ (b) measured E_θ (c) computed E_ϕ (d) measured E_ϕ.

3-16(a) and 3-16(b), are at very good agreements in the plane of θ=0 and 90 degrees. A slight difference of

amplitude exists at θ=90 and φ=0 degrees. This difference was detected earlier in the SURPAT plots. The phi

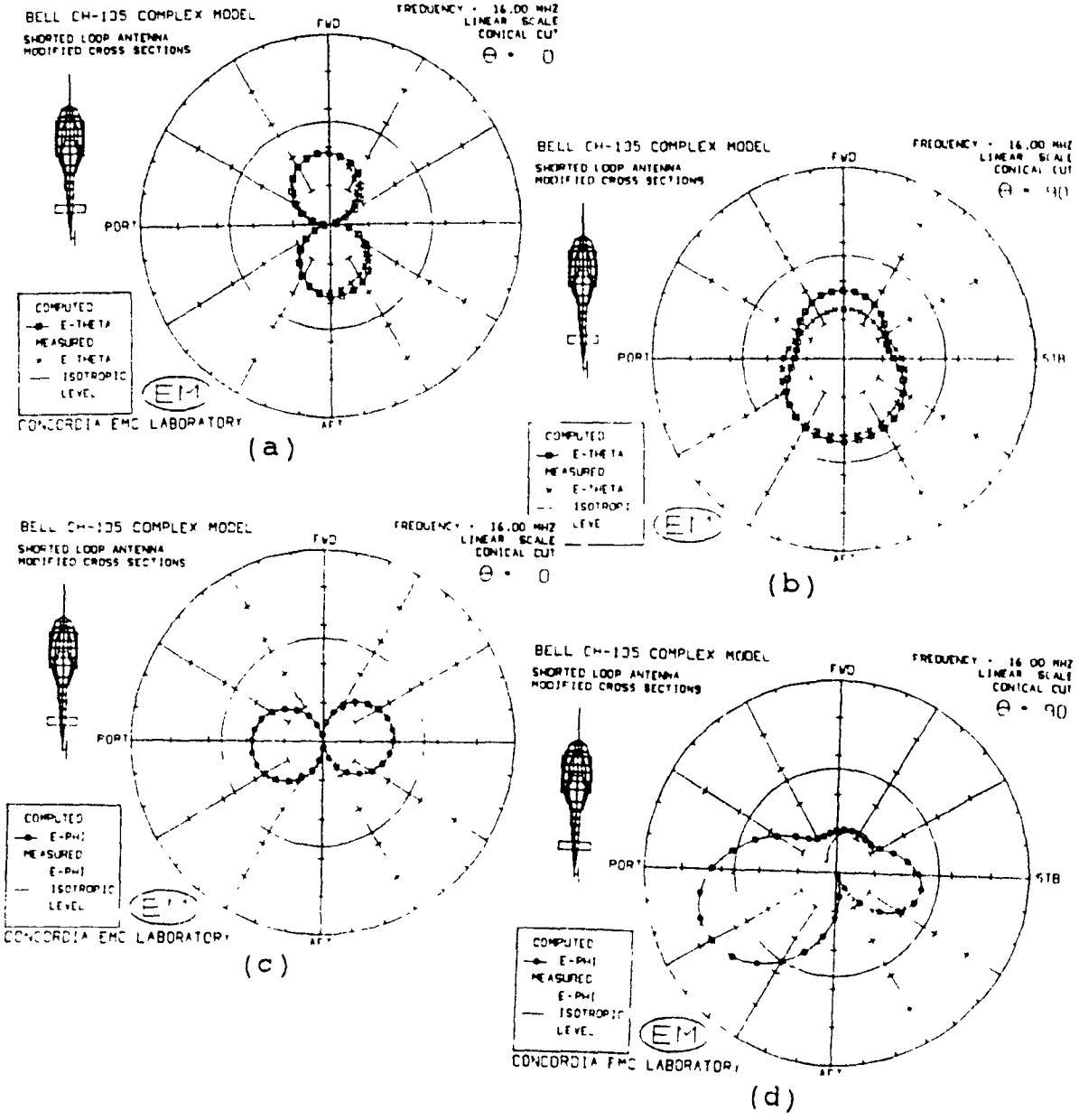

Figure 3-16 PATCMP patterns at 16 MHz of measured vs. computed field at (a) θ=0 for E_θ, (b) θ=90 for E_θ, (c) θ=0 for E_ϕ, (d) θ=90 for E_ϕ.

components, Figures 3-16(c) and 3-16(d), are also very

similar with small differences at θ=90 , ϕ=90 and 270 degrees. Again for the sake of completeness, all the PATCMP plots are included in Appendix B.

Although validation of a numerical model is a task which is never fully complete, the last step in validating the wire grid model of the BELL CH-135, is to compare the calculated input impedance with the measured one throughout the HF band. Since the measured input impedance was only available for TRANLINE antenna, an entire section in the next chapter is devoted to this comparison. It will be shown that an excellent match is obtained between the measured and computed input impedances.

CHAPTER 4

TRANLINE ANTENNA ON BELL CH-135

Two different types of antennas, namely Tranline and Zig-Zag, may be installed on BELL CH-135 helicopter. Zig-Zag antenna is an open-wire antenna which is connected to the fuselage at the feed point and runs around the tail in a zig-zag fashion. Its end is open in the air and not connected to the helicopter. Tranline or shorted loop antenna[51,52] on the other hand, starts at the same feed point, but its end is electrically connected to the fuselage. Figure 4-1 shows the wire-grid model of BELL CH-135 with Tranline antenna indicated by arrows. The antenna is located on the port side of the fuselage, and running aft has an approximate length of 2.3 meters. The wire-grid model of CH-135 with Tranline installation was evolved in two steps.

4.1 Evolution of Tranline Model

The first wire-grid model of BELL CH-135 developed at EMC laboratory[31,53], which in this work is regarded as the old model, had certain deficiencies. In the region of

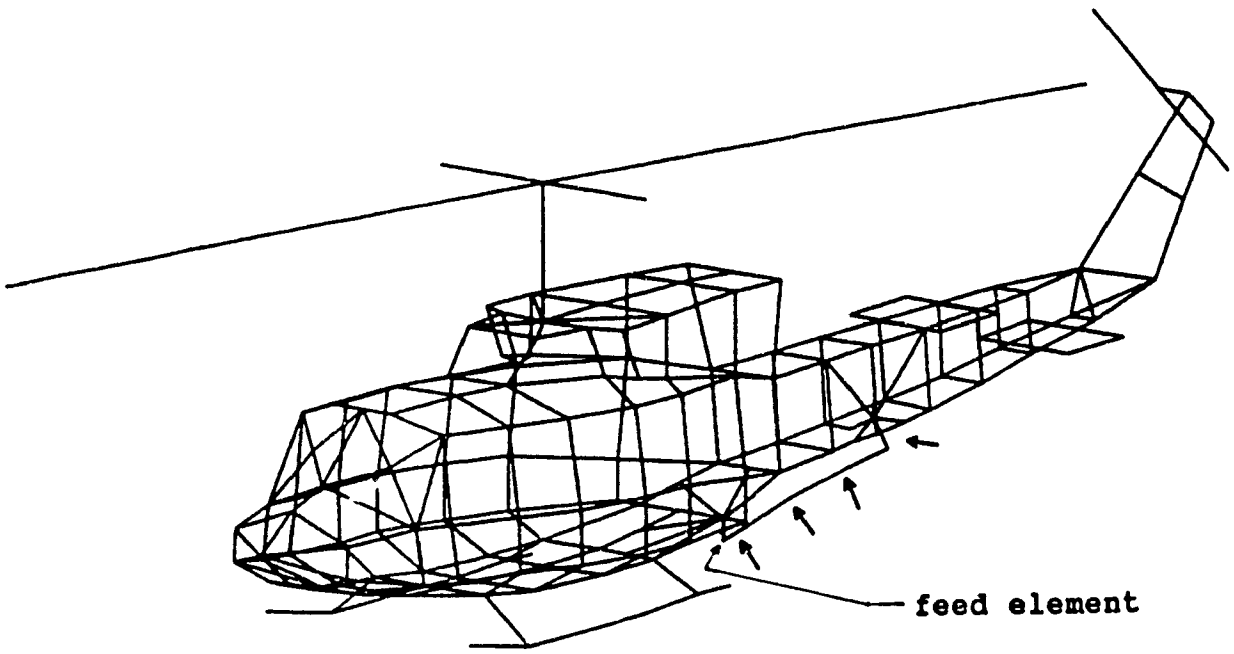

Figure 4-1 BELL CH-135 with Tranline installation (Tranline antenna is shown by arrows).

special interest (6 to 12 MHz), the old model exhibited very poor results. Hence a new model was required to closely represent the measured results, which is essential for model validation. To derive the new model, orthogonal views of the helicopter were re-examined. This resulted in recalculation of wire lengths and radii. The model was carefully studied at all frequencies and wires were added in places where more currents were suspected to flow. Extra wires were added in the feed and join regions and were then tapered off to provide a smooth current flow. The last step was to remove all the errors detected by

program CHECK. Figure 4-2 illustrates the differences

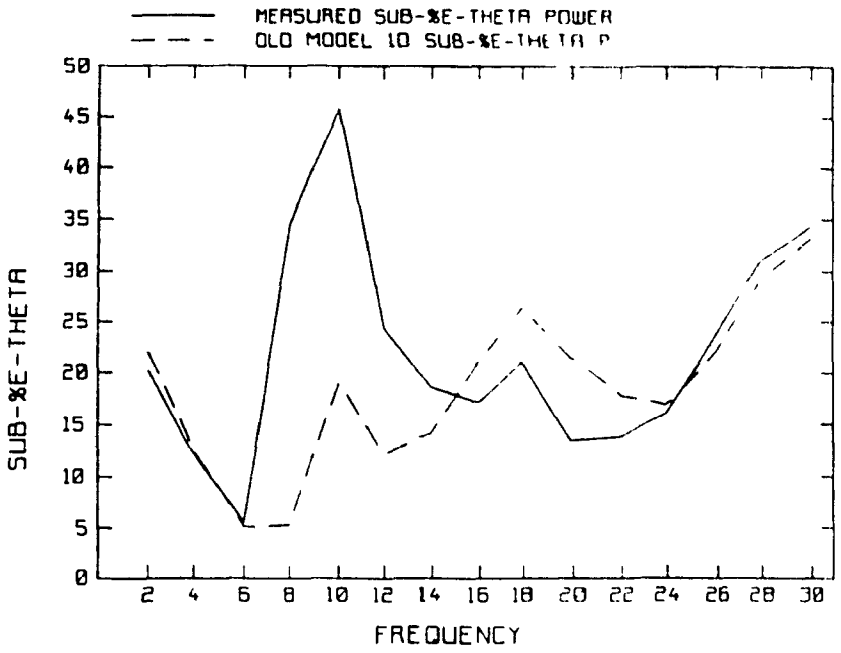

(a)

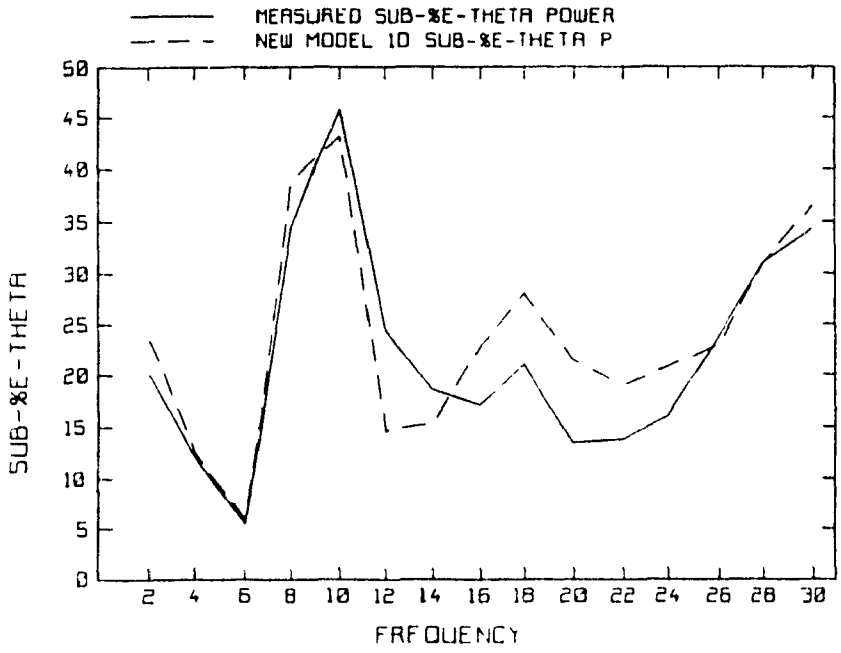

(b)

Figure 4-2 A comparison between the measured results and (a) the old model (b) the new model.

between the old and the new model values of SUB-%E_θ power, using the measured results as criterion. A very good improvement is observed in the region of special interest. At 8 MHz the old model exhibits a SUB-%E_θ value of only 5%, whereas the new model radiates about 38% at the same frequency. It must be mentioned that this improvement was obtained after adding an extra element to the wire-grid model, namely "the rod". The logic behind addition of this element will be discussed in the next section. Another improvement in performance of the new model over the old one is observed at 10 MHz, where the SUB-%E_θ power has increased from 18% to 43%. This is only 3% short of the measured result. Figures 4-3 and 4-4 are outputs of the program CONTSF, and compare the old and new model theta and phi components at 10 MHz, respectively. CONTSF is another graphic program used at EMC laboratory and produces a three dimensional colour representation of the far field radiation. The red spots are where the field is very strong (lobes), and the blue spots are where the field is weak (nulls). The magnitude of each colour is shown above the figure. It must be noted that parts (a) and (b) of figures 4-3 and 4-4 can not be directly compared together. This is because they do not share a common scale, that is the red colour in part (a) does not represent the same field intensity in part (b). But figures may be compared

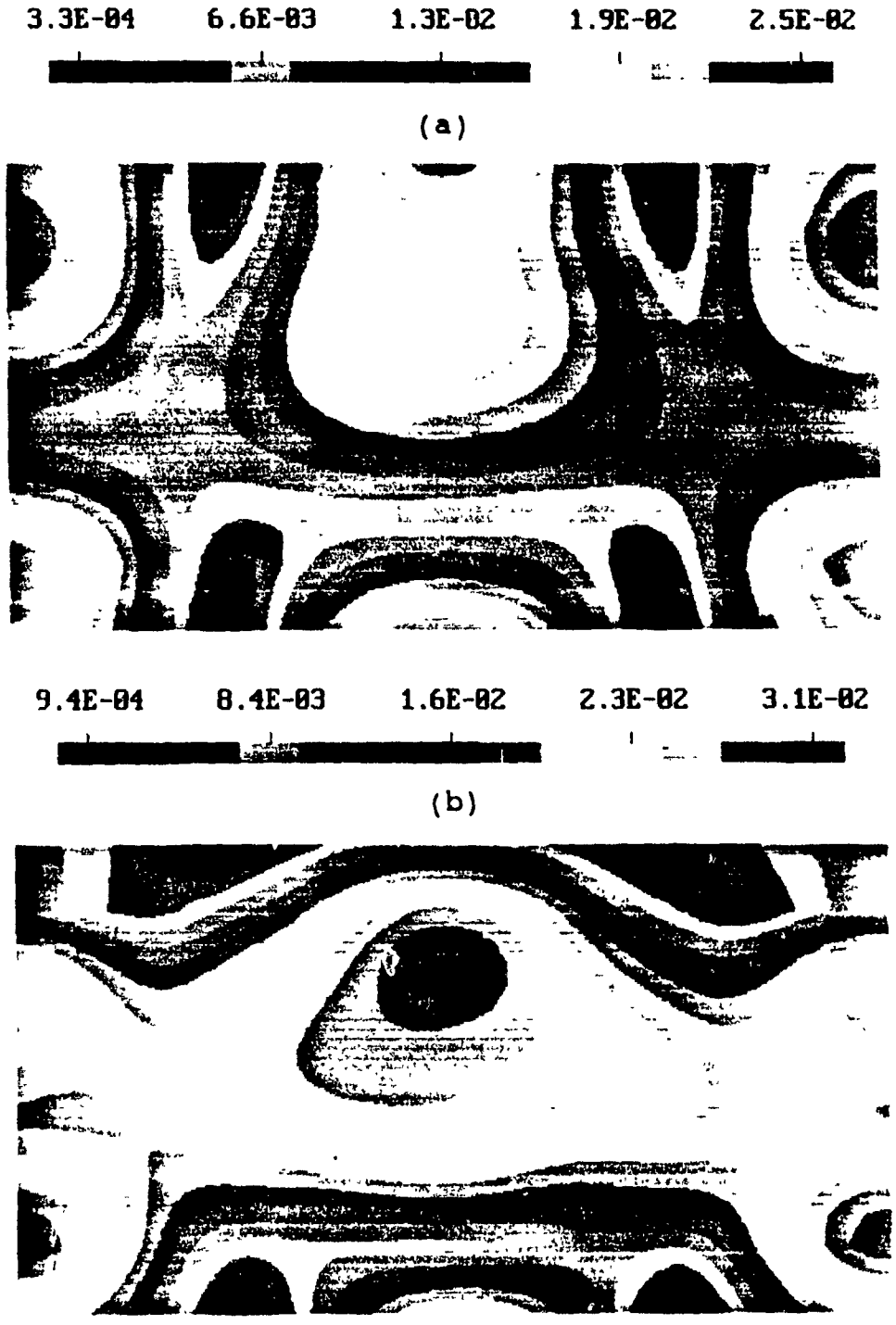

Figure 4-3 E_θ of (a) old model (b) new model.

in a relative fashion to provide some information about the differences at 10 MHz. In this case, figures 4-3 and 4-4 demonstrate that both E_θ and E_ϕ components of the fields produced by the new and old models are indeed very different at 10 MHz, as expected from figure 4-2.

4.2 The Effect of The Rod

The measured data of BELL CH-135 were obtained by mounting a scale model of the helicopter on the NRC range and measuring the radiated field. The scale model was connected to the range tower by means of a connecting rod, which is shown by an arrow in figure 3-5. Discrepancies observed between measured and computed results at certain frequencies, lead to a re-examination of the electromagnetic characteristics of the rod. Since electrical current flows on any conducting path, the rod was theoretically expected to be composed of material that would not support a current flow. It was not supposed to be a conductor, as it was later found to be. The measurements for Tranline antenna were done with a conducting rod, and as the problem was rectified, the Zig-Zag antenna measurements were done with a non-conducting rod. Therefore, the wire-grid model for Tranline installation had to be modified to account for the

conductivity of the rod. This new model is shown in figure 4-5. This is the model used for all numerical computations

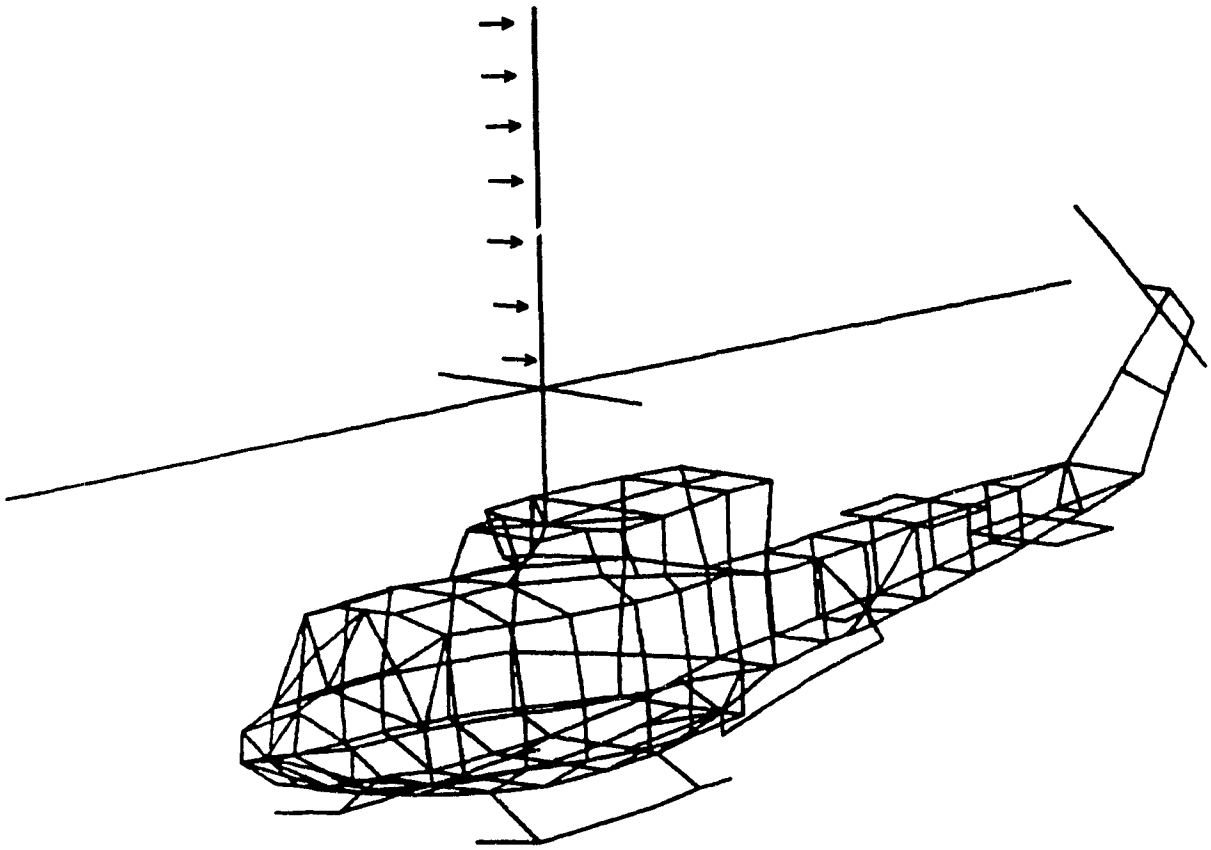

Figure 4-5 Wire-grid model of BELL CH-135 with the connecting rod shown by arrows.

of the field radiated by Tranline installation.

To examine the effect of the rod, a full frequency sweep of the HF band was carried out for both cases, that is when the rod is installed and when it is absent. The

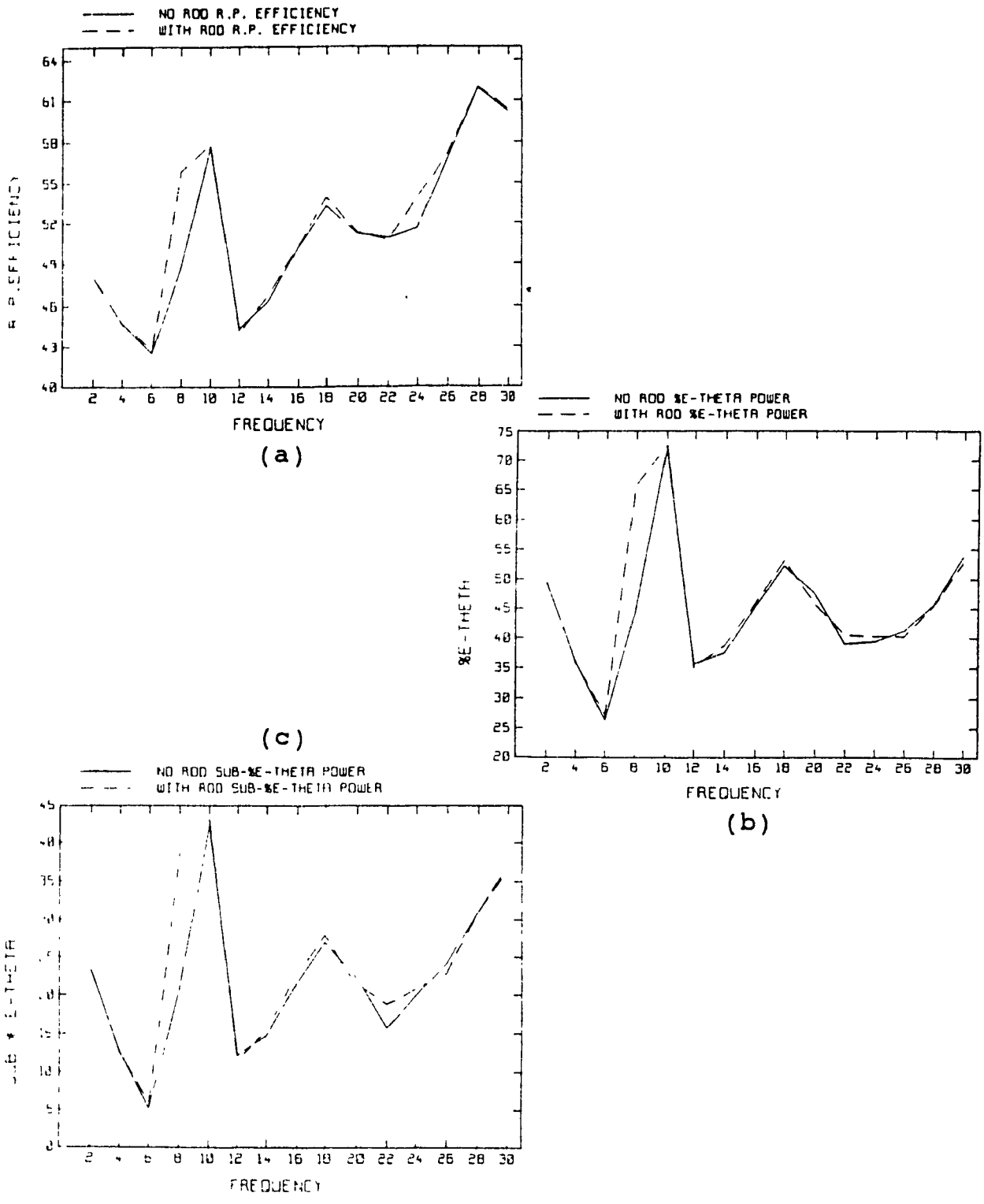

Figure 4-6 Performance parameters showing the effect of the rod. (a) radiation pattern efficiency, (b) $\%E_\theta$ (c) SUB-$\%E_\theta$.

results of comparing the performance parameters were quite revealing, as is shown in figure 4-6. The radiation pattern efficiency, figure 4-6 (a), increased some 18% at 8 MHz and 4% at 24 MHz. Subsequent examination of $\%E_\theta$ and SUB%-E_θ, figure 4-6(b) and (c), revealed a 22% and 19% increase at 8 MHz in the values of $\%E_\theta$ and SUB-$\%E_\theta$, respectively. At this stage, it was known why the large difference between measured and computed results existed when the rod was absent. From the increase in the values of $\%E_\theta$ and SUB-$\%E_\theta$ it is noted that the rod causes major change in the value of vertical component of the radiated field at 8 MHz. A close examination of the difference, due to the rod, between theta components of the fields illustrates this point. PATCMP representation of the difference is shown in figure 4-7. One may notice in figure 4-7(a) that the pattern is shifted by approximately 30 degrees. This indicates a field of the same amplitude and a positional shift of 30 degrees. Figures 4-7(b) and (c) however, maintain the same shape but a large increase in amplitude is observed. This increase gives rise to the differences observed in the values of performance parameters. It is however important to remember that the actual aircraft does not have a rod installed on the top of its rotor, and therefore any computation which is meant to resemble the electromagnetic characteristics of the

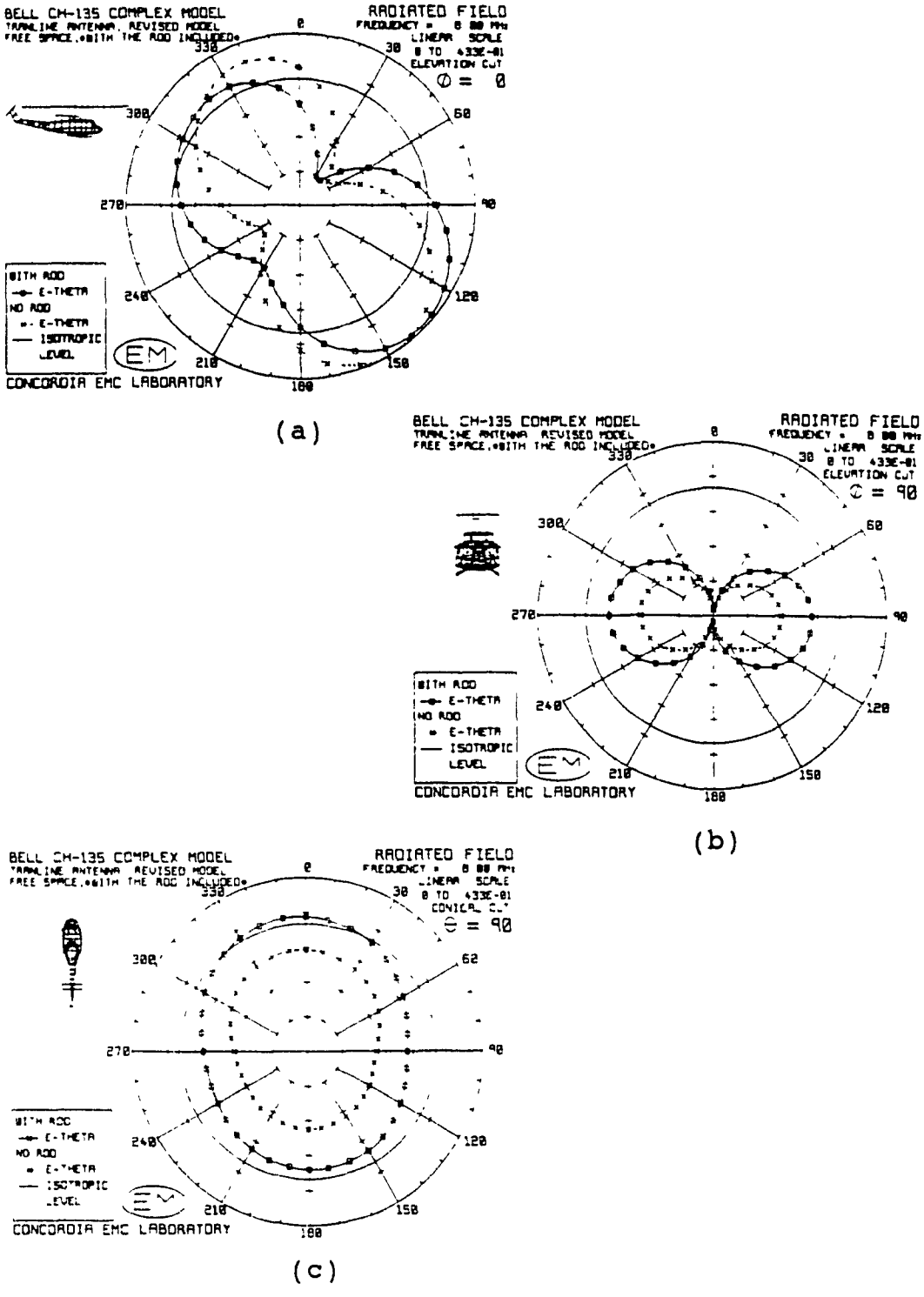

Figure 4-7 Theta components of the fields produced by models with or without the rod at (a) ϕ=0, (b) ϕ=90 and (c) θ=90 planes.

helicopter must be done in the absence of the rod. Such computations may include flying at a certain heights over a perfectly or imperfectly conducting ground.

4.3 The Ground Effect

A helicopter, during the course of its flight, is often required to fly at heights which are comparable to the operating wavelength. In these situations, the assumption of free space conditions is no longer valid and the effect of the ground plane on the radiation pattern must be considered.

When flying near the earth's surface, communication is achieved using ground wave mode of propagation. This is divided into space wave and surface wave modes of propagation. The space wave is composed of a direct wave, which travels directly from helicopter to the receiver, and a reflected wave, which is reflected from the surface of the earth to the receiver. This is shown in Figure 4-8. The surface wave, which is some times called the "Norton surface wave", is a wave that is guided along the earth's surface, much as an electromagnetic wave is guided by a transmission line[39]. The total received signal is the sum of the space and the ground waves.

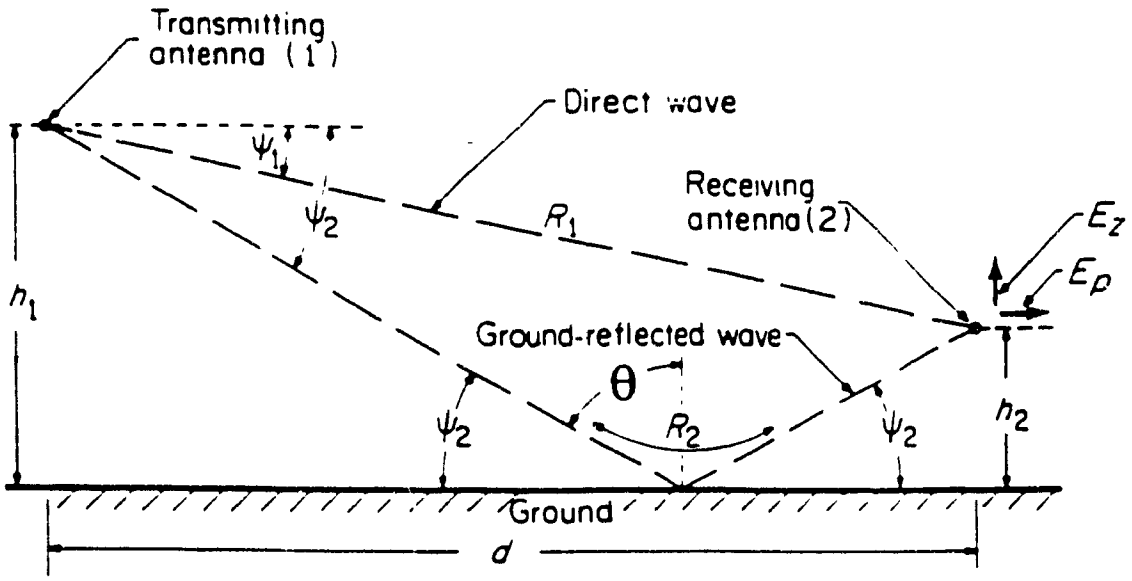

Figure 4-8 Geometry for direct and ground reflected wave[39].

4.3.1 Height and Ground Parametric Variation

Two important considerations in communication are the height above the ground plane and the terrain over the transmission path. The height of the radiating antenna above the earth, H, determines the lobe structure of the radiation patterns. Whenever $H>\lambda$, where λ is the operating wavelength, the lobe structure is very fine; i.e., the angular separation between the lobes is very small[54]. As H becomes more compatible with λ, the angular separation between the lobes increases. The terrain over the transmission path is the earth's surface which bends the

ground wave, and it is the earth's surface which absorbs the RF energy[47]. The terrain parameters considered in this work for the purpose of determining the received field intensity, are earth's relative dielectric constant and conductivity. Table 4 lists some typical values of terrain parameters for common earth surface types.

TABLE 4. TYPICAL VALUES OF TERRAIN PARAMETERS

EARTH SURFACE TYPE	RELATIVE DIELECTRIC CONSTANT	CONDUCTIVITY (Millimho/m^2)
Arctic Ice	3	0.025
Average Land	15	27.800
Dry Soil	4	10.000
Fresh Water	81	5.000
Marsh Land	30	111.000
Sea Water	81	4640.000
Tundra	5	0.400

In this work only the space wave mode of propagation, which is a consideration of direct and ground reflected wave, shown in Figure 4-8, is discussed. This is a general case of oblique incidence and is best undertaken in two parts. In the first part, the electric field vector is considered to be parallel, and the magnetic field vector perpendicular to the reflecting surface. In the second part, the magnetic field intensity is parallel and the

electric field intensity is perpendicular to the reflecting surface. The two cases are often referred to as horizontal polarization and vertical polarization, respectively[55]. The reflection factor R_h for a plane wave having horizontal or perpendicular polarization is given as

$$R_h = \frac{\cos\theta - \sqrt{(\epsilon_r - jX) - \sin^2\theta}}{\cos\theta + \sqrt{(\epsilon_r - jX) - \sin^2\theta}} \qquad (65)$$

where $X=\sigma/\omega\epsilon_o$ and ϵ_r is relative dielectric constant. θ is the angle of incidence measured from the normal to the reflecting surface. In a manner similar to the above, the reflection coefficient for vertical or parallel polarization is given as

$$R_v = \frac{(\epsilon_r - jX)\cos\theta - \sqrt{(\epsilon_r - jX) - \sin^2\theta}}{(\epsilon_r - jX)\cos\theta - \sqrt{(\epsilon_r - jX) - \sin^2\theta}} \qquad (66)$$

From equations (65) and (66) it is evident that the reflection coefficients are complex and that the incident wave will differ both in magnitude and phase from the reflected wave. The manner in which the magnitudes of reflection coefficients for different earth surface types vary with the angle of incidence is shown in Figure 4-9. The phase variation of reflection coefficients with the angle of incidence for a typical earth surface type, such as arctic ice, is shown in Figure 4-10. A close examination of Figures 4-9 and 4-10 reveals that when the

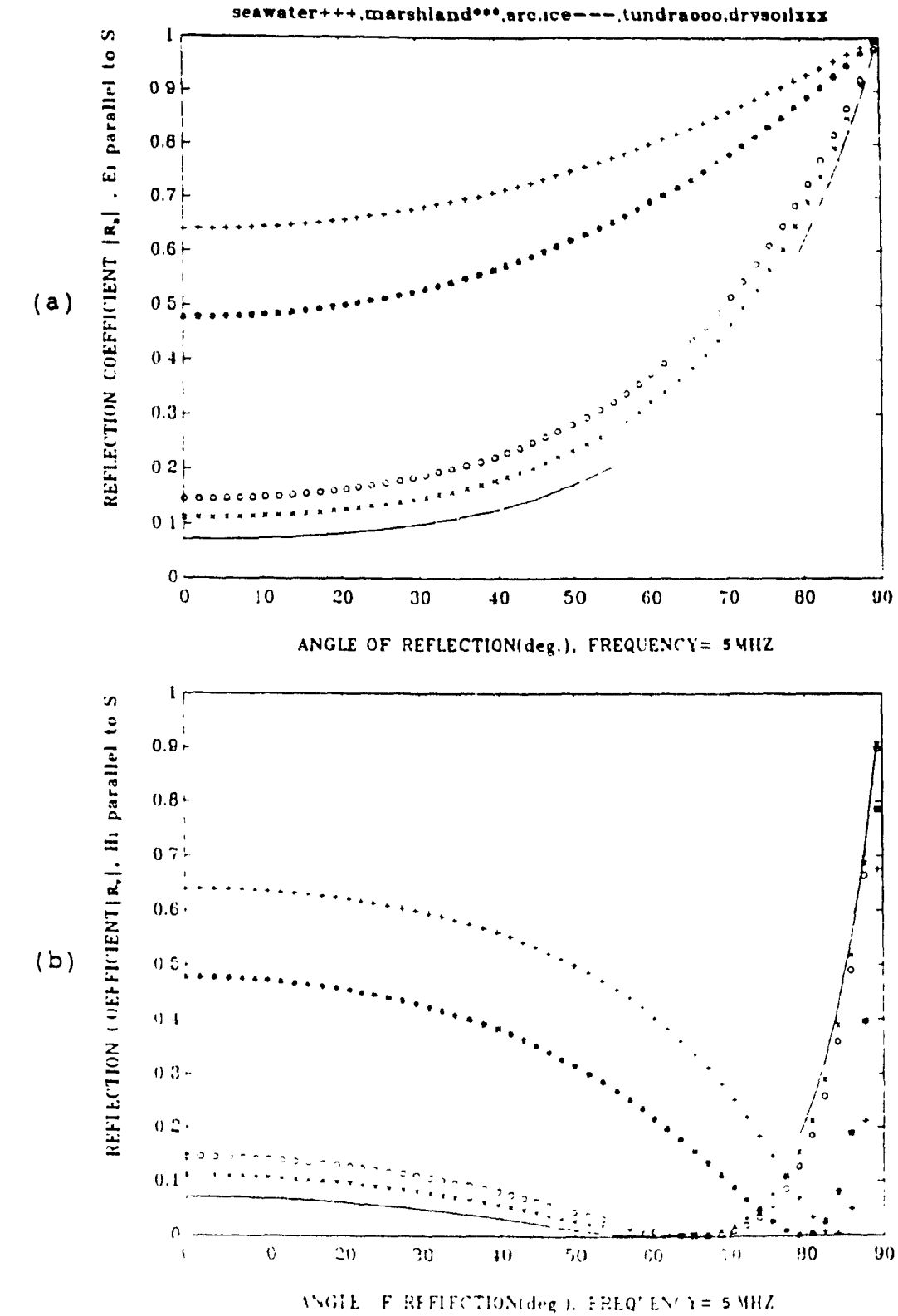

Figure 4-9 Magnitude of plane wave reflection coefficients of various earth surface types for (a) horizontal, and (b) vertical polarization at 5MHz.

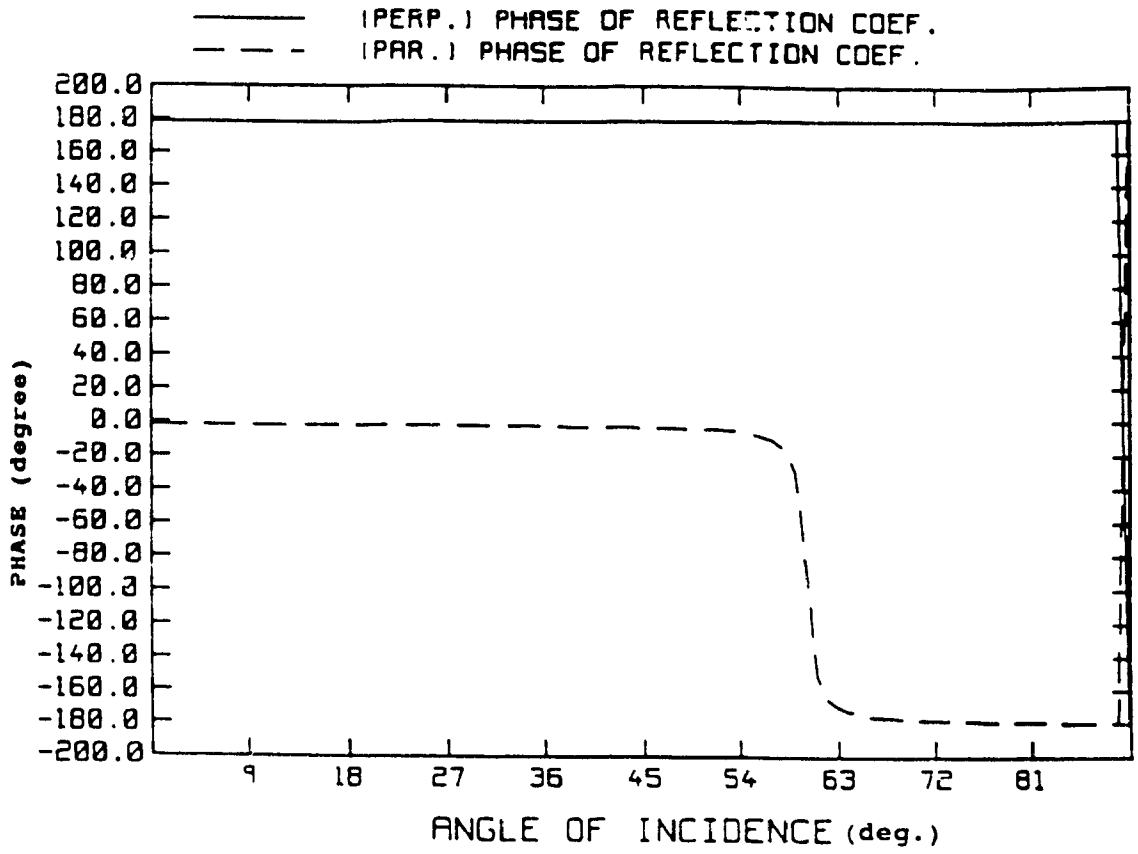

Figure 4-10 Phase of the plane wave reflection coefficient of horizontal (solid line) and vertical (dash line) polarization at 5 MHz for arctic ice.

electric field is parallel to the reflecting surface, the incident and reflected waves are nearly 180 degrees out of phase of all angles of incidence. For angles of incidence near grazing (θ = 90 degrees), the reflected and incident waves are equal in magnitude but 180 degrees out of phase. Although, for the sake of clarity, only the phase information of arctic ice is shown in figure 4-10, its phase characteristics are very similar to that of the other

earth surface types. For the case of vertical polarization, where magnetic vector is parallel to the reflecting surface, the results are different from those obtained for horizontal polarization. At grazing angle, the electric field vectors of incident and reflected waves are equal in magnitude and 180 degrees out of phase with each other. As the angle θ decreases from 90 degrees, the magnitude and phase of the reflected wave rapidly change. The magnitude reaches a minimum and the phase goes through 180 degrees at an angle known as the Brewster angle. At angles of incidence below this angle, the magnitude increases again and the phase approaches zero[39].

The radiation patterns of BELL CH-135 helicopter, flying over different terrains at various heights, are greatly effected by changes in the values of the above mentioned reflection coefficients. Figure 4-11 illustrates theta and phi components of the radiated field at 5 MHz in the separate planes of ϕ=0 and 90 degrees. As mentioned before, true values of radiated field are obtained when the joining rod is not included, and so patterns presented in Figure 4-11 were obtained under this condition. Figure 4-12 shows the difference between the far field patterns calculated over perfect ground and sea water when flying at heights of 1, 15, 30, 100, and 300 meters above the ground. At 5 MHz, these heights are $\lambda/60$, $\lambda/4$, $\lambda/2$, $5\lambda/3$ and 5λ.

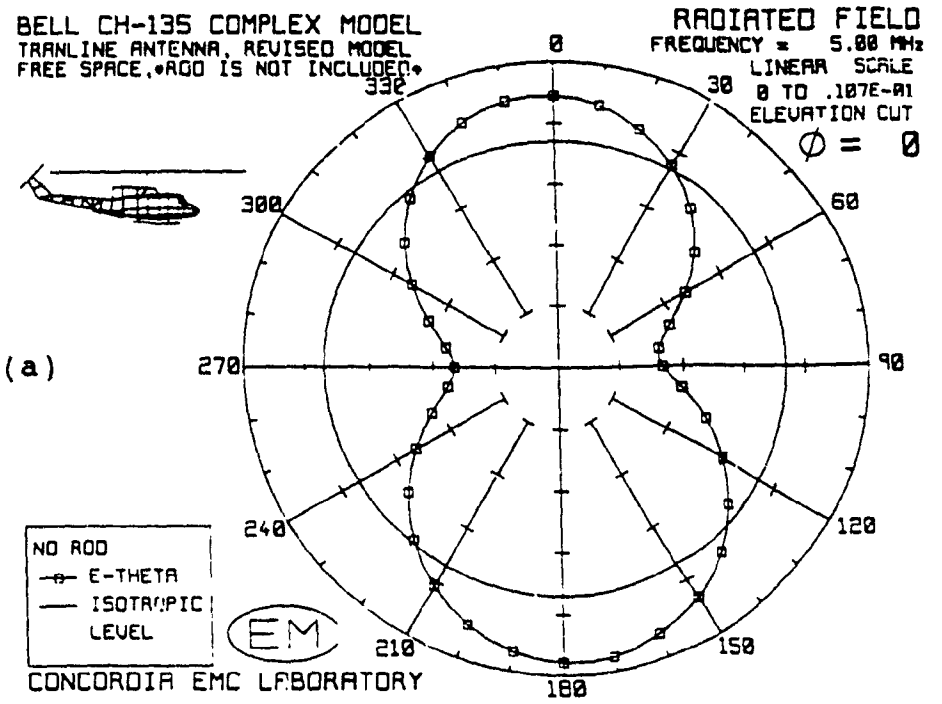

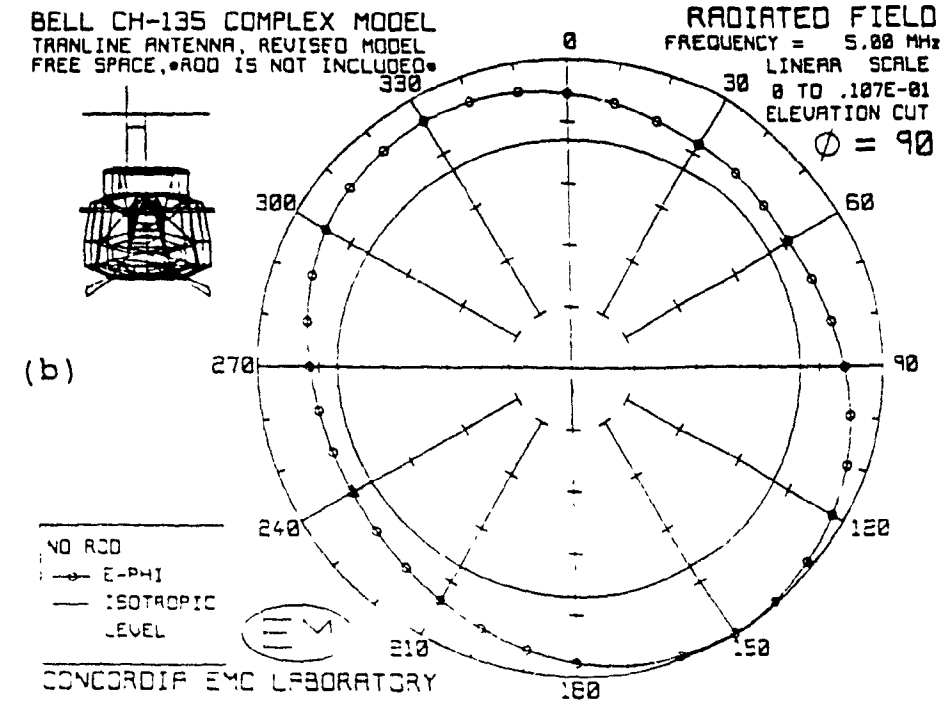

Figure 4-11 Radiation patterns of CH-135 in free space at 5 MHz of (a) E_θ in the plane ϕ=0 degrees and (b) E_ϕ in the plane ϕ=90 degrees.

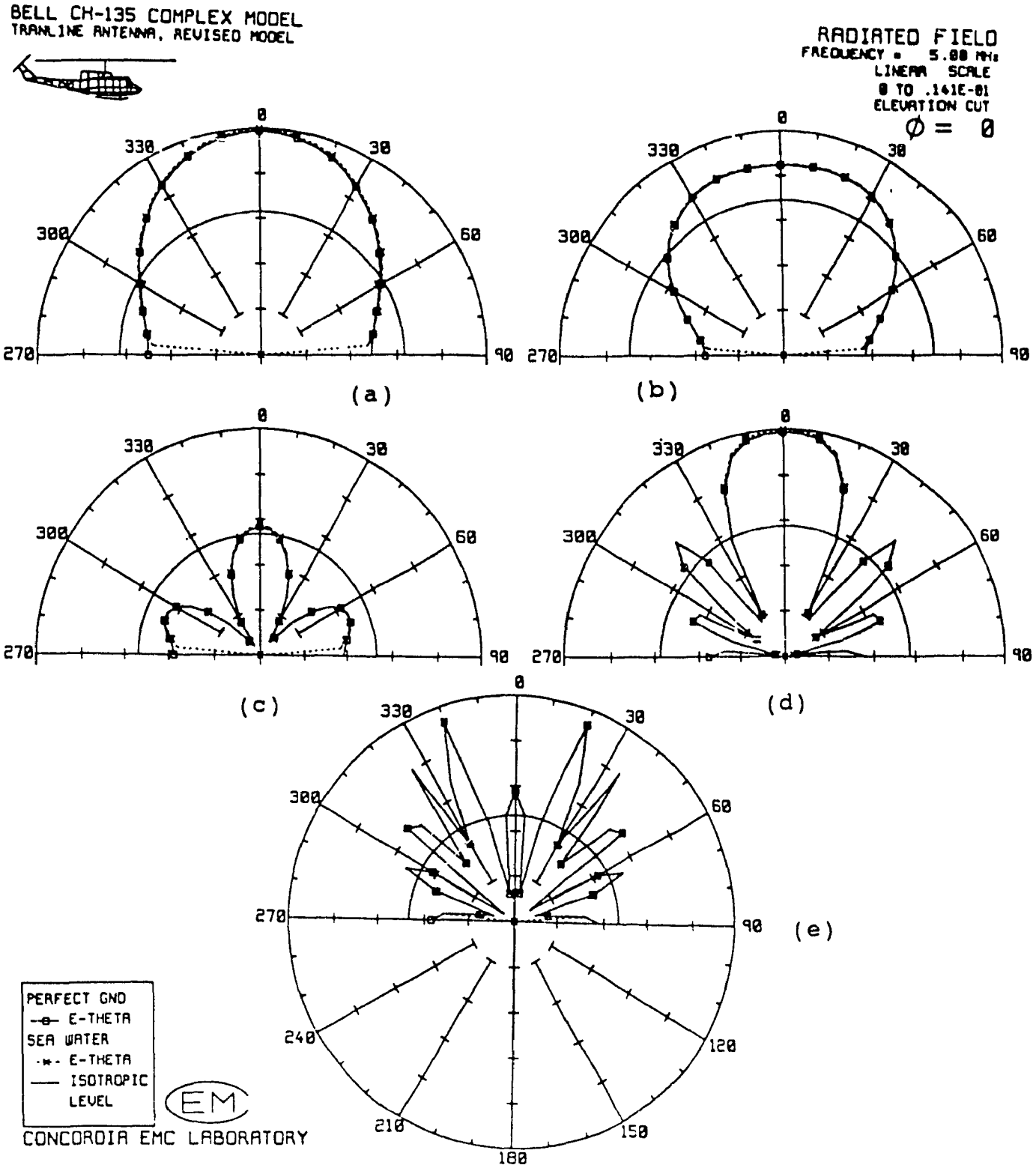

Figure 4-12 E_θ comparison at 5 MHz between perfect ground (solid line) and sea water when flying at (a) H=1m, (b) H=15m, (c) H=30m, (d) H=100m, (e) H=300m above the ground.

respectively. As expected, the number of lobes in the pattern increases with height above the ground. Due to high conductivity of the sea water (Table 4), the patterns are quite similar. At the ground level however, the electric field is perpendicular and finite for the perfect ground, but vanishes in the case of sea water. This is due to the fact that at the surface of a perfect conductor, the tangential component of the electric field vanishes and only the perpendicular component remains. In the case of sea water, because of its finite conductivity, the incident and reflected waves are equal in magnitude and 180 degrees out of phase at the grazing angle, hence the total field vanishes at the ground boundary.

As ground parameters, and conductivity in particular, differ from that of perfect ground or sea water, the shape of the radiated field begins to change. Figures 4-13 and 4-14 separately illustrate the differences in radiation patterns between perfect ground and lossy ground (σ=0.01 mho/m, ε_r=15), and between perfect ground and arctic ice (Table 4), respectively. A close examination of Figures 4-12, 4-13 and 4-14 reveals that the number of lobes in a pattern is really a function of height above the ground. However, as the conductivity decreases, the nulls begin to be "filled", that is, the reflected and incident waves over a lossy ground, at a particular angle, do not approach zero

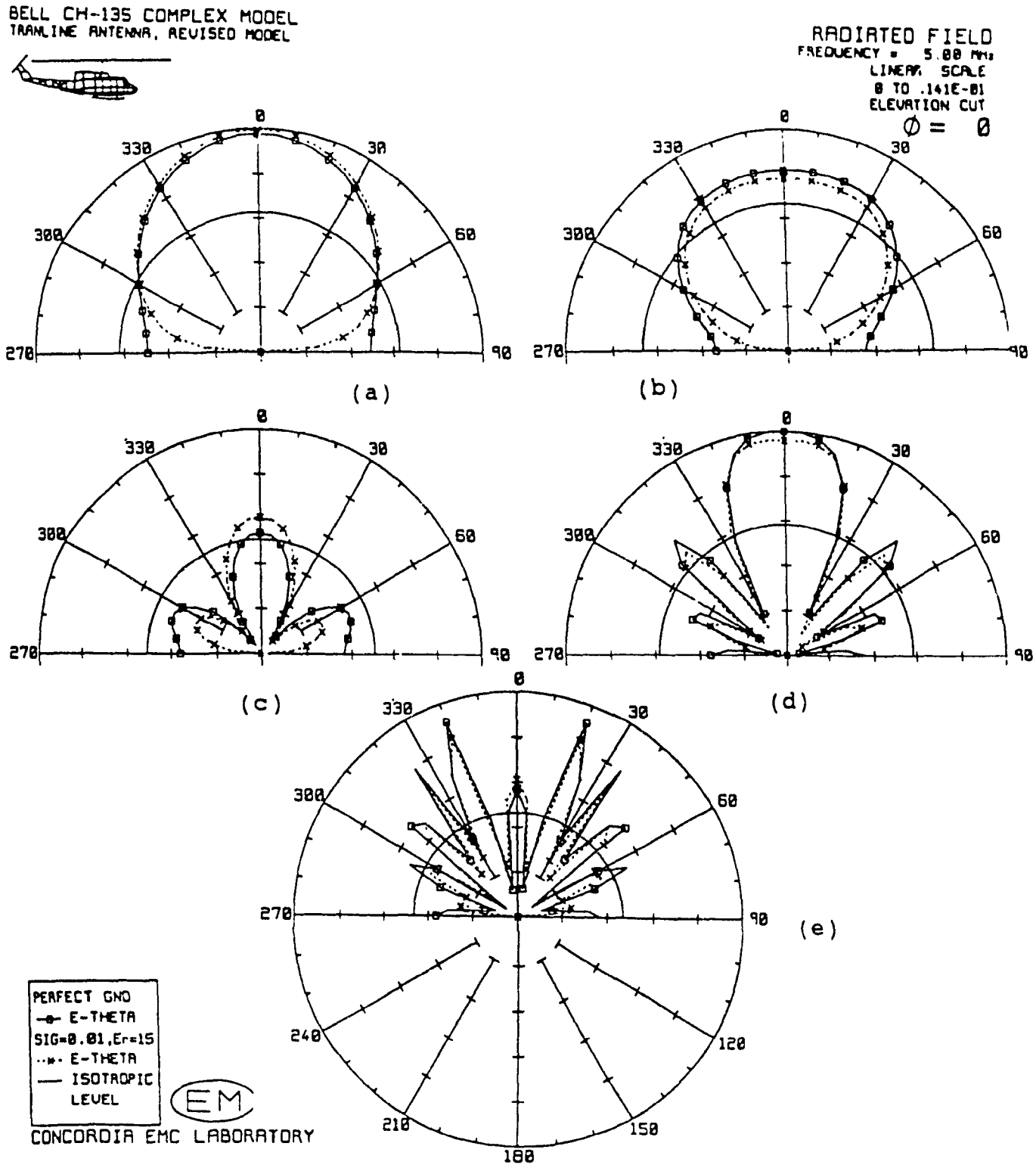

Figure 4-13 E_θ comparison at 5 MHz between perfect ground (solid line) and lossy ground (σ=0.01 mho/m, ε_r=15) when flying at (a) H=1m, (b) H=15m, (c) H=30m, (d) H=100m, (e) H=300m above the ground.

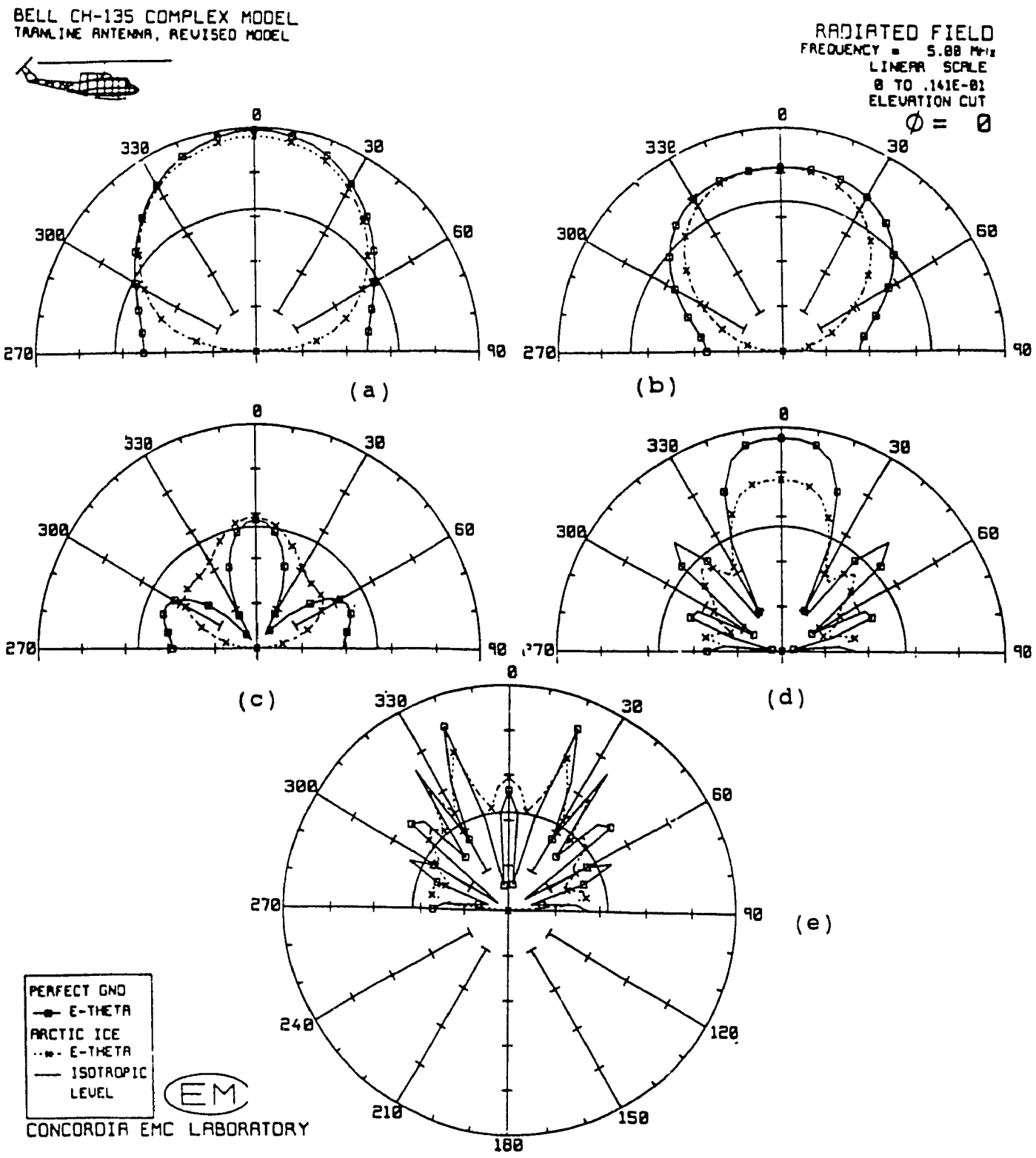

Figure 4-14 E_θ comparison at 5 MHz between perfect ground (solid line) and arctic ice when flying at (a) H=1m, (b) H=15m, (c) H=30m, (d) H=100m, (e) H=300m above the ground.

as they do in the case of perfect ground. From these figures it is obvious that the main effect of variation in conductivity of the earth on the vertical radiation patterns occurs at low angles where the space wave is much reduced from its value over a perfectly conducting ground. This is related to the phase of the reflection factor R_v, which changes rapidly for angles of incidence near Brewster angle. Above this angle the phase of R_v is nearly zero, whereas below this angle near grazing incidence the phase of R_v approaches -180 degrees[39]. When considering these figures, an important point to remember is that the relative shape of the patterns shown is the important thing; their relative size has less significance [56,39]. This is due to the fact that all the patterns shown in Figures 14-11 to 14-14 have been plotted for equal currents. A small radiated field, as for example in the case of arctic ice, indicates small power radiated for a given current and therefore, a low radiation resistance. For a given power radiated the currents would be larger for this case (arctic ice) and hence the resultant field would be larger[39]. For the sake of completeness the effects of variation in height and conductivity on the horizontal component of the electric field are illustrated in figures 4-15, 4-16 and 4-17. As noticed from these figures, the effects of conductivity are much less marked then vertical

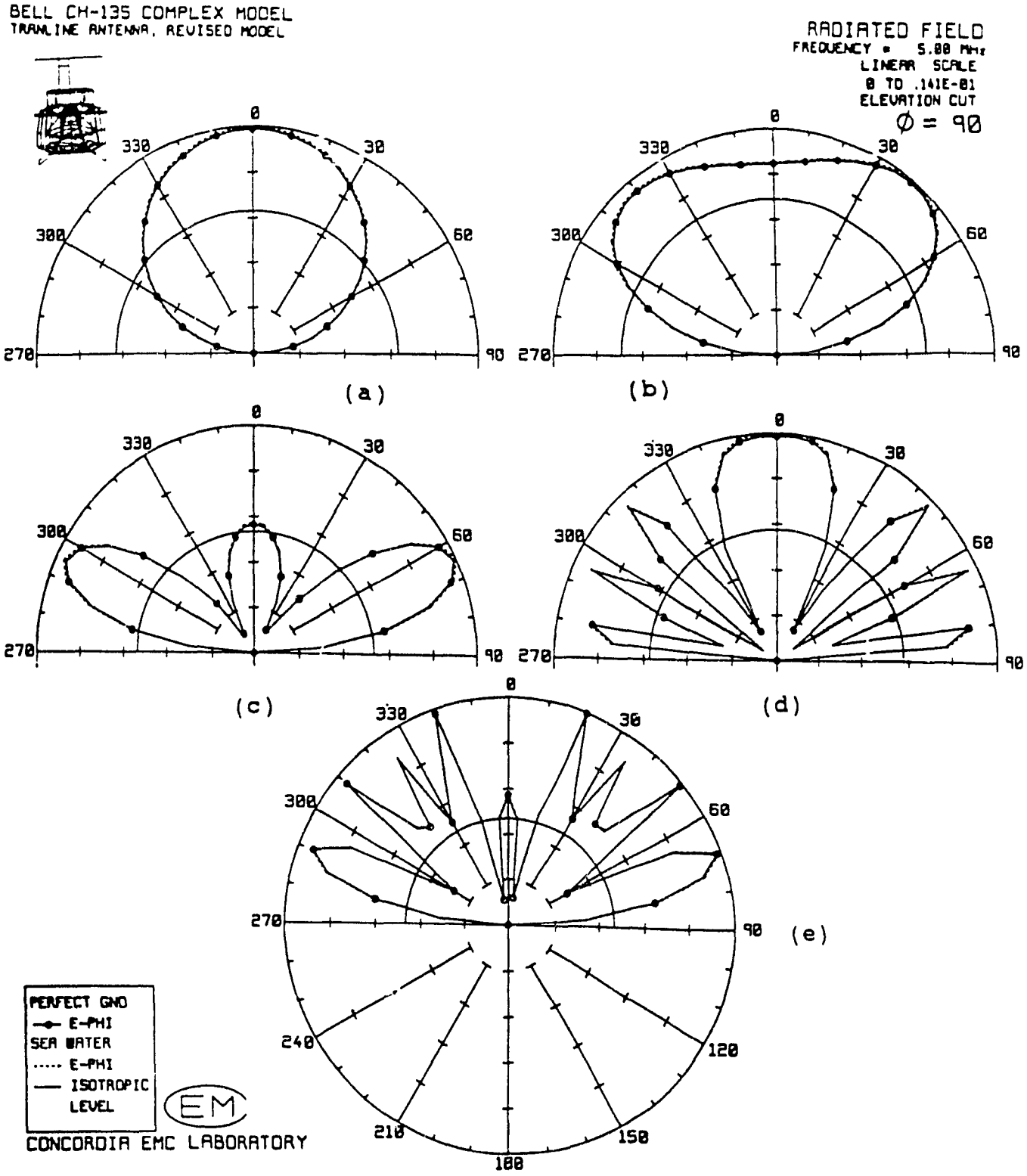

Figure 4-15 E_ϕ comparison at 5 MHz between perfect ground (solid line) and sea water when flying at (a) H=1m, (b) H=15m, (c) H=30m, (d) H=100m, (e) H=300m above the ground.

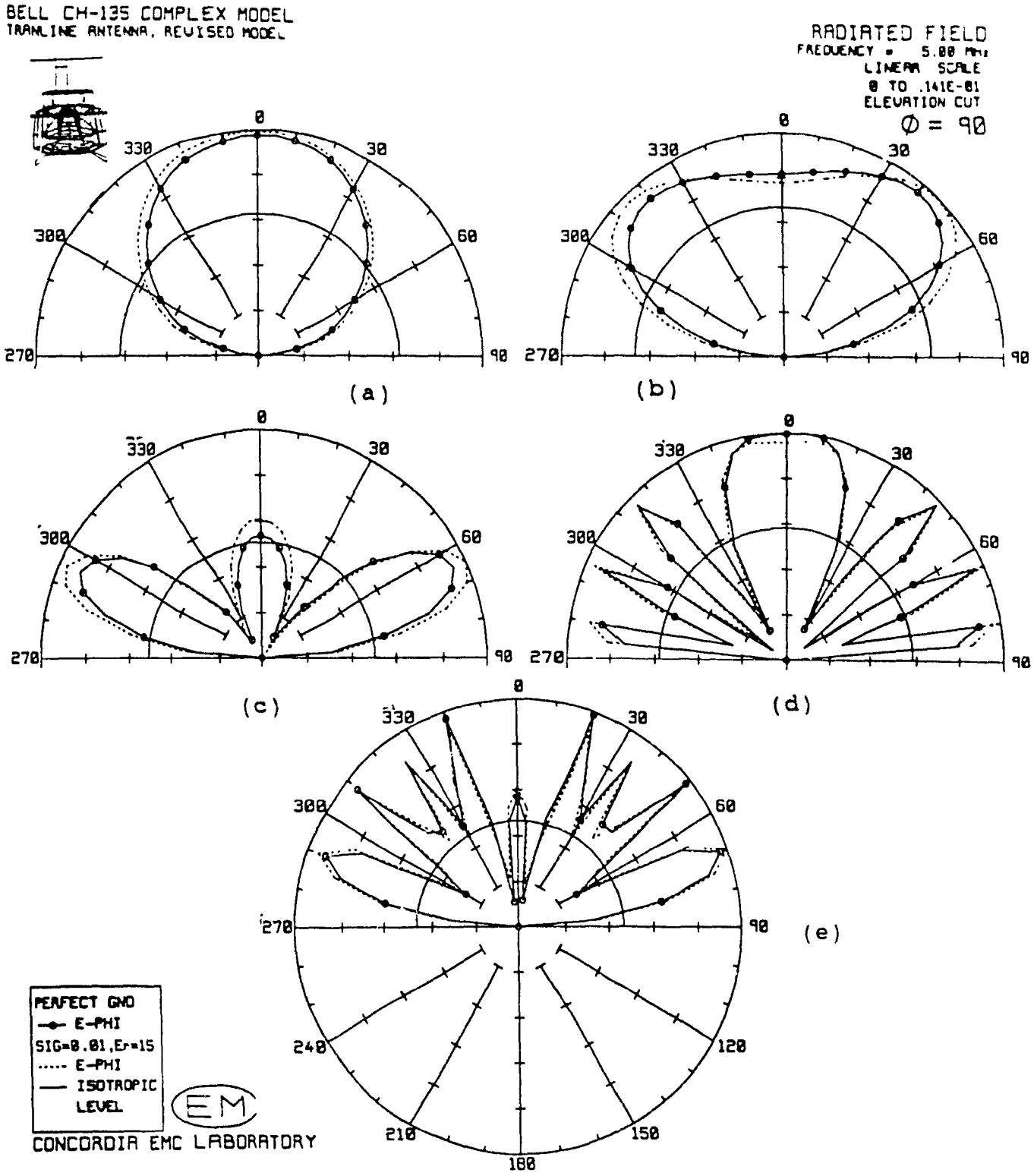

Figure 4-16 E_ϕ comparison at 5 MHz between perfect ground (solid line) and lossy ground (σ=0.01 mho/m, ε_r=15) when flying at (a) H=1m, (b) H=15m, (c) H=30m, (d) H=100m, (e) H=300m above the ground.

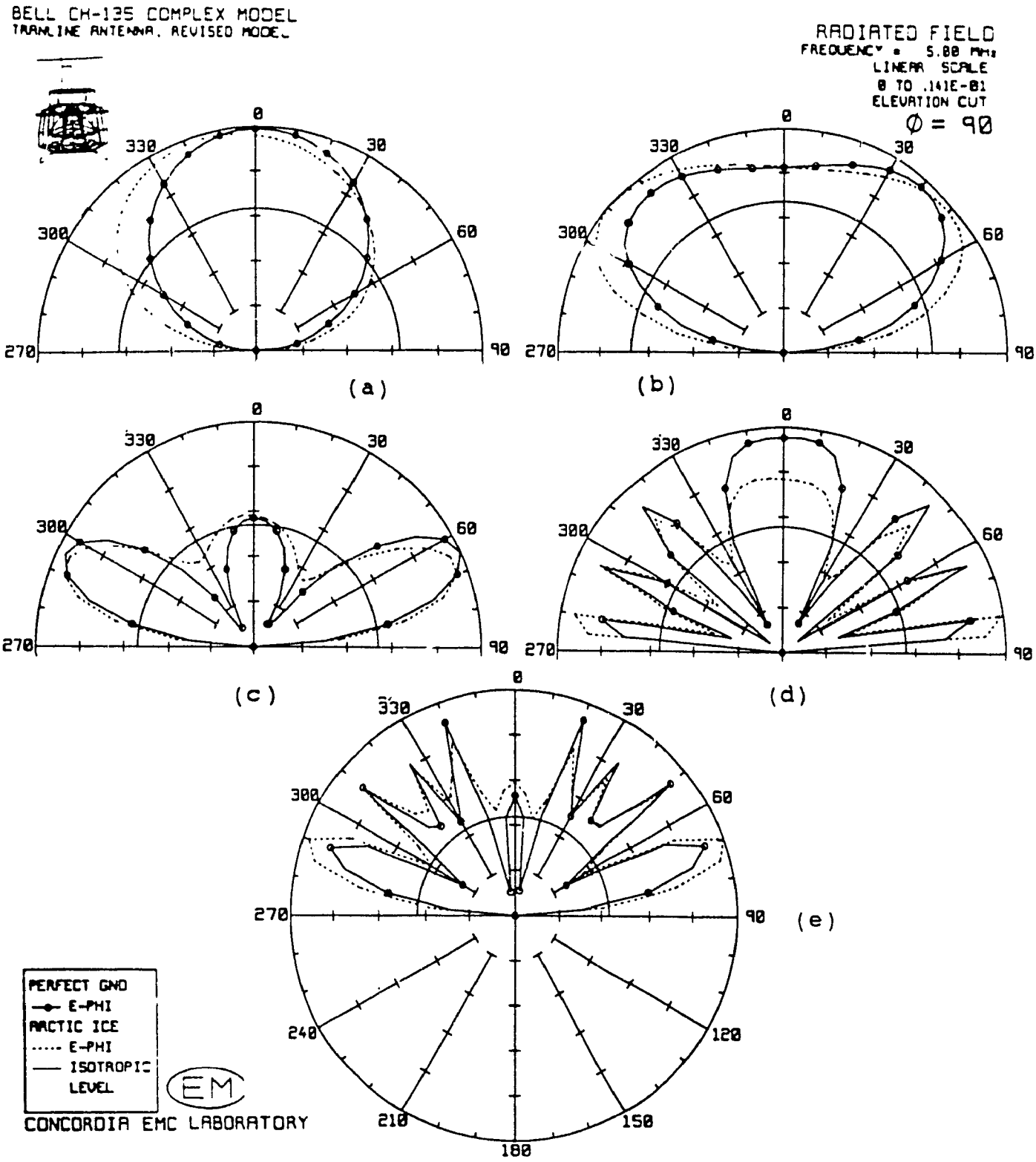

Figure 4-17 E_ϕ comparison at 5 MHz between perfect ground (solid line) and arctic ice when flying at (a) H=1m, (b) H=15m, (c) H=30m, (d) H=100m, (e) H=300m above the ground.

polarization, remembering once again that it is the relative shape of the patterns which is of prime importance and not their relative size.

4.4 The Input Impedance of Tranline Antenna

The interaction between an antenna and its associated circuits are greatly affected by the input impedance of the antenna. It is an important factor in consideration of power transfer, noise and stability of active circuit components. It is a limiting factor in establishing the useful bandwidth of the antenna[38]. Measurement of the input impedance is made at a single port and the antenna should be placed at a replica of its operating environment[57,58]. This is due to the fact that the input impedance of the radiating structures is modified by their environments[38].

The input impedance of tranline antenna on BELL CH-135 was measured on a full scale model. It is composed of resistive, or real, and reactive, or imaginary parts. Figure 4-18 illustrates the plots of input resistance and reactance versus frequency for measured and computed values. A definite shift may be observed between measured and computed results. As suggested by Larose[18], several factors may be identified that could have brought an

additional capacitive effect. Dielectric coating around the antenna, presence of lightning arresters near the antenna and the stand-off that shield the antenna from the surface of the fuselage may cause the capacitive effect. To account for these factors, the input impedance was shunted with a small capacitor of several picofarads. By trial and error, the best results were obtained with a 17.8 picofarad shunt capacitor. These results are illustrated in Figure 4-19.

The plots of input impedance of aircraft antennas contain important information about the electromagnetic behavior of an airframe. As shown in Figure 4-18, the computed input resistance has three "bumps" at 8, 10.8, and 27 MHz. The input reactance changes its nature from inductive to capacitive at 27 MHz. The last bump in the input resistance at 27 MHz may be explained by equating the antenna to a transmission line terminated in a short circuit. In this case, a reactance change from inductive to capacitive, accompanied by a sharp peak in resistance value, occurs at $(2n-1)\lambda/4$ intervals[59]. Tranline antenna is 2.9 meters long and is expected to have zero reactance around 26 MHz. The frequency difference may be due to inclusion of losses in the circuit[59]. The first two bumps in resistance value are in a range within which the dimensions of the airframe are comparable to λ. Hence they

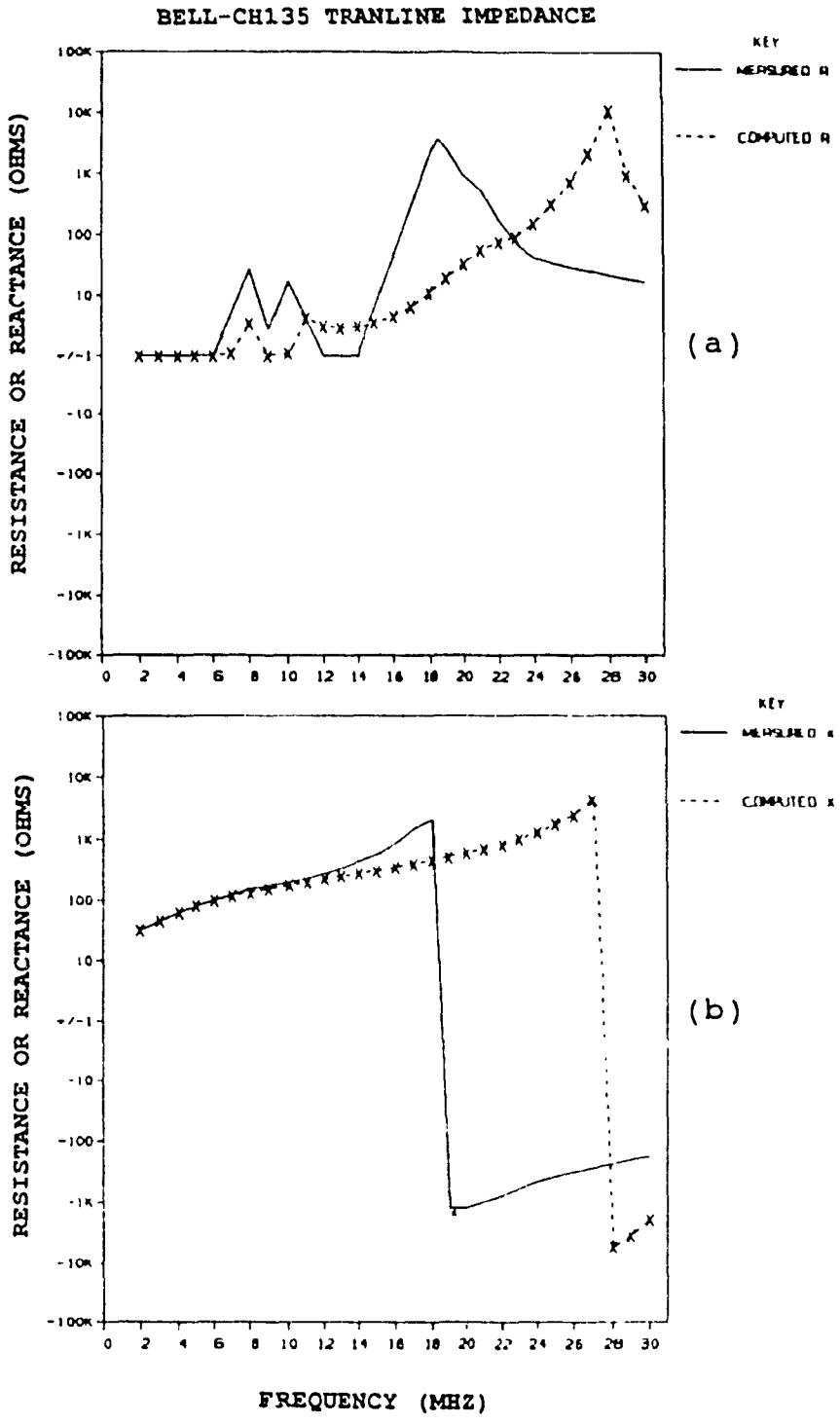

Figure 4-18 BELL CH-135 tranline antenna's (a) input resistance and (b) input reactance vs. frequency for measured and computed case.

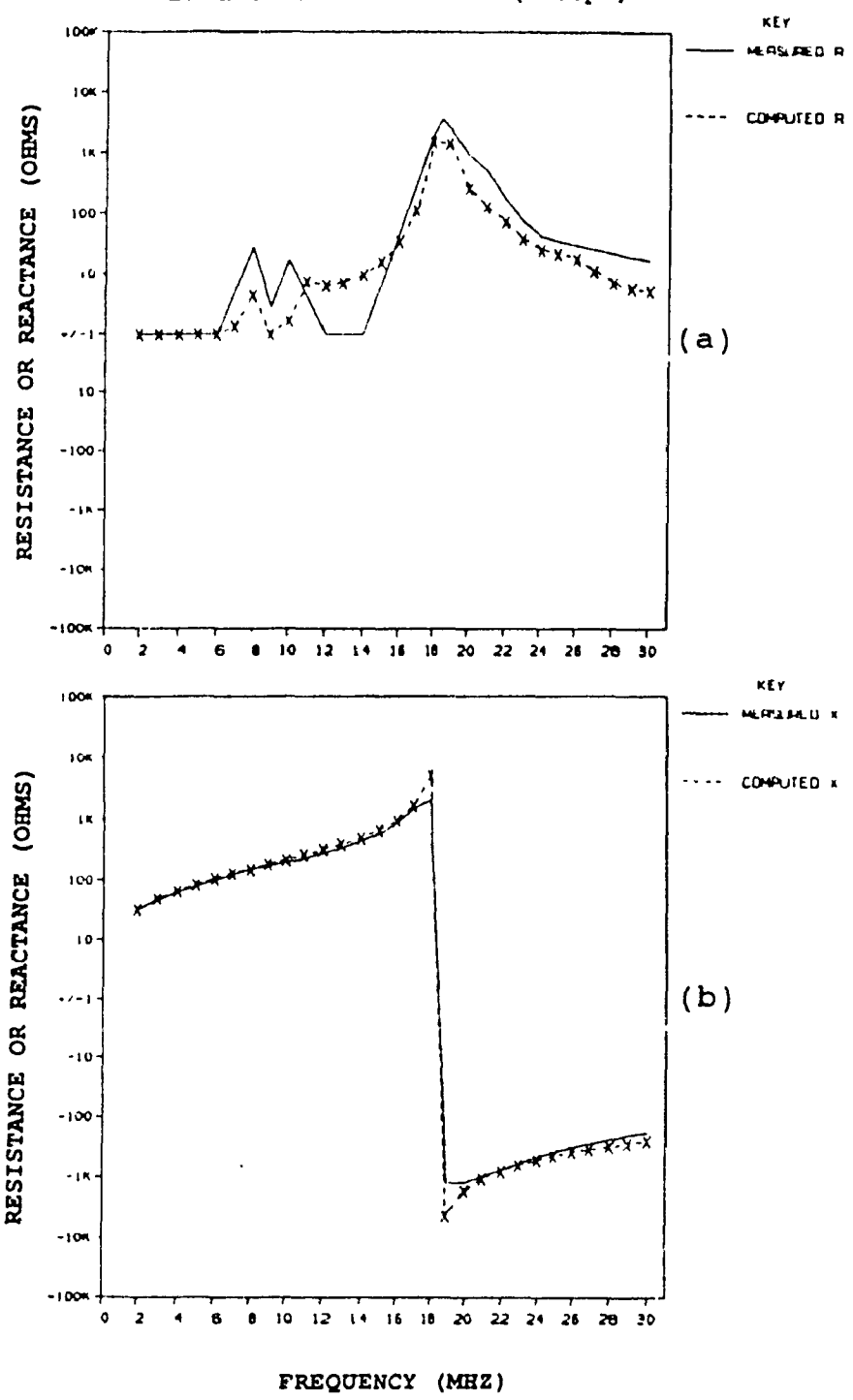

Figure 4-19 Measured and shunted computed (a) input resistance and (b) input reactance vs. frequency. shunt capacitor=17.8 pF.

could indicate what is known as longitudinal resonances.

4.4.1 Longitudinal Resonances of Tranline Antenna

In the analysis of the characteristics of airborne antennas, as mentioned by Granger[60], it has been observed that whenever the major dimensions of airframe are comparable with the wavelength, the airborne transmitting antenna excites different parasitic current paths on the airframe which affect both the radiation pattern and the input impedance of the antenna[60,61]. The impedance of an antenna will exhibit a series of peaks at the frequencies which give rise to the parasitic current paths. Each peak represents what is known as a longitudinal resonance[62]. The lowest order resonances occur at the frequencies where the lengths of the current paths, as measured along the most direct route on the surface of the airframe, are approximately equal to $\lambda/2$ [62]. For a fixed wing aircraft, the various modes of current flow is divided into two classes; symmetric and antisymmetric modes. Figure 4-20 illustrates these two modes for a fixed wing aircraft. It may be possible to define similar modes of current flow for a helicopter. Two bumps, at or around 8 and 10.8 MHz, are noticed in the computed resistance values as shown in Figures 4-18(a) and 4-19(a). Close examinations of the

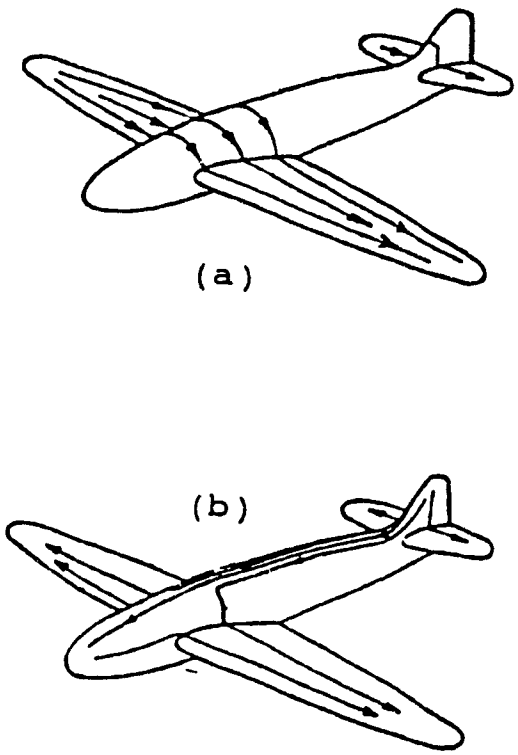

Figure 4-20 (a) Symmetric and (b) Anti-symmetric modes of current on a fixed wing airframe[62].

current distributions on the airframe at the above mentioned frequencies revealed that the bumps at 8 and 10.8 MHz may be the result of coupling to anti-symmetric and symmetric modes of the airframe, respectively. Figures 4-21 and 4-22 show the current paths along with the magnitude and phase of the current for 8 and 10.8 MHz, respectively. The program used to display magnitude and phase of the wires, called IDIS [18], displays the tag number of each wire at the bottom of its magnitude plots and top of its phase plots. From Figures 4-21(b) and 4-22(b) it is observed that the current distribution is

sinusoidal with a constant phase. It must be noticed that wire numbers 90 and 94 exhibit low current amplitude. This is due to the fact that, although parts of the current paths, they are situated perpendicular to other wires of the path and hence exhibit low current amplitude. The resonant current path at 8 MHz was measured to be 0.45λ and 0.48λ at 10.8 MHz. A possible justification for the difference between the measured lengths and 0.5λ may be found in the fact that by reducing the length of the half-wave dipole slightly, the antenna can be made to resonate[63]. Also as the wire thickness increases the dipole must be shortened more to obtain resonance[3,64].

The radiation pattern of a helicopter, as suggested by Cox and Vongas[65], exhibits certain characteristics in the azimuthal plane as the frequency approaches that of the longitudinal airframe resonance. At or around this frequency deep nulls in the nose and tail directions for the horizontal component should become apparent[65]. Figures 4-23 and 4-24 show the radiation patterns of 8 and 10.8 MHz, respectively. In figure 4-23 the measured and computed results are in good agreement and the nulls for the horizontal component are recognized in 4-23(a). At 10.8 MHz, due to the absence of measured results, only the computed results are shown in Figure 4-24. Again two deep nulls in the nose and tail directions for the horizontal

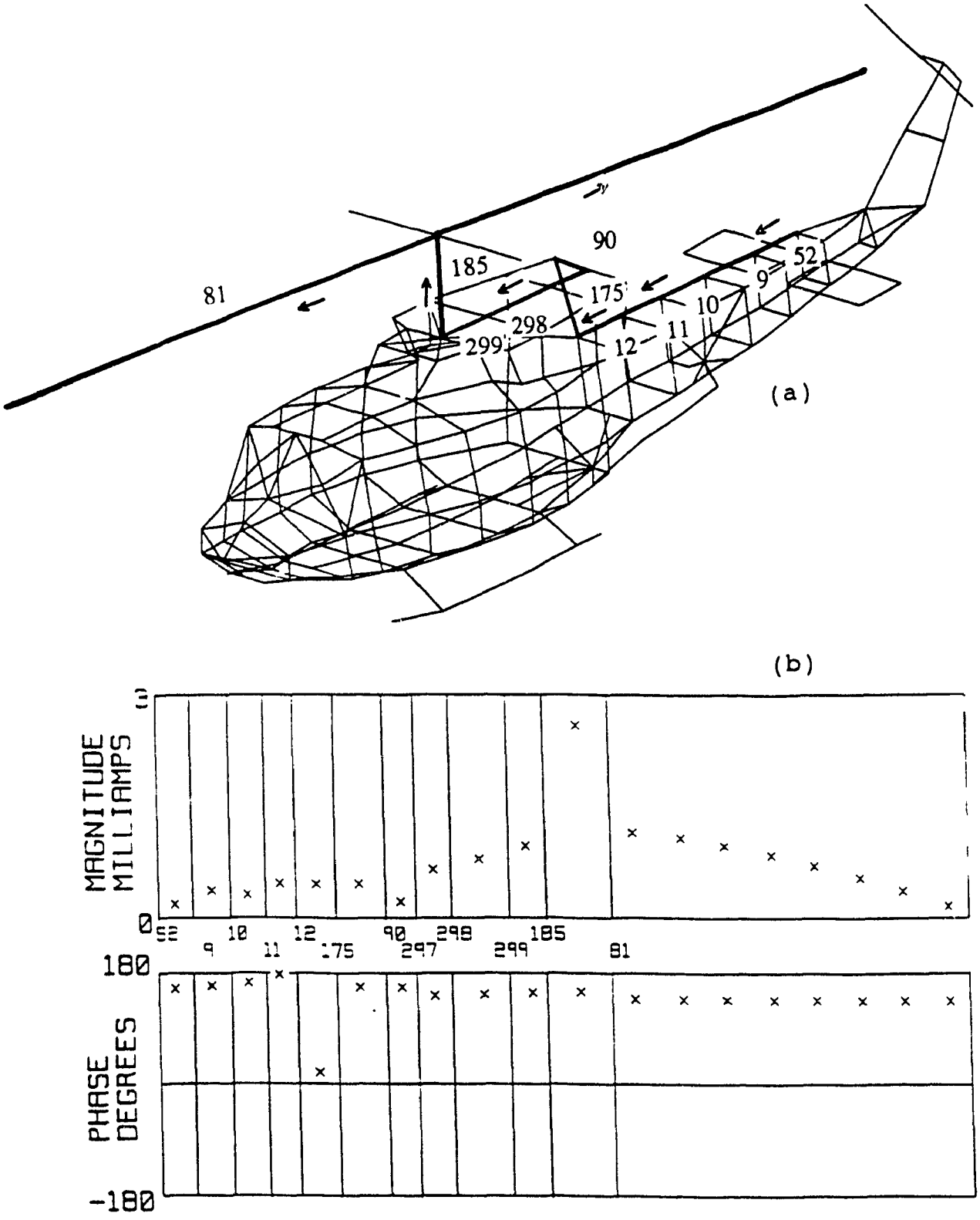

Figure 4-21 (a) Direction and (b) amplitude and phase of the resonant current at 8 MHz.

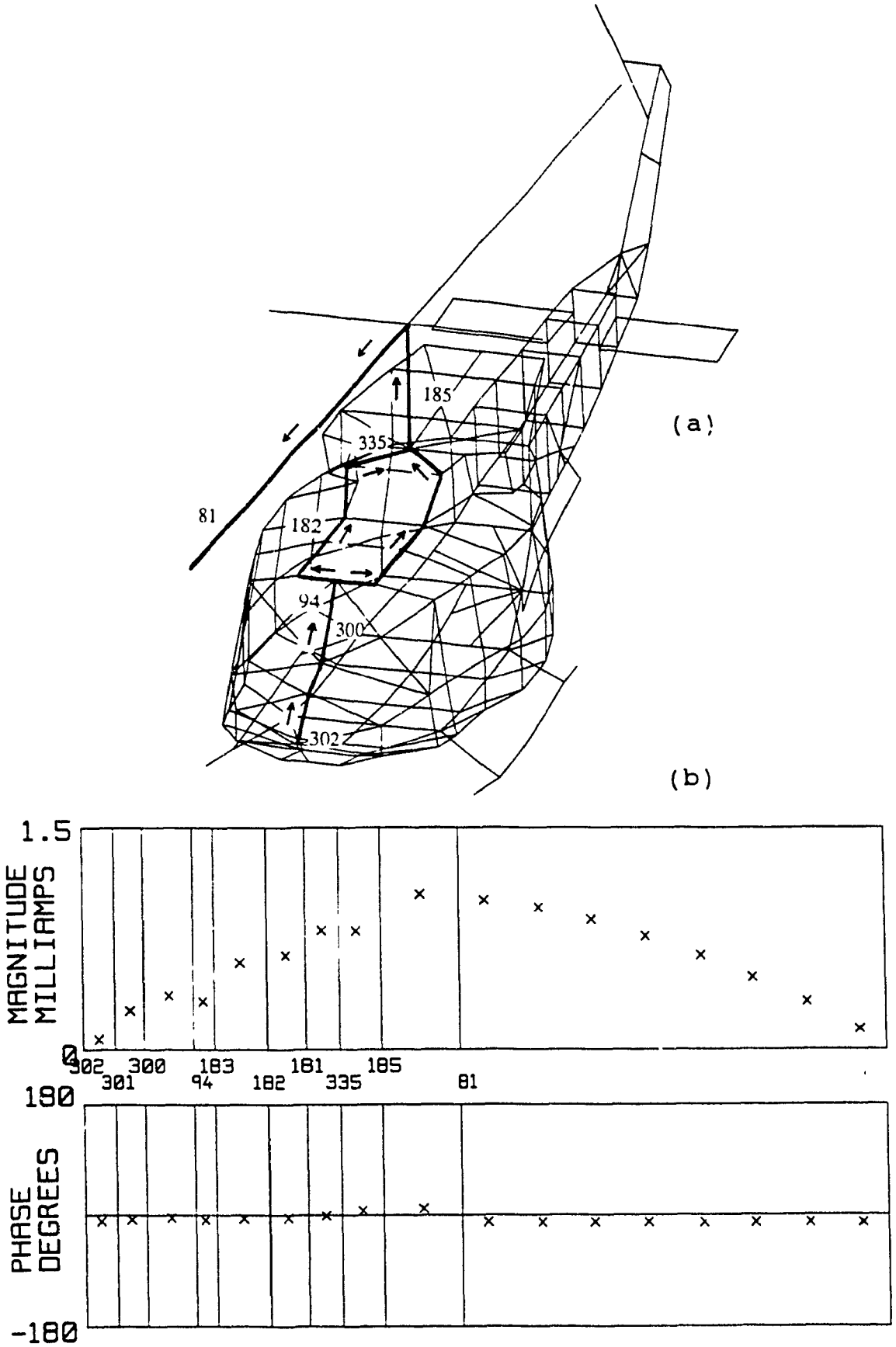

Figure 4-22 (a) Direction and (b) amplitude and phase of the resonant current at 10.8 MHz.

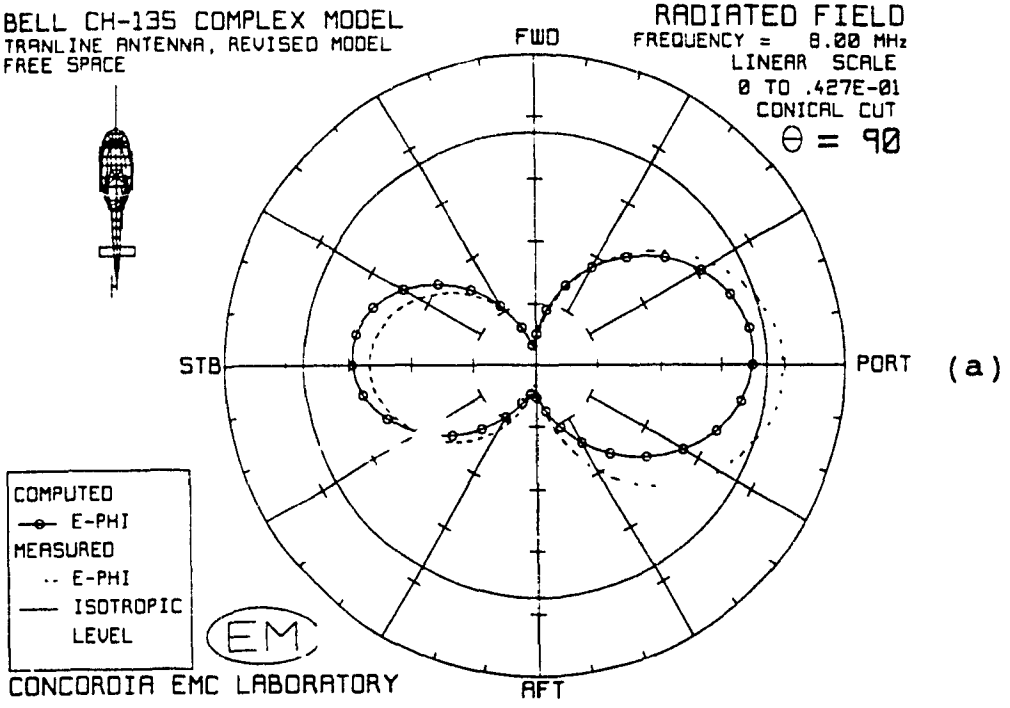

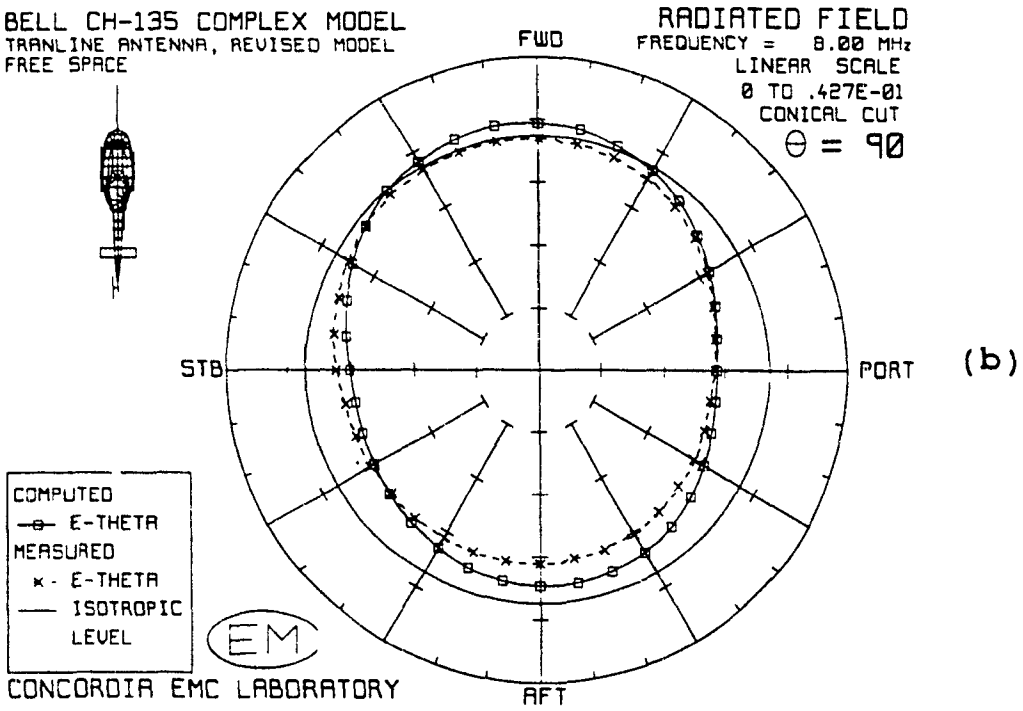

Figure 4-23 Comparison of computed and measured radiation patterns at 8 MHz in the θ=90 degree plane. (a) E_ϕ and (b) E_θ.

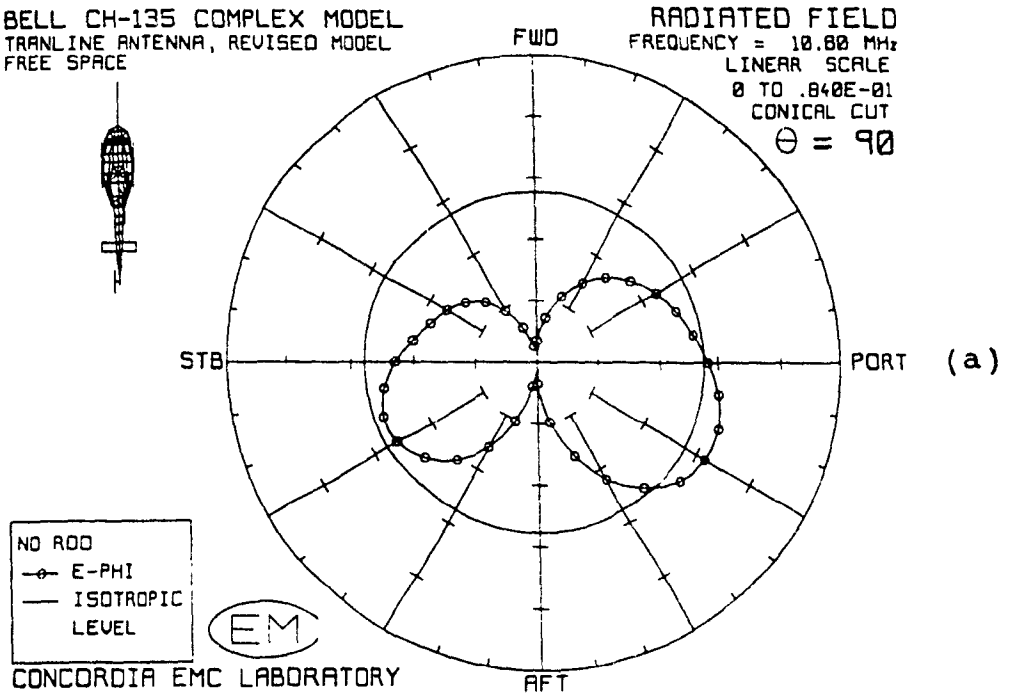

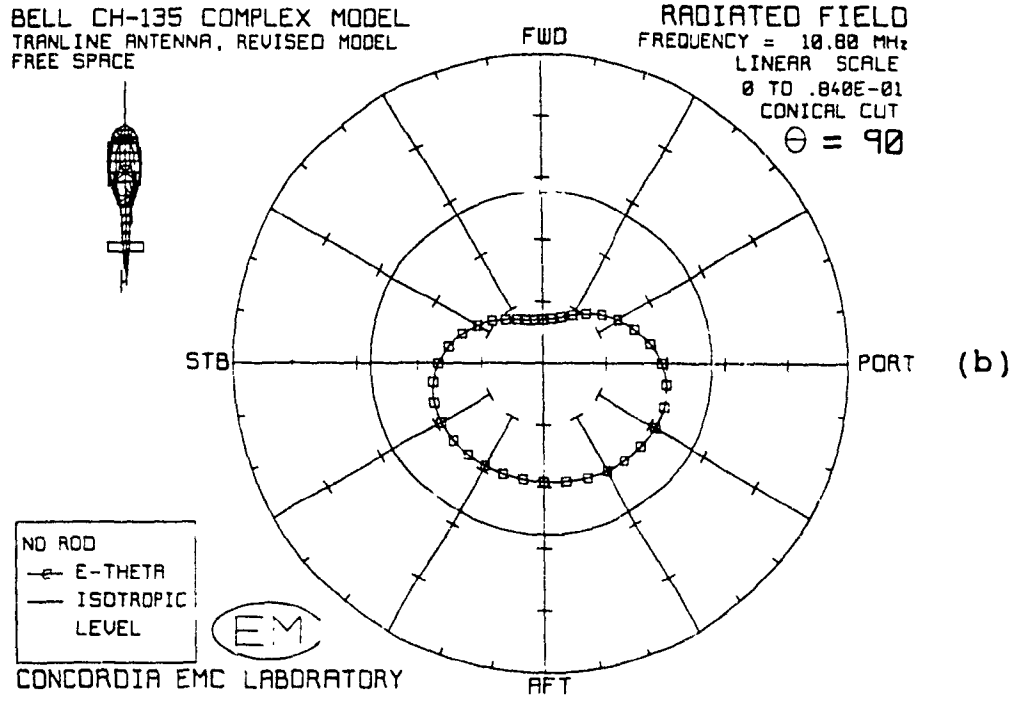

Figure 4-24 Computed radiation pattern at 10.8 MHz in θ=90 degree plane. (a) E_ϕ and (b) E_θ.

component are noticed.

4.5 The Effect of Rotor Modulation on Tranline Antenna

Unlike fixed wing aircraft, the rotor of a helicopter is a major component of the airframe which is constantly moving and is comparable with the wavelength at HF frequencies. It is believed that the performance of a helicopter antenna may be influenced, at certain frequencies, by the position of its rotor[66,67]. Wong and Muilwyk[66], reported an amplitude variation of 6 dB at 8.5 MHz for the Sea-king helicopter at different extreme rotor positions. To investigate the effect of rotor modulation on the performance of tranline antenna installed on BELL CH-135 helicopter, another model was created in which the position of rotor blade was changed by 90 degrees. Figure 4-25 illustrates the two different models. In Figure 4-25(a), or model 1D, the rotor is parallel to the overall length of the helicopter. This is the model for which pattern measurements of tranline antenna were performed. Model 1E on the other hand, Figure 4-25(b), has the rotor positioned perpendicular to the overall length of the helicopter and all the other parameters are the same as in model 1D. There are no measured data for model 1E. By

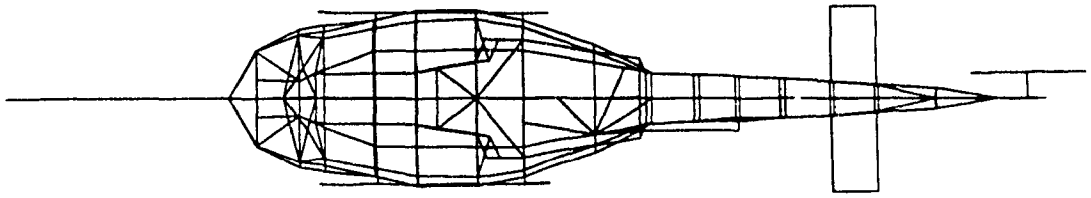

(a)

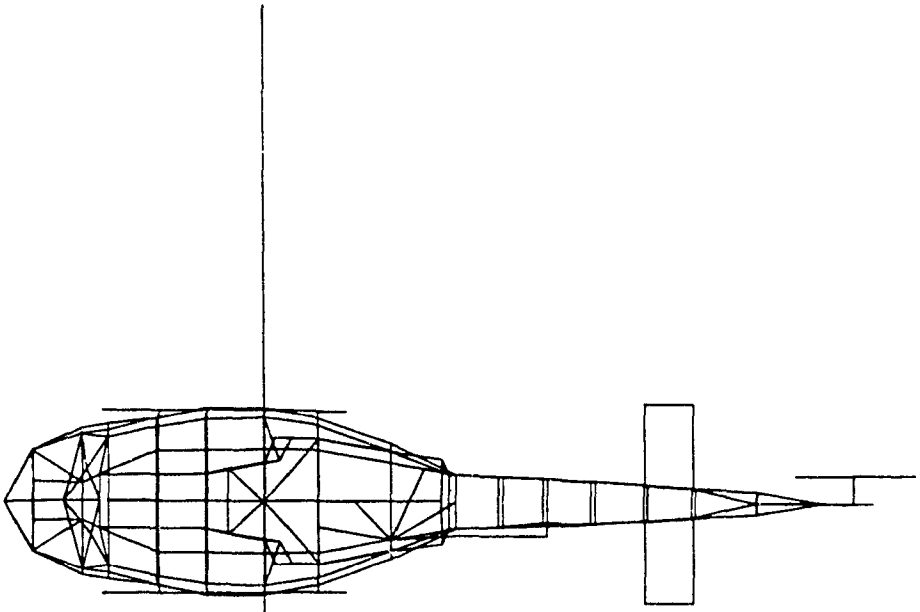

(b)

Figure 4-25 The rotor blade is (a) parallel (model 1D) or (b) perpendicular (model 1E) to the overall length of the helicopter.

comparing the two models it is noticed that a difference of approximately 3.45 meter in the overall electrical length of the helicopter results from rotor rotation. To examine the effects of the difference in electrical length, the performance parameters, Figure 4-26, and the input impedance, Figure 4-28, of the two models are compared against each other. A close examination of Figures 4-26 and 4-28 reveals that the most noticeable effect of rotor modulation happens at or around the frequencies at which longitudinal resonances were observed. At these frequencies the rotor blades are part of an electrical current path. The performance parameters show largest degradation of about 10% in radiation pattern efficiency, 15% in percent E_{θ} power and 20% in SUB-%E_{θ} power at 10 MHz. To further examine the effect of rotor modulation of the performance of communication system at 10 MHz, the horizontal and vertical components of radiation pattern at the above mentioned frequency, on the azimuthal plane, are illustrated in Figure 4-27. The vertical component, Figure 4-27(a), exhibits a maximum amplitude variation of approximately 5 dB in the FWD direction. The horizontal component however, Figure 4-27(b), exhibits both an amplitude variation and a definite pattern degradation. The rotor blade modulation could have serious effects on the communication system at frequencies where the radiation

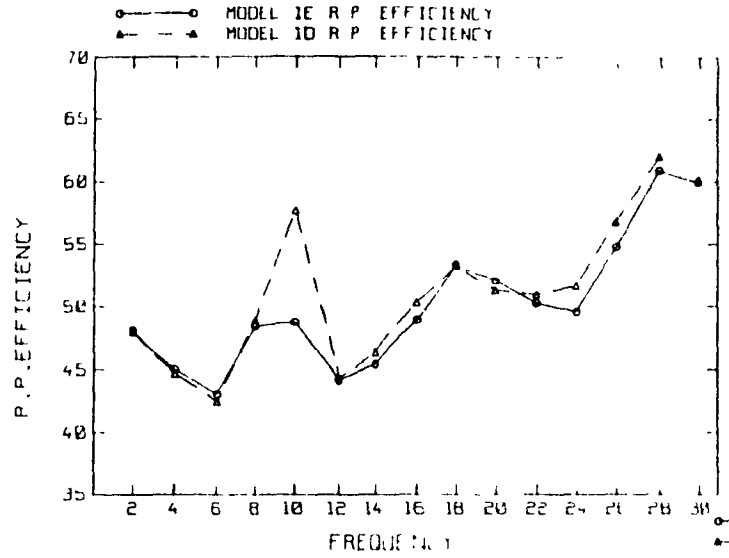

(a)

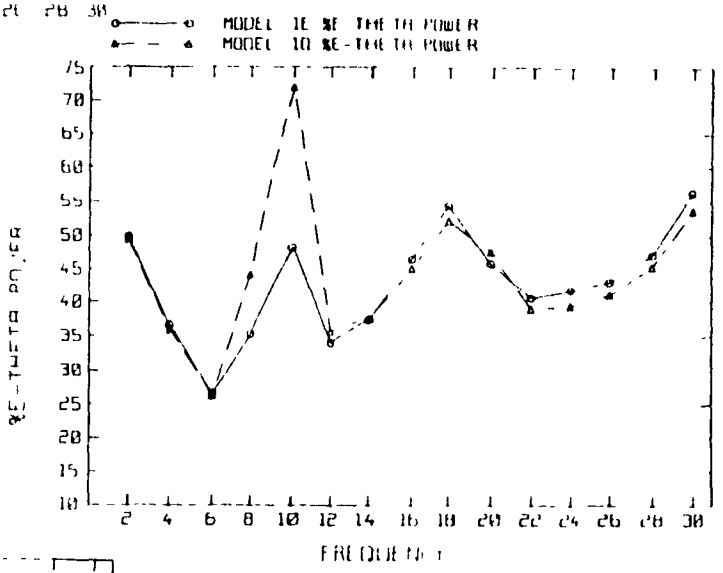

(b)

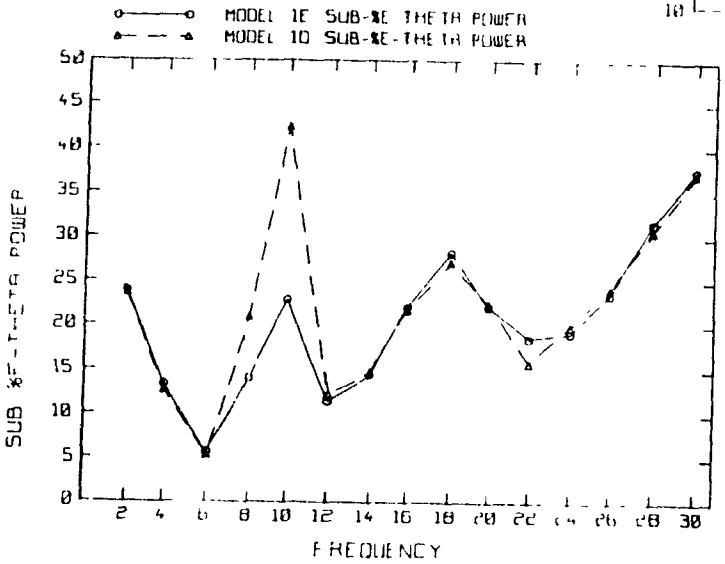

(c)

Figure 4-26 A comparison between (a) Radiation Pattern Efficiency, (b) % E_0 power and (c) Sub % E_0 power of models 1D and 1E.

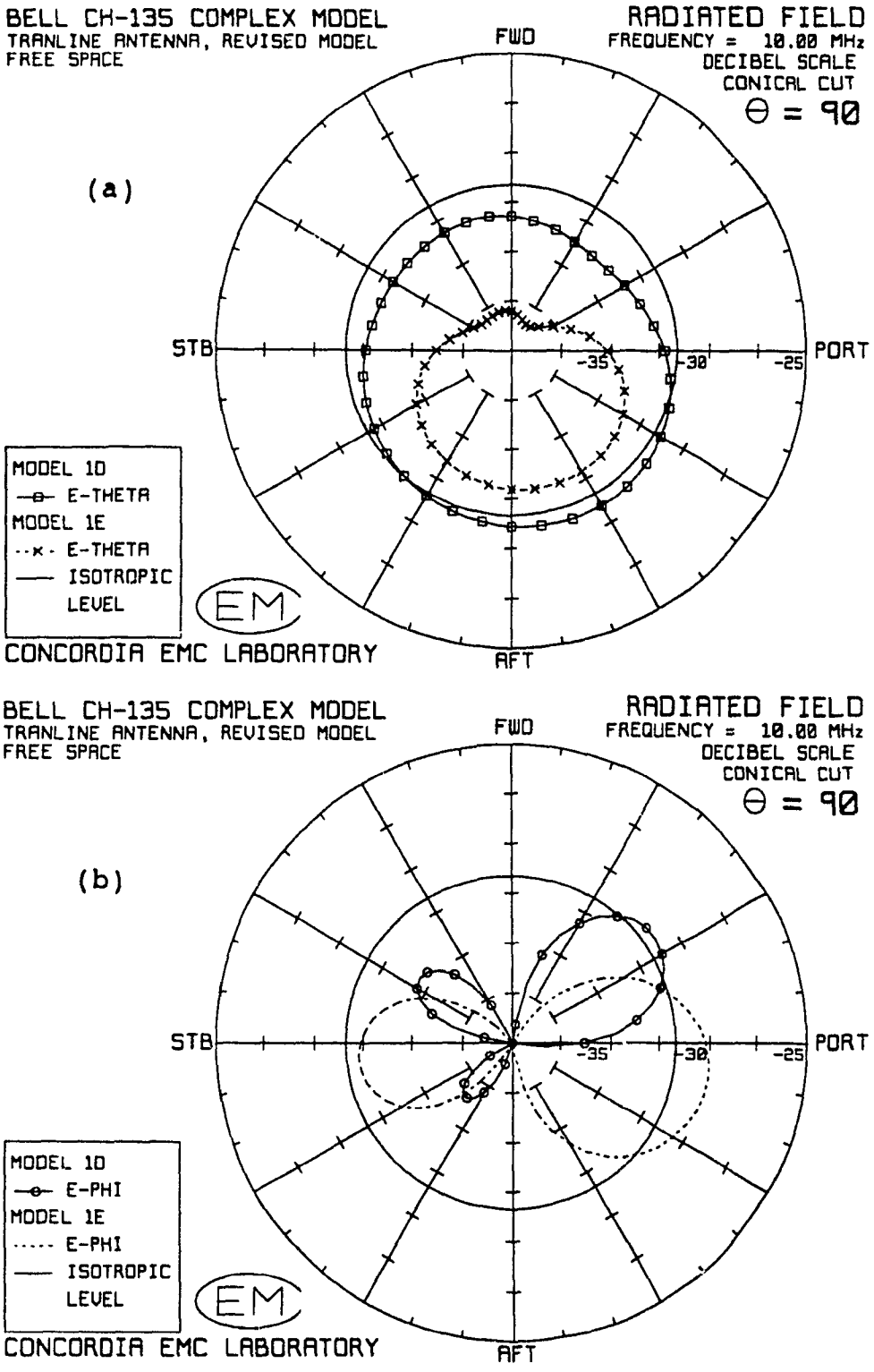

Figure 4-27 A comparison between the radiation patterns of models 1D and 1E at 10.0 MHz in θ=90 degree plane. (a) E_θ and (b) E_ϕ.

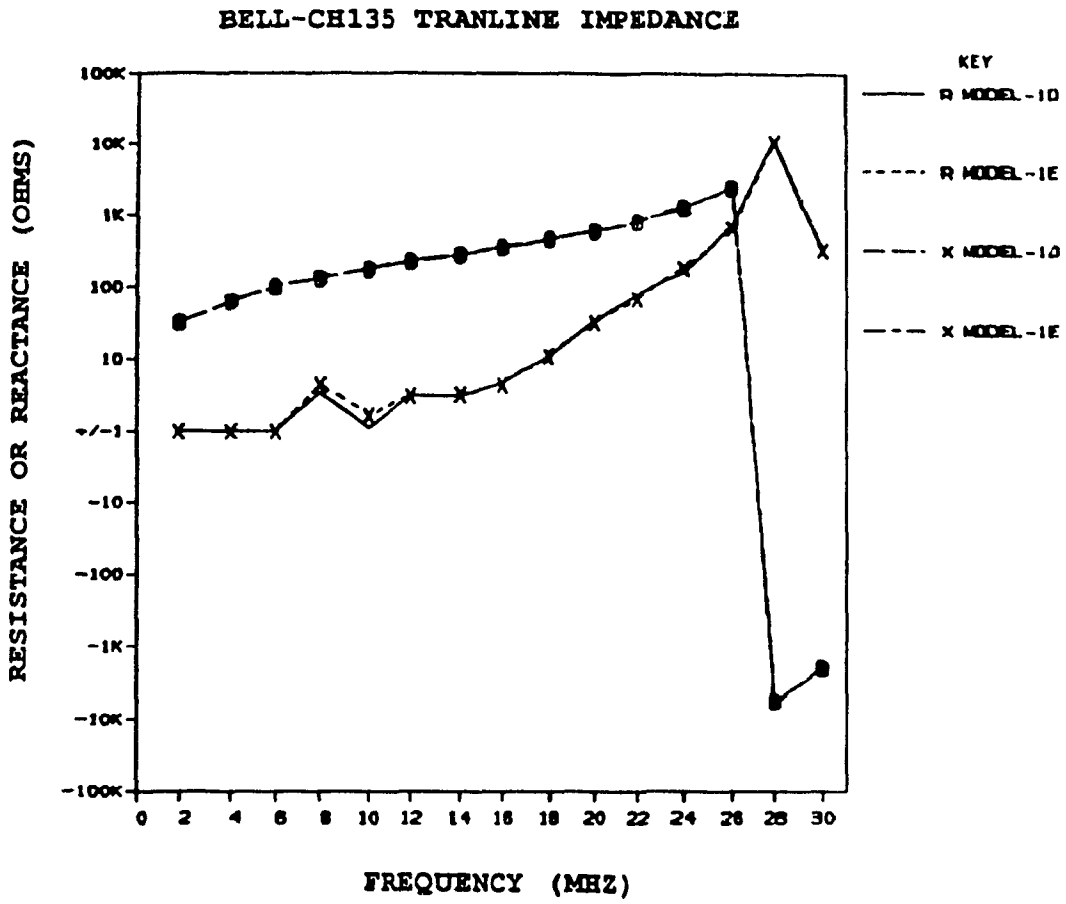

Figure 4-28 A comparison between input impedance of models 1D and 1E.

pattern changes radically[37].

CHAPTER 5

ZIG-ZAG INSTALLATION ON BELL CH-135

A second antenna which may be separately installed on BELL CH-135 helicopter is an open-ended wire antenna which runs along and around the tail section of the airframe in a zig-zag fashion, hence the name zig-zag antenna. The zig-zag formation, amongst other things, helps to increase the effective length of the antenna and maximize its interaction with the airframe. The location of the feed element and the radius of the wire is similar to tranline installation. It must be noted that these two antennas are not installed at the same time on the helicopter. Figure 5-1 illustrates a computer wire grid model with zig-zag installation shown in bold print. The model for the situation where the rotor blade is positioned parallel to the body, as in Figure 5-1, is called 2A.

Although radiation pattern measurements of the scale model with zig-zag installation were performed at NRC, they were not yet available to be used in this report. Hence all the mentioned characteristics regarding the zig-zag antenna are computational in nature.

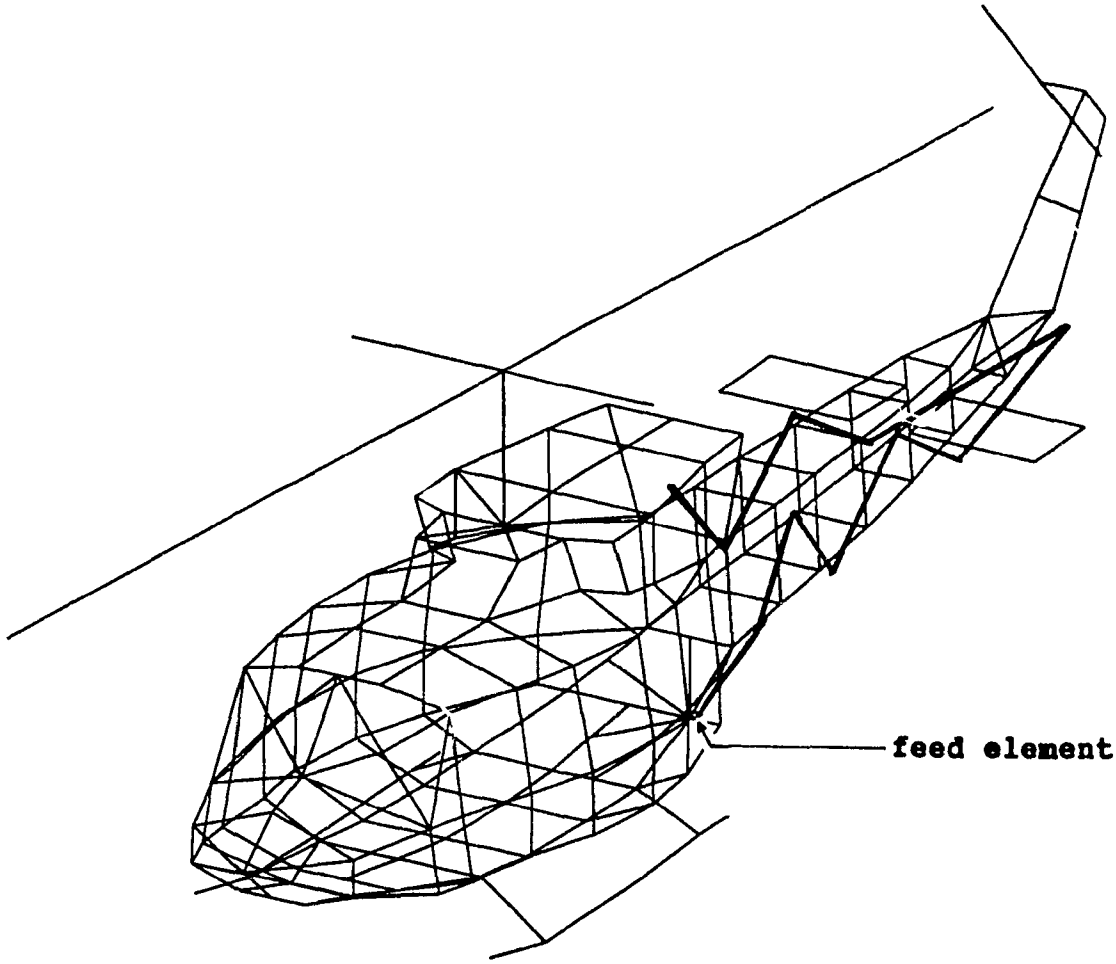

Figure 5-1 Computer model (model 2A) of BELL CH-135 with zig-zag antenna shown in bold print.

5.1 The Input Impedance of Zig-Zag Antenna

The input impedance of zig-zag antenna, Figure 5-2, is very similar to that of an open transmission line of finite length. It may be recalled that the input impedance of tranline antenna, Figure 4-18, was very similar to a short circuit transmission line of finite length. The input impedances of both open and short circuit transmission

lines exhibit resonance and antiresonance behaviours[68]. The antiresonance behaviour has many interesting features. Seshardi[68] has verified that the maximum value of R_{in} occurs at antiresonance. The input reactance, or X_{in},

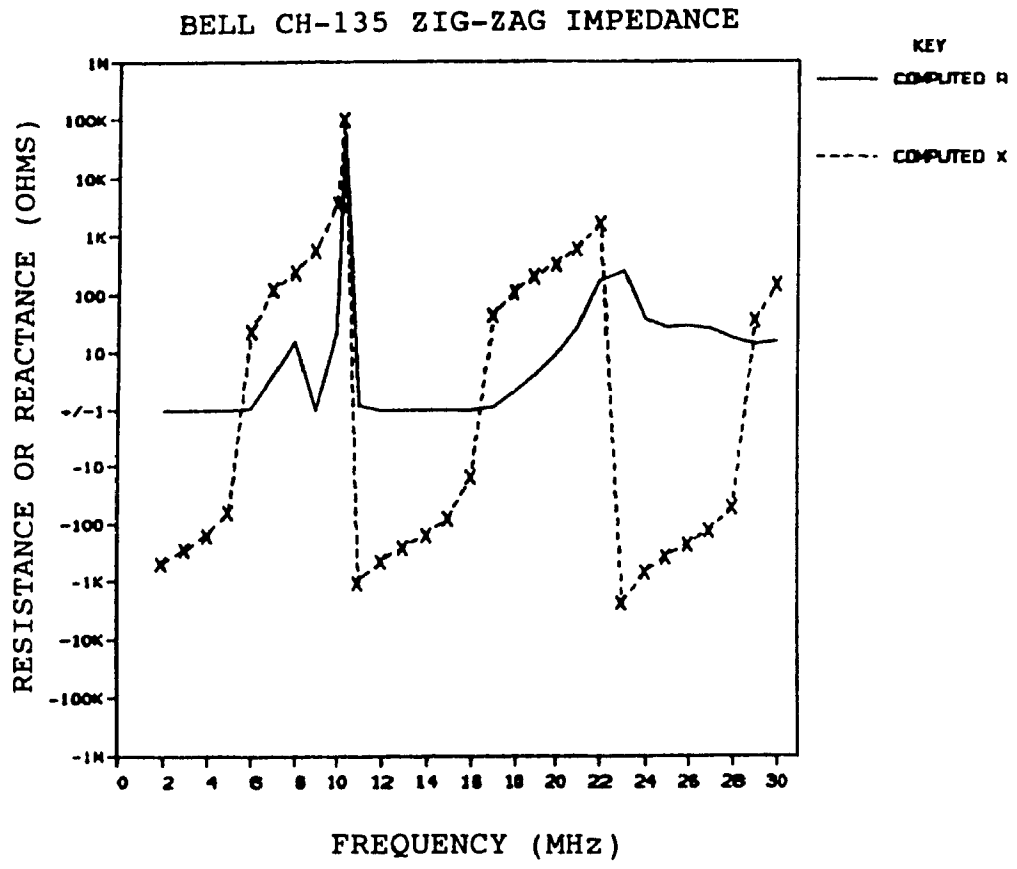

Figure 5-2 Input impedance of zig-zag antenna on BELL CH-135.

becomes infinite in the absence of losses. In the case of slight losses, the input impedance has a large finite value and a rapid variation passing through zero at antiresonance. When losses are included, antiresonance

takes place when the length of the line is in the close neighbourhood of $n\lambda/2$ or $(2n-1)\lambda/4$ for an open or short circuit transmission line, respectively[68]. Since zig-zag antenna is an open-ended wire antenna of length 14.02 meter, it is expected to exhibit antiresonance behaviour at around 10.6 and 21.2 MHz. As shown in Figure 5-2, antiresonance occurs at 10.3 and 22 MHz. The difference in values of expected and computed cases may be due to inclusion of losses. A careful examination of Figure 5-2 also reveals bumps in the value of input resistance at 8 and perhaps 10 MHz. This may be the result of coupling to longitudinal modes of resonance on the airframe, which was discussed in the previous chapter.

5.2 The Effect of Rotor Rotation on Zig-Zag Antenna

To examine the effect of rotor modulation on the performance of zig-zag antenna, a second computer model was created, model 2B, in which the rotor blades were positioned perpendicular to the length of the fuselage as shown in Figure 5-3. All the other parameters were kept constant. As mentioned before, a difference of about 3.45 in the overall electrical length of the helicopter results from rotor modulation. To examine the effects of the

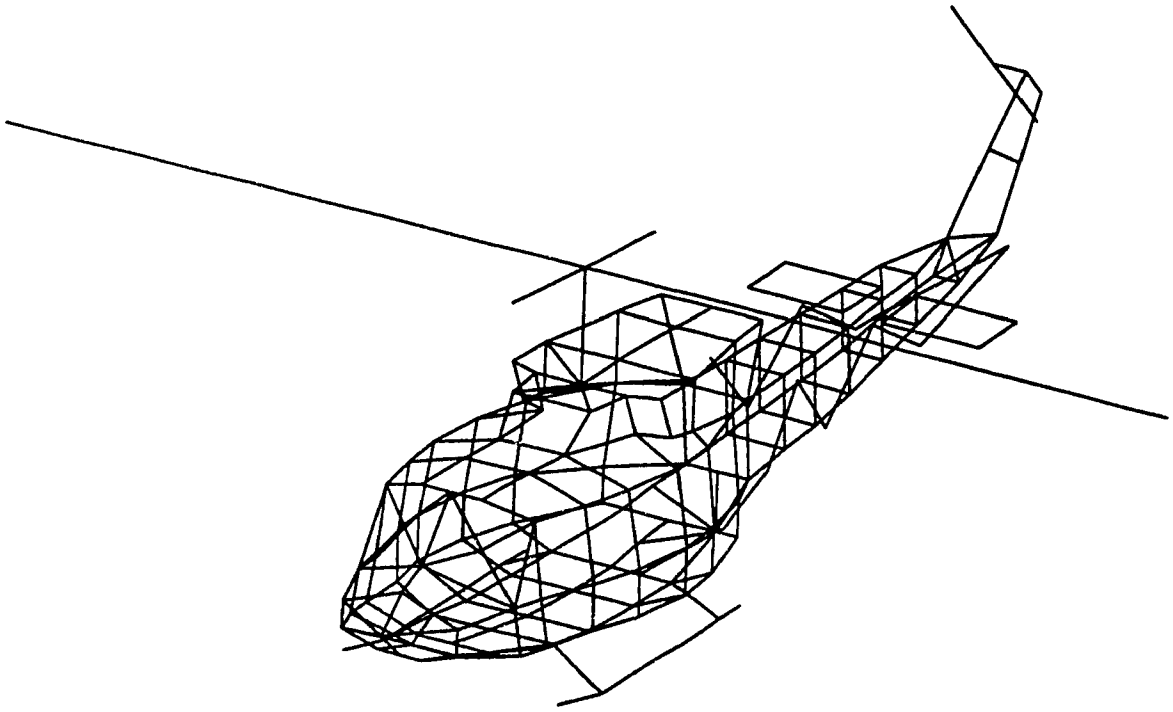

Figure 5-3 Rotor blade perpendicular to the overall length with zig-zag installation (model 2b).

difference in length, the performance parameters of the two models with zig-zag installation are compared against each other and shown in Figure 5-4. The largest differences in the values of performance parameters occur in the range of 8 to 10 MHz, where the probable occurrence of longitudinal resonance was indicated by the plot of input impedance shown in Figure 5-2. A maximum difference of about 7% in radiation pattern efficiency, 15% in percent E_0 power and 13% in SUB-% E_0 power between the models 2A and 2B at 10 MHz is shown in Figure 5-4. It must be noted however, that

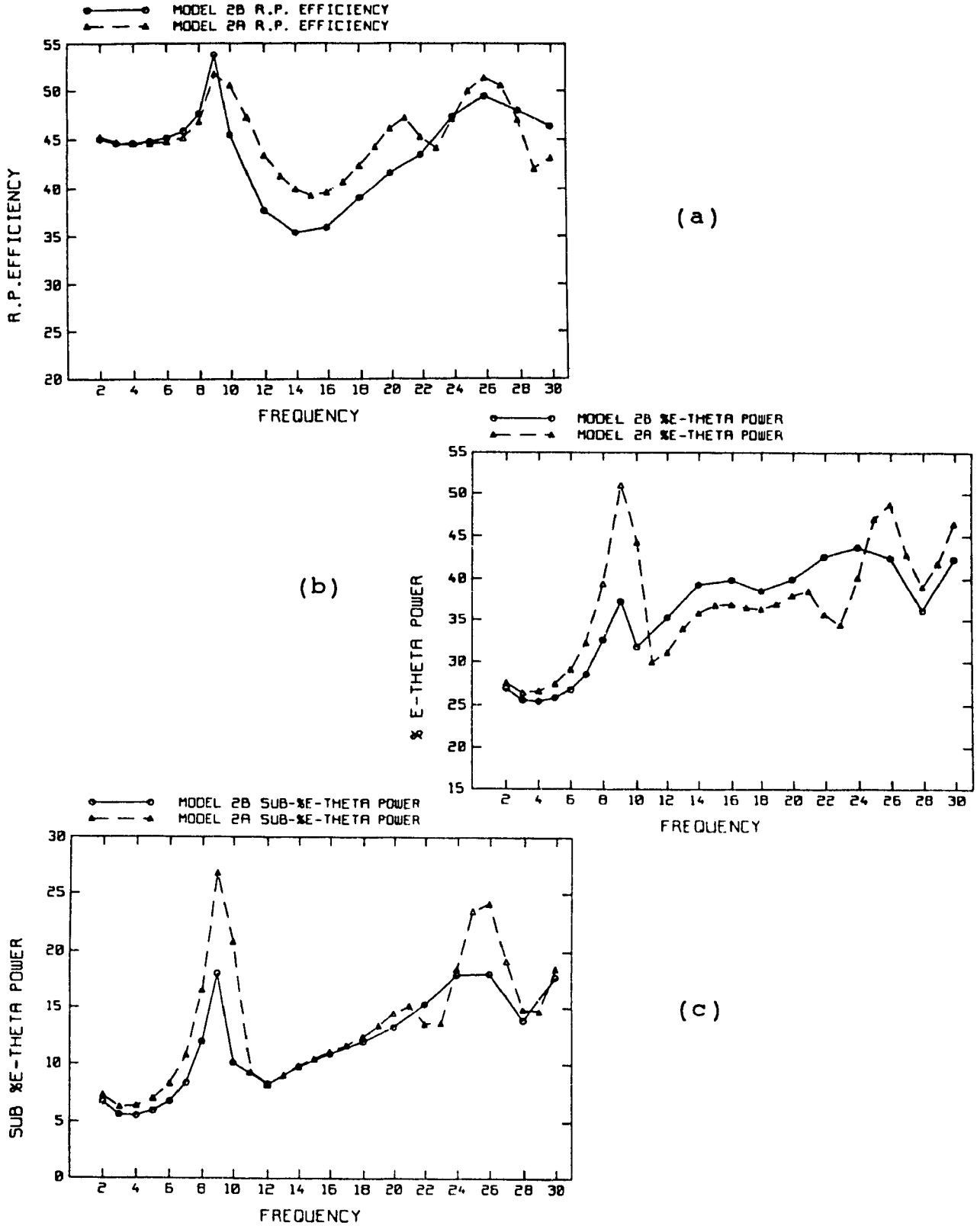

Figure 5-4 A comparison between (a) Radiation Pattern Efficiency, (b) % E_{θ} power and (c) Sub % E_{θ} power of models 2A and 2B.

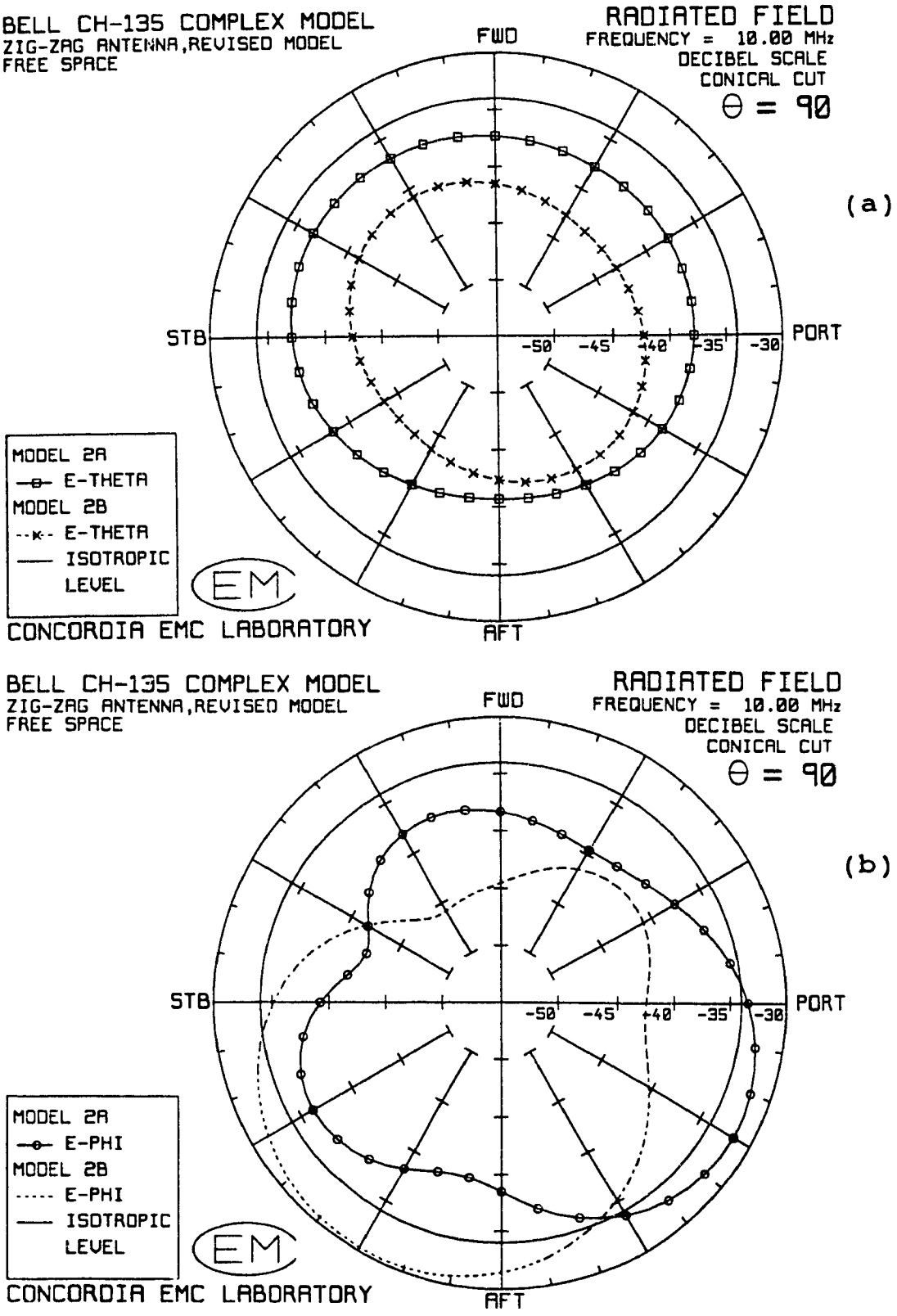

Figure 5-5 A comparison between the radiation patterns of models 2A and 2B at 10.0 MHz in θ=90 degree plane. (a) E_0 and (b) E_ϕ.

unlike tranline antenna, the differences between the performance parameters of zig-zag antenna are not confined to 8 to 10 MHz region, but rather exist all through the HF band with different variations. To further examine the effect of rotor modulation on the performance of communication system at 10 MHz, the horizontal and vertical components of the radiated field on the azimuthal plane are illustrated in Figure 5-5. An amplitude difference of approximately 5 dB is noticed in the vertical component, shown in Figure 5-5(a). The horizontal component, Figure 5-5(b), exhibits both an amplitude variation and a definite pattern degradation. A maximum amplitude variation of 8 dB is noticed in the PORT direction. Due to the pattern degradation, the communication system may also be effected at 10 MHz.

5.3 A Brief Comparison Between Zig-Zag and Tranline Antennas

Tranline and zig-zag antennas, Figures 4-1 and 5-1, are two different types of antennas which may be installed on BELL CH-135 helicopter[69]. The tranline, or HF loop antenna, generally takes the shape of a conducting tube several meters long supported at a height above the fuselage. The antenna is driven by an excitation source

attached to the feed point at a pylon and is grounded to the airframe at the other end. Other pylons can provide switched short circuit paths to the airframe so forming a continuous return path for electric conduction current[65]. The Zig-zag antenna on the other hand, is an open-ended wire antenna with a zig-zag shape which shares the common characteristics of wire antennas. Performance parameters of both antennas provide a good basis for a general comparison between the two antennas. Figure 5-6 illustrates the performance parameters of tranline and zig-zag antennas. A close examination of Figure 5-6(a) reveals that , with the exception of frequencies around 6 MHz, the tranline antenna seems to perform more efficiently than the zig-zag antenna. Figures 5-6(b) and (c) show that, with the exception of frequencies around 6 and 25 MHz, the tranline antenna seems to be radiating more efficiently in the vertical polarization including the solid angle of $60^\circ < \theta < 120^\circ$.

Other possible advantages of tranline antenna over zig-zag antenna are mechanical and electrical in nature. As mentioned by Cox and Vongas[65], "the operational and siting considerations for a helicopter give the loop antenna (a magnetic dipole) some mechanical advantages over other types of antennas. The electrical advantage is that by shorting out portions of the antenna it can be made to

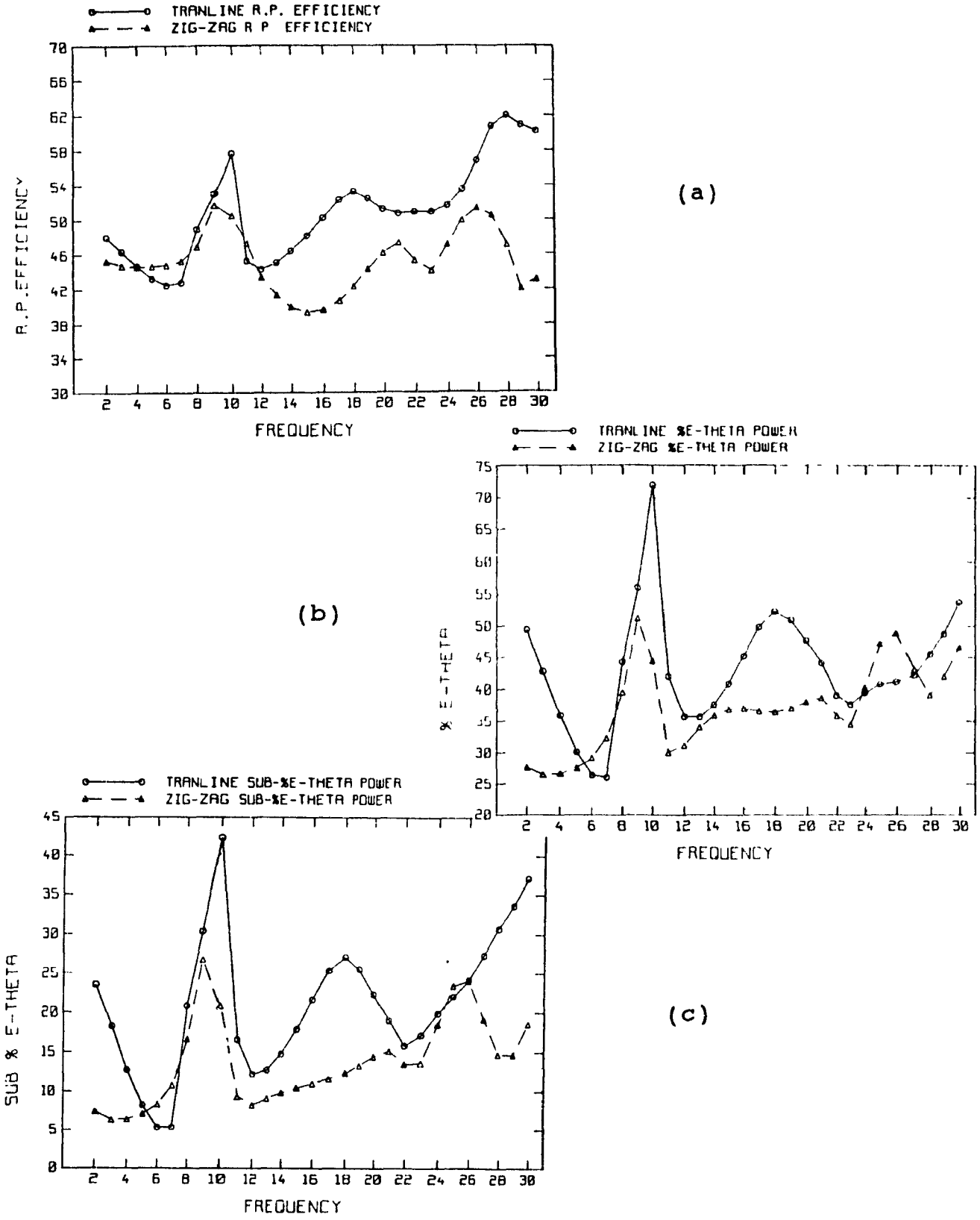

Figure 5-6 A comparison between (a) Radiation Pattern Efficiency, (b) % E_θ power and (c) Sub % E_θ power of tranline and zig-zag antennas.

exhibit an inductive reactance which does not vary greatly across the band. This simplifies antenna tuning unit (ATU) design. Although achieved at the cost of restricting the radiation resistance to comparatively low levels, this tactic enables tuning and matching to be achieved with low loss vacuum capacitors and tend to offset the concomitant efficiency penalty". An examination of Figure 4-18(b) reveals that the inductive reactance is indeed obtained across most of the HF band for tranline installation.

CHAPTER 6

CONCLUSION

In this thesis the development of a suitable numerical model for BELL CH-135 Twin/Huey is discussed. The process and known guidelines for model creation were discussed. The model was validated by comparison with scale-model measurements partly carried out by the author at the National Research Council in Ottawa. It has been shown that the validated model can effectively be used to compare the performances of Tranline and Zig-Zag antennas and obtain information regarding input impedance and rotor modulation effect on the performance of each antenna.

The computer model must be developed in accordance with certain rules and guidelines. These rules, which are known as "modelling guidelines", are either the consequences of assumptions made in deriving the integral equation and arriving at a numerical solution or the result of code limitations. Although some deviations from modelling guidelines are unavoidable at times, the attempt must be made to follow them to their fullest extent. Various modules are used in the EMC laboratory to inform

the designer of possible deviations from the guidelines so that correctional steps may be taken. The last step in model derivation is model validation. An internal validation may be done by "eyeballing" the results to detect an obvious physical inconsistency. In an external validation it is required to compare the computed results with the measured data. Comparisons of performance parameters, input impedances and radiation patterns are often carried out for external validation. It is however important to remember that validation, by its nature, is an open-ended task. The radiation pattern measurements of BELL CH-135 were performed using NRC facilities. The antenna was excited by a miniature battery-operated oscillator inserted into the model. The advantage of using oscillators was in eliminating the need for an external cable to excite the antenna. Since spurious RF signals may be induced on the high resistance cable, its removal would eliminate the distortion in patterns and reduce the error margin. Battery-operated oscillators however, tend to have a slight frequency drift over a period of time. This is particularly important when operating in the resonance region. A shift of 0.1 MHz could radically change the results in this region. This may explain the differences between the measured and computed radiation patterns at 10 MHz, as shown in appendices A and B. At all other

frequencies in the HF band the measured and computed results seem to be in good agreement with each other.

A more meaningful and general comparison between the measured and computed results is based on the performance parameters derived from the set of conical patterns and the power radiated by the antenna. These parameters are radiation pattern efficiency, percent E_0 and SUB-percent E_θ. R. P. Efficiency is the ratio of power radiated in the sector $60° < \theta < 120°$ to the total power radiated by the antenna. Percent E_0 is the ratio of radiated power in the vertical component to the total power radiated by the antenna. The third parameter, SUB-percent E_0, is the ratio of power radiated in the vertical polarization in the solid angle of $60° < \theta < 120°$ to the total power radiated. A comparison between measured and computed performance parameters of tranline installation on BELL CH-135 reveals very good agreement throughout the HF band. Furthermore it shows that the tranline antenna is a poor radiator in the vertical polarization in the region of 16 to 24 MHz.

Of particular interest was the ability to obtain elevation pattern information under varying height and conductivity in order to have means to analyze communication system performance under various propagation conditions. It was found that as the height above the ground increases, so does the number of lobes in the far

field radiation pattern. Furthermore, as the ground conductivity decreases, the nulls in the pattern begin to be "filled, that is, they are not as deep any more.

BELL CH-135 helicopter supports the separate installation of two different antennas, namely Tranline and Zig-Zag. Tranline is an HF shorted loop antenna in the shape of a conducting tube. It is connected to the fuselage at the feed and join points and maybe shorted to the airframe by means of pylons. Zig-Zag is an open-ended wire antenna which is stretched along and around the tail section of the helicopter in a zig-zag shape. It was shown that both antennas produce typical input impedance plots. The Tranline antenna was shown to have an input reactance which is inductive for a good portion of the HF band, and resembles a transmission line terminated in a short circuit. The input impedance of a Zig-Zag antenna is similar to that of a transmission line terminated in an open circuit. The antiresonance phenomenon occurs at $(2n-1)\lambda/4$ or $n\lambda/2$ intervals for a short or open circuit transmission line, respectively. The "bumps" in the curves of input resistance, around 8 and 10 MHz, are shown to be the result of coupling to longitudinal modes of resonances on the airframe of the helicopter.

Since, from an electromagnetic point of view, the rotor of a helicopter is a major component of the airframe,

its modulation is shown to affect the HF communication at certain frequencies. The rotor rotation creates a difference of approximately 3.45 meter in the overall electrical length of the helicopter. A close examination of the performance parameters of both antennas reveals that the performance of Tranline installation is affected by rotor modulation at 8 and 10 MHz, whereas the performance of Zig-Zag installation is affected all throughout the HF band. The analysis of current distribution and input impedance has produced insight into interactions with the fuselage which helo to understand pattern changes and rotor modulation effects.

Most of the information presented in this thesis regarding the computer model were obtained using frequency steps of 2 MHz. With the advancement of technology it is now possible to complete a NEC run in a few minutes. It is therefore recommended that the frequency steps be reduced to 5 KHz in the 7 to 11 MHz region of the HF band, and 10 KHz in all other regions. This is due to the fact that the electromagnetic response in the resonance region is drastically affected by a small change in frequency. If the opportunity of performing measurements on the scale model of the helicopter presents itself again, it is highly recommended that they be carried out in steps of 1 or 0.5 MHz. The results could then be used to fine tune the

computer model in order to arrive at a more precise numerical result. Small frequency steps, both in measurements and numerical computation, help to reveal intricate details of coupling between airborne antenna and the airframe in the HF band.

Appendix A

Tranline antenna (model 1D with the rod installed) three dimensional radiation patterns computed (top), and measured (bottom) in the HF band.

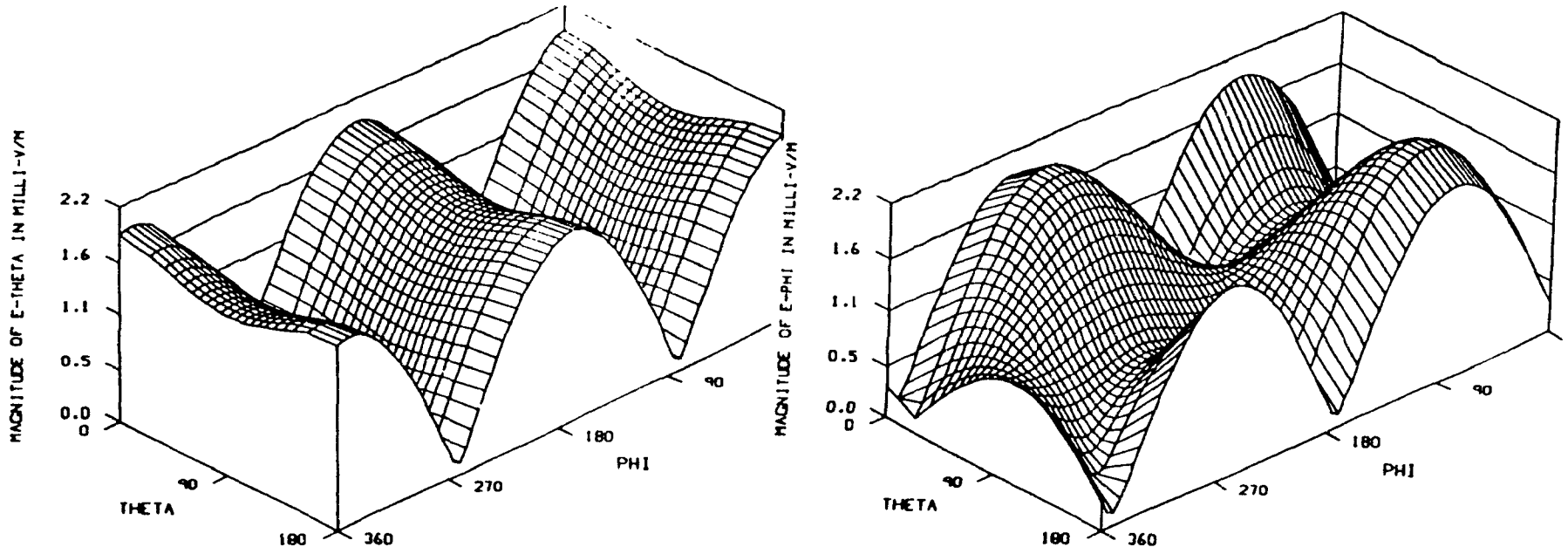

FREQUENCY = 2 MHz

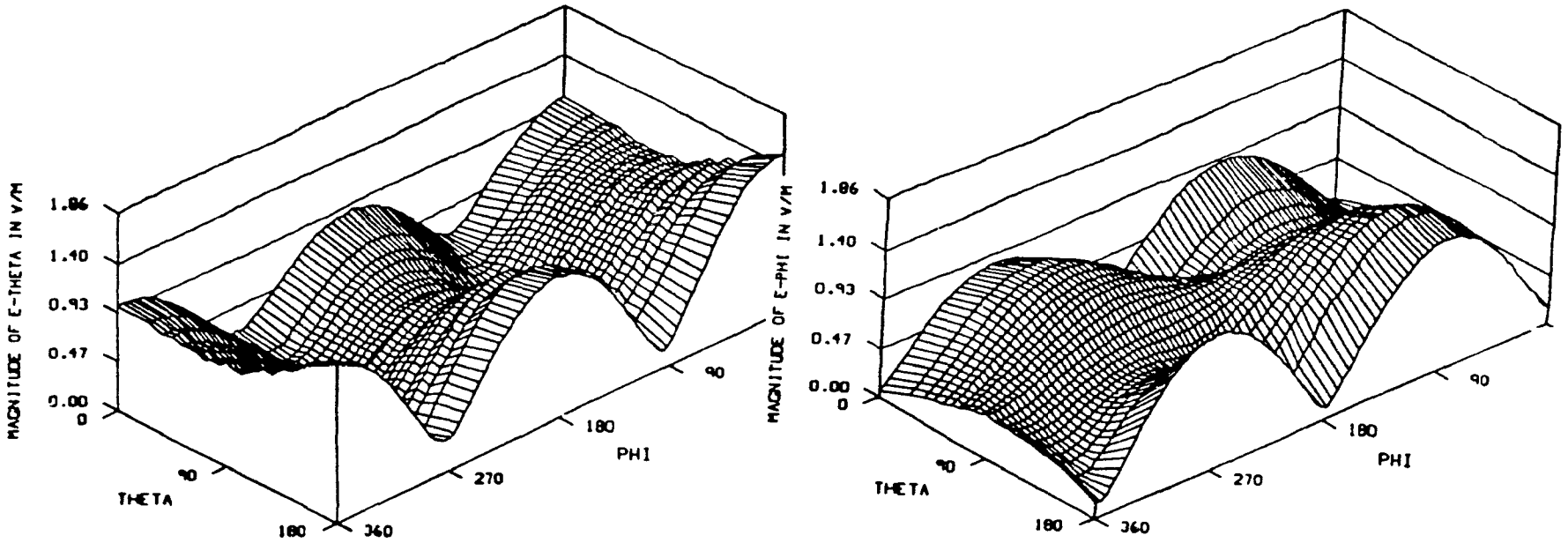

FREQUENCY = 4 MHz

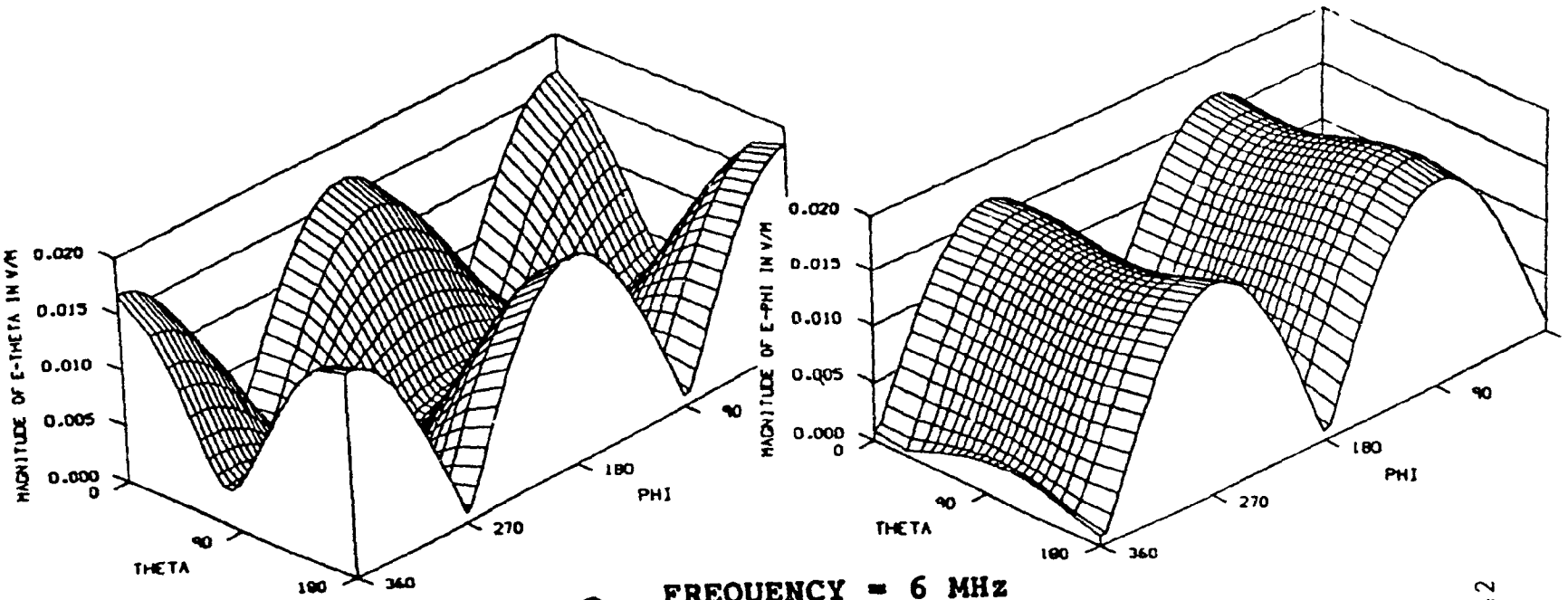

FREQUENCY = 6 MHz

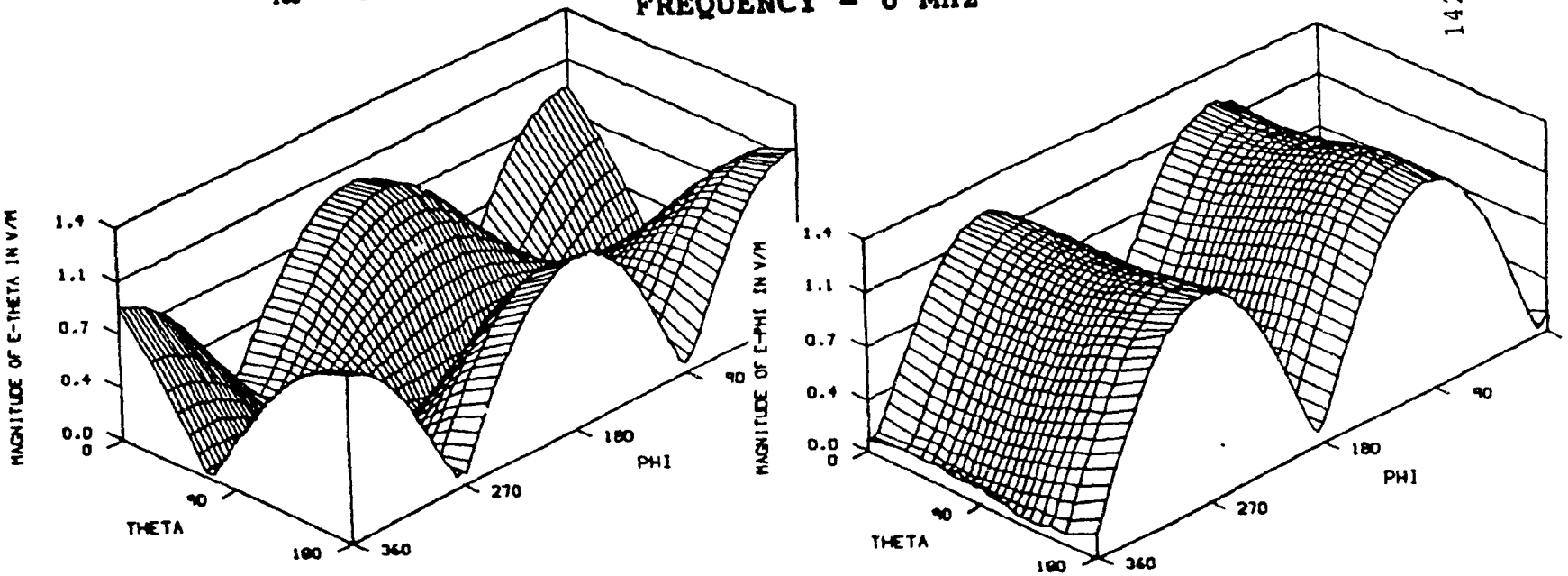

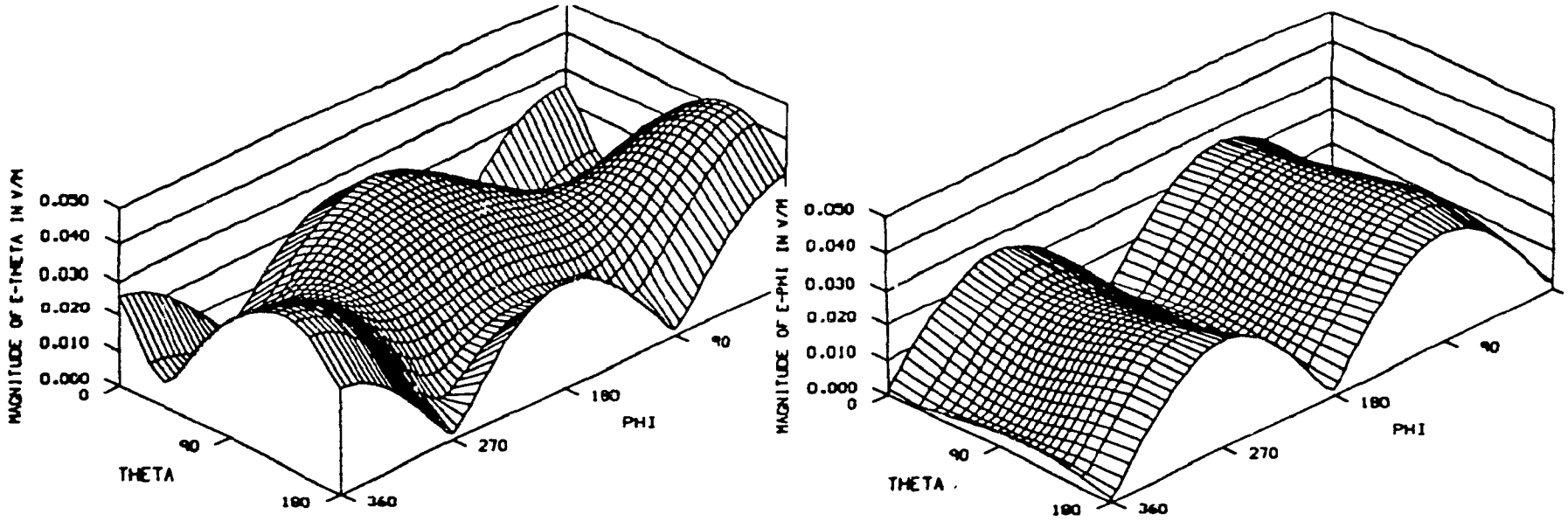

FREQUENCY = 8 MHz

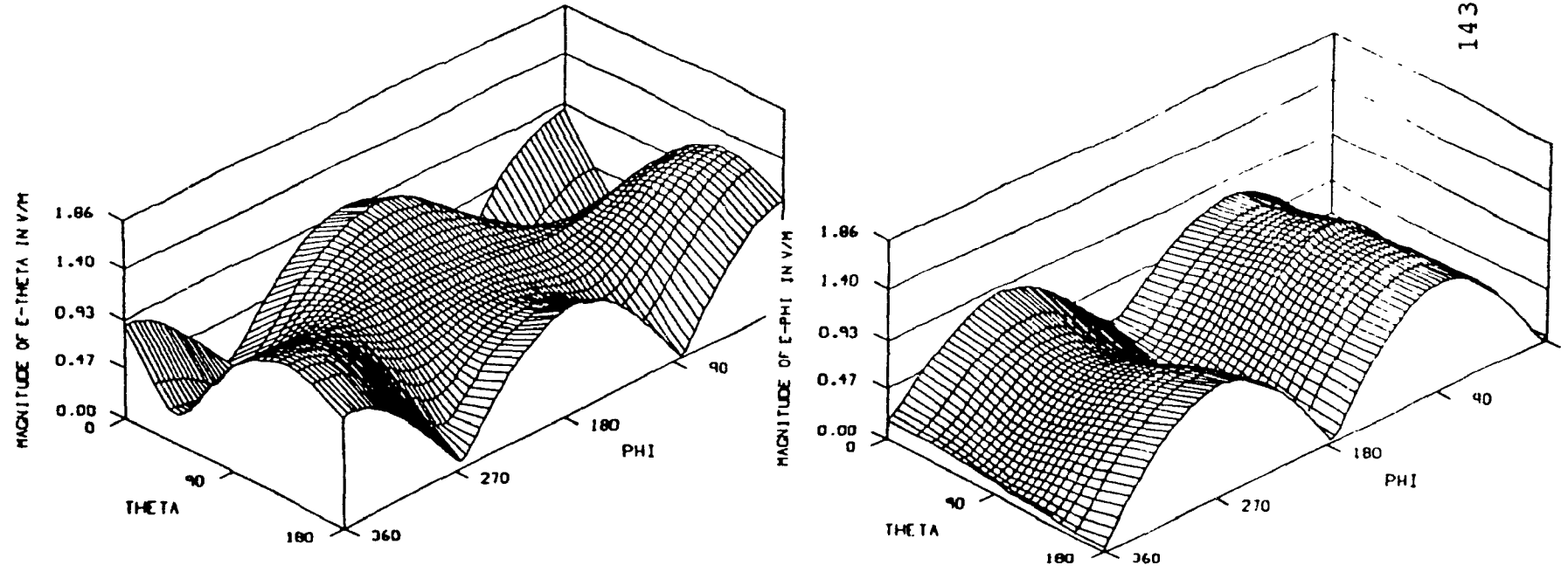

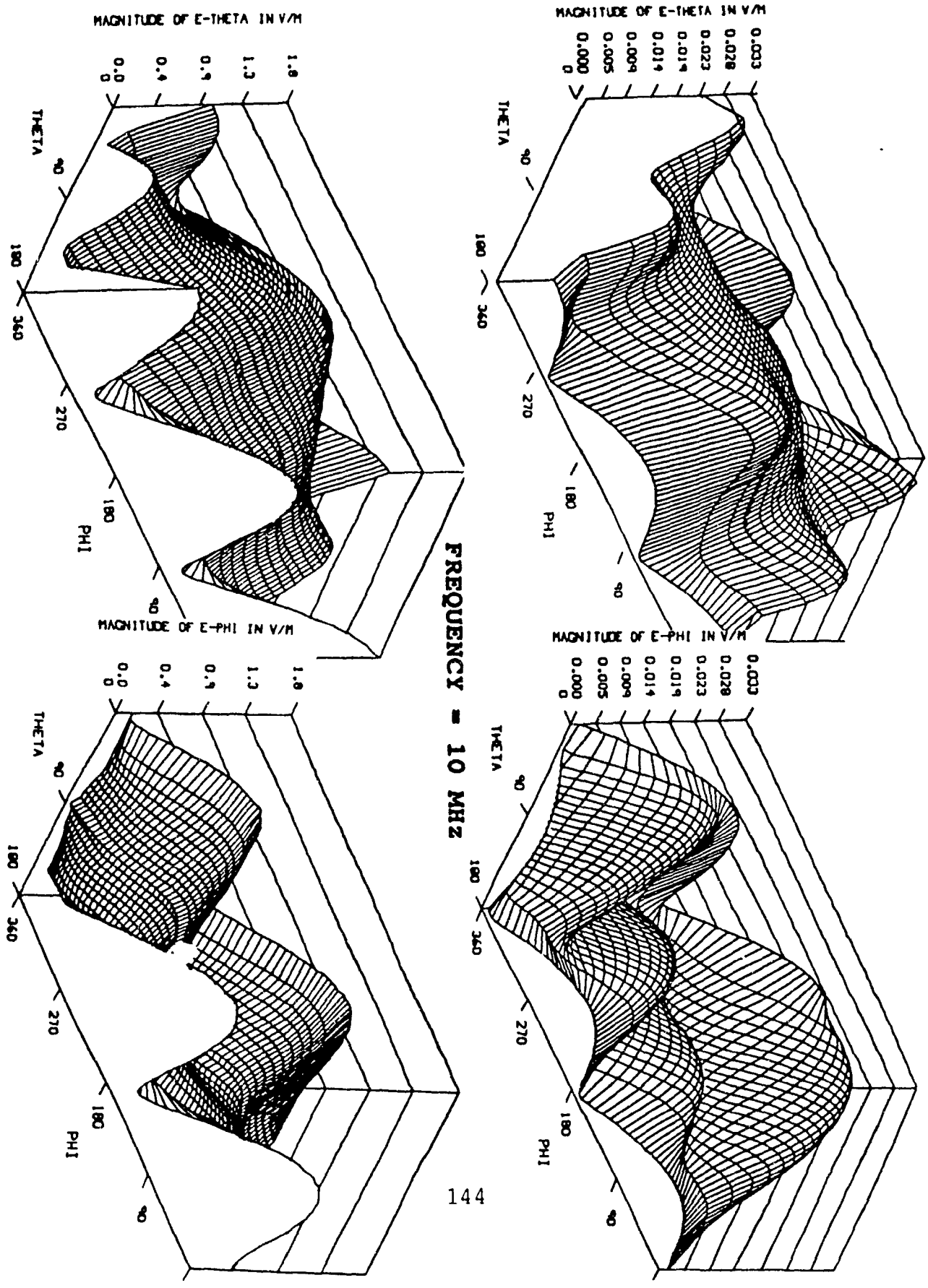

FREQUENCY = 10 MHz

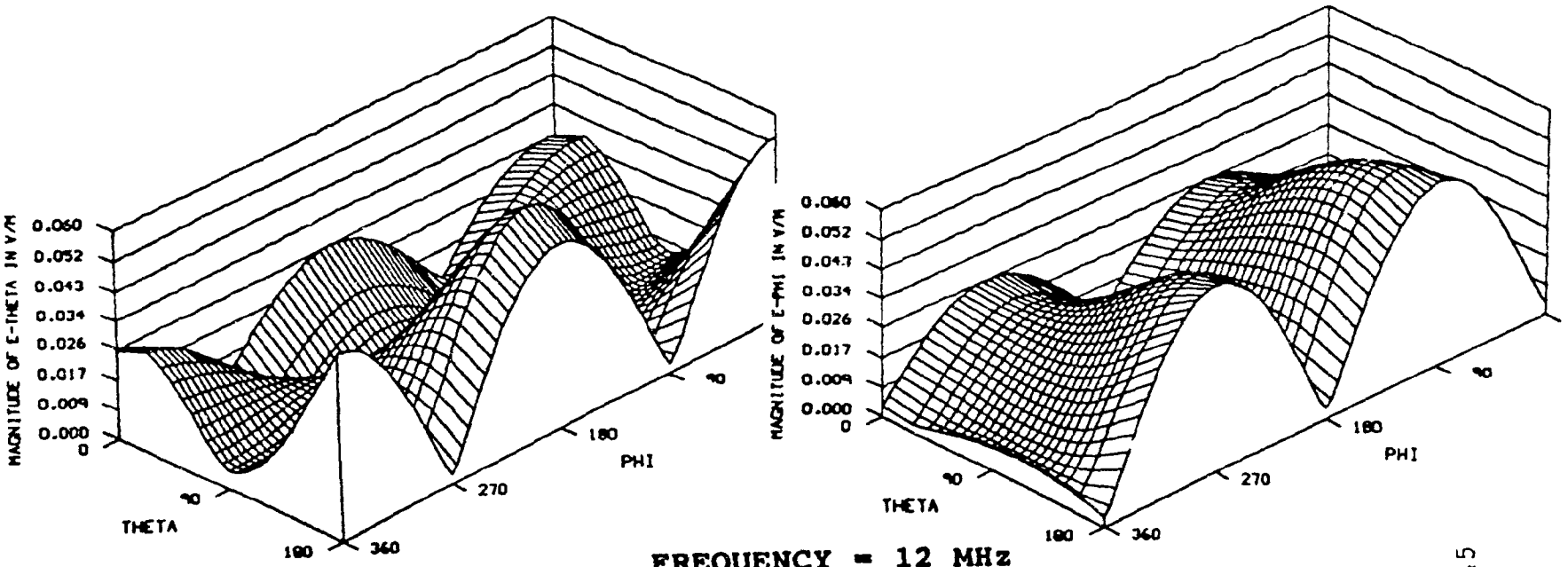

FREQUENCY = 12 MHz

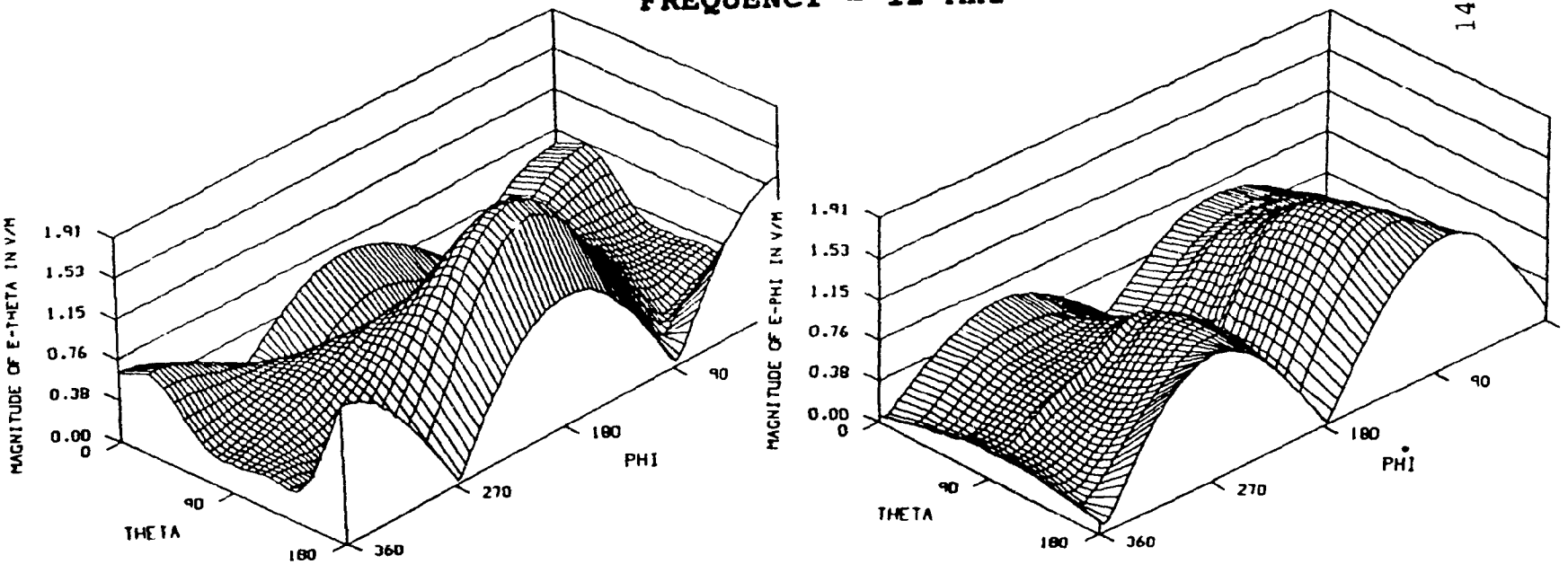

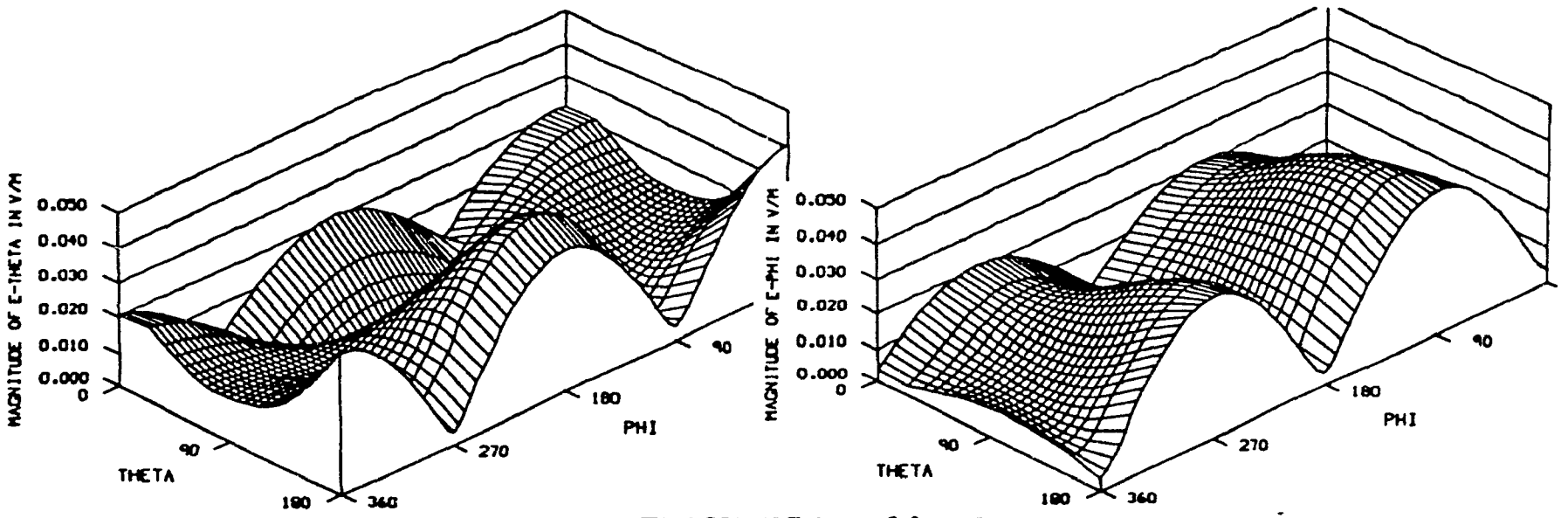

FREQUENCY = 14 MHz

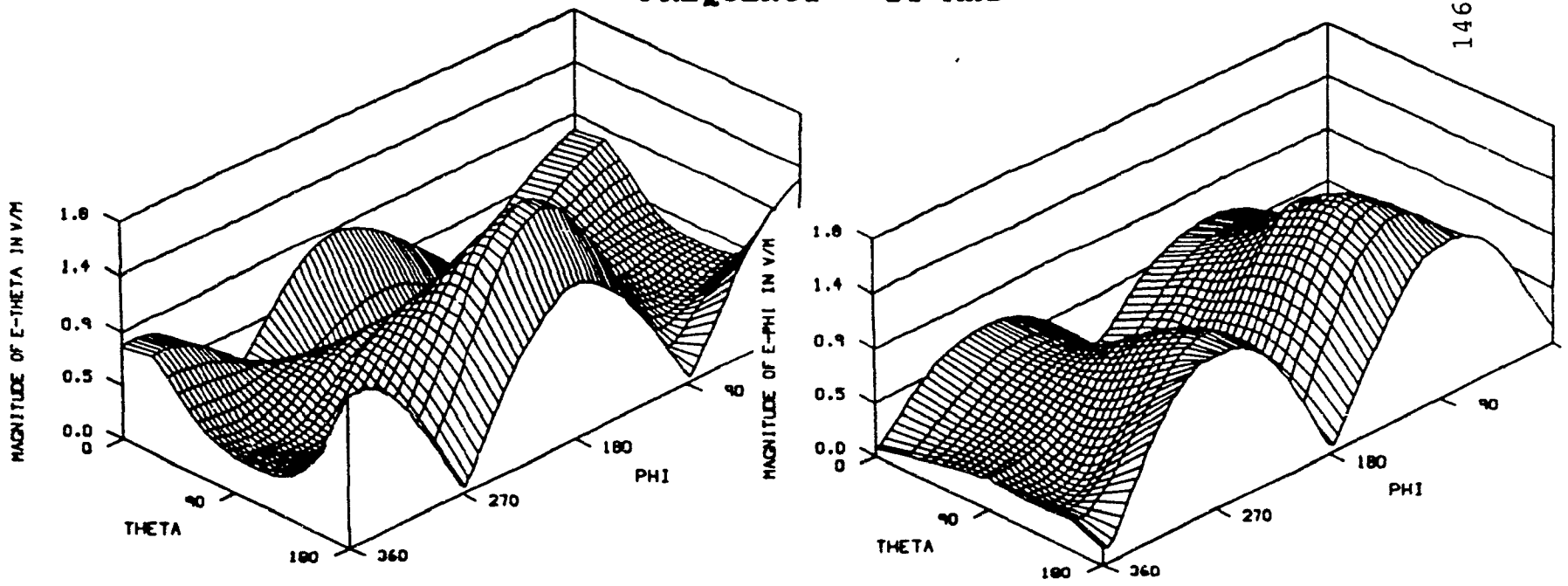

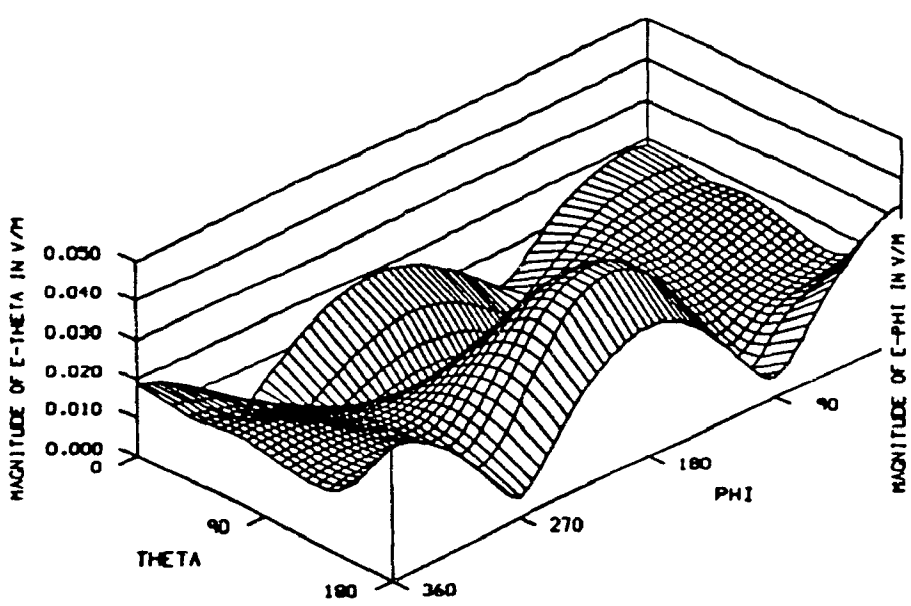

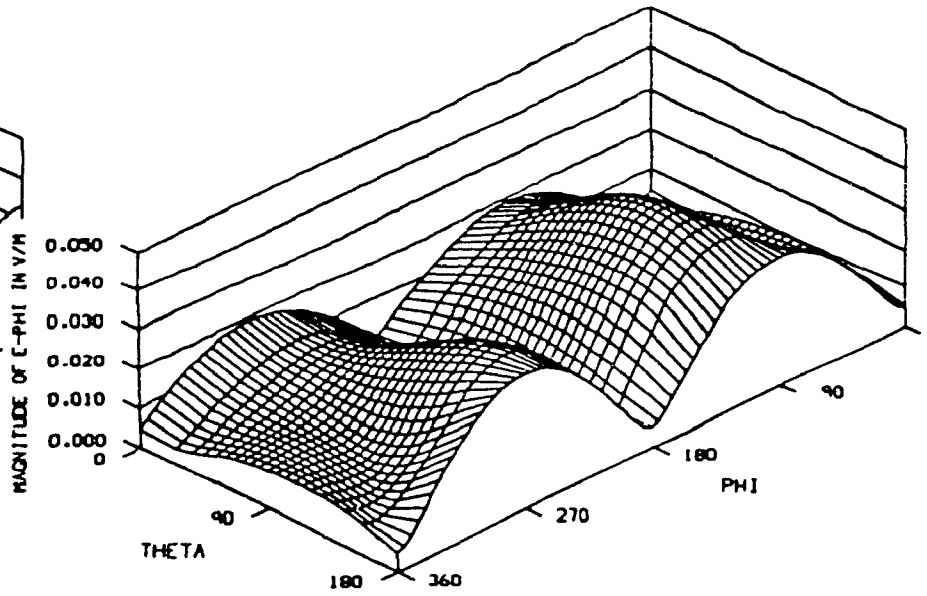

FREQUENCY = 16 MHz

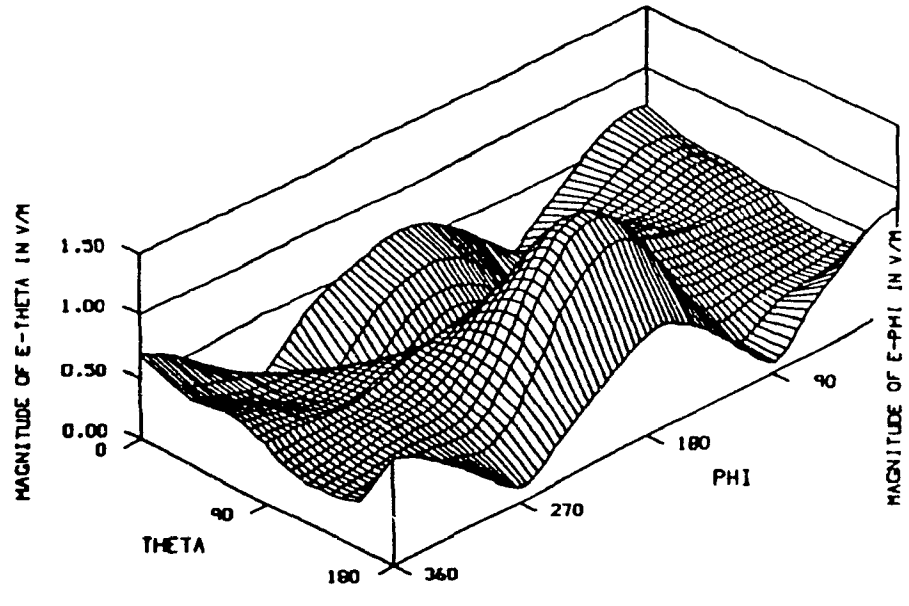

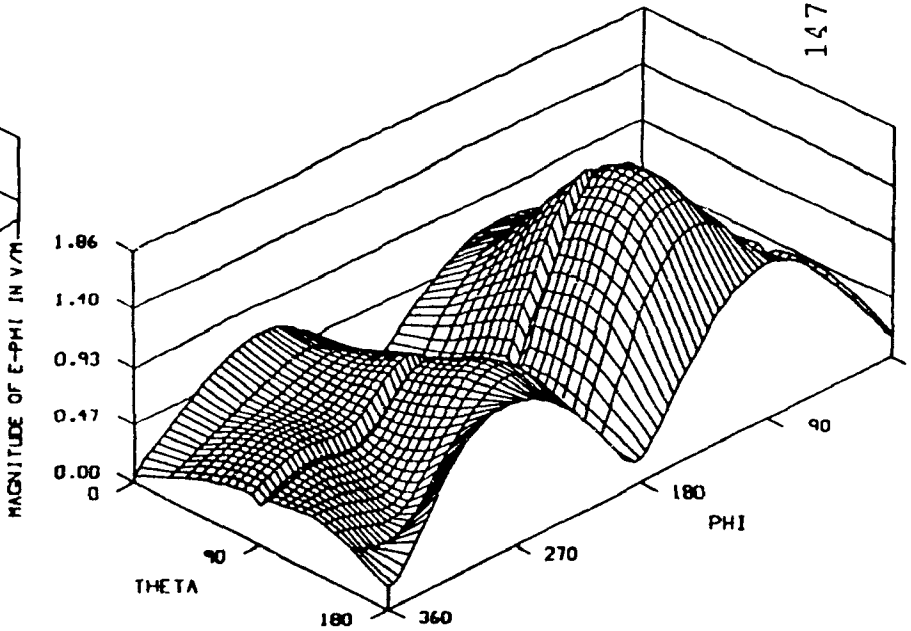

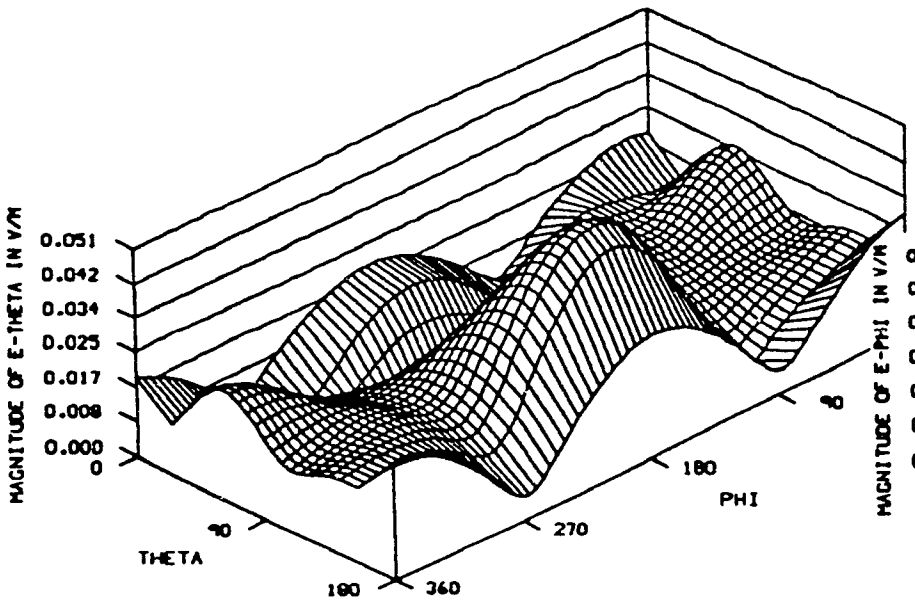

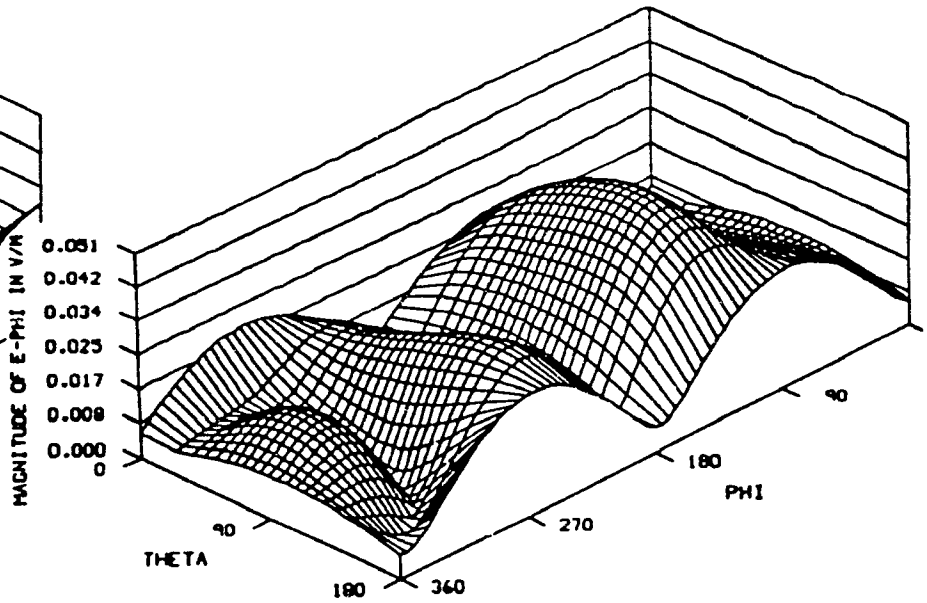

FREQUENCY = 18 MHz

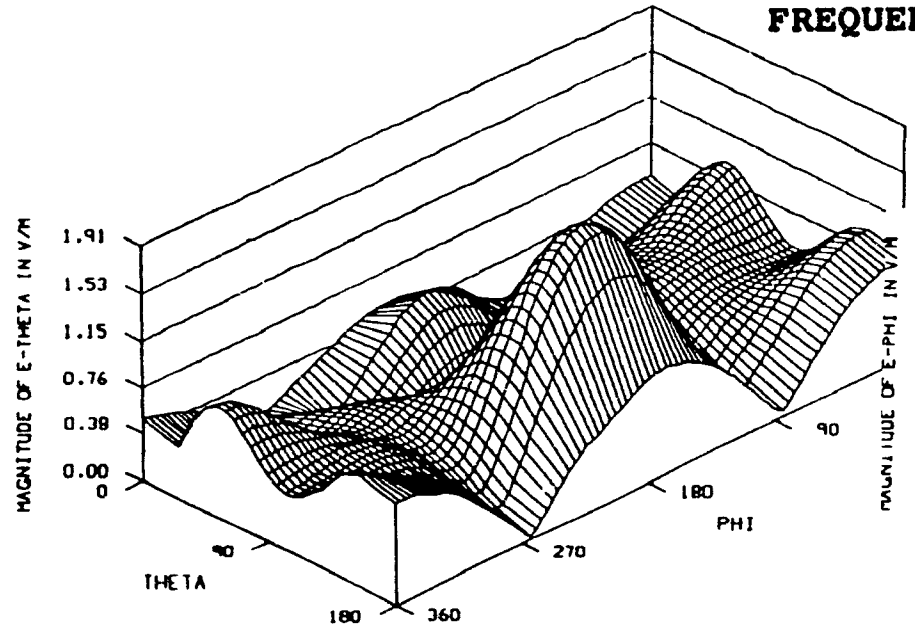

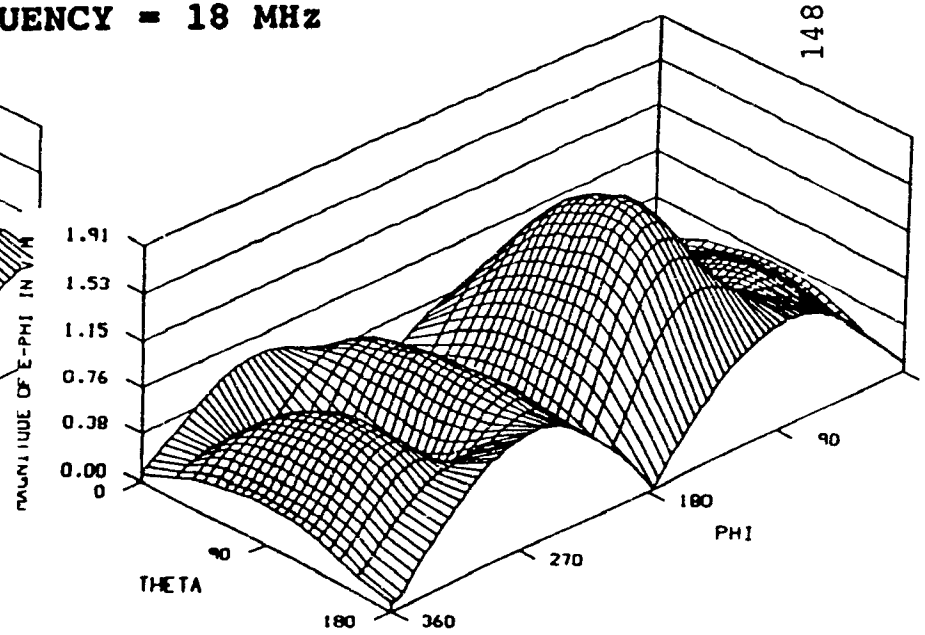

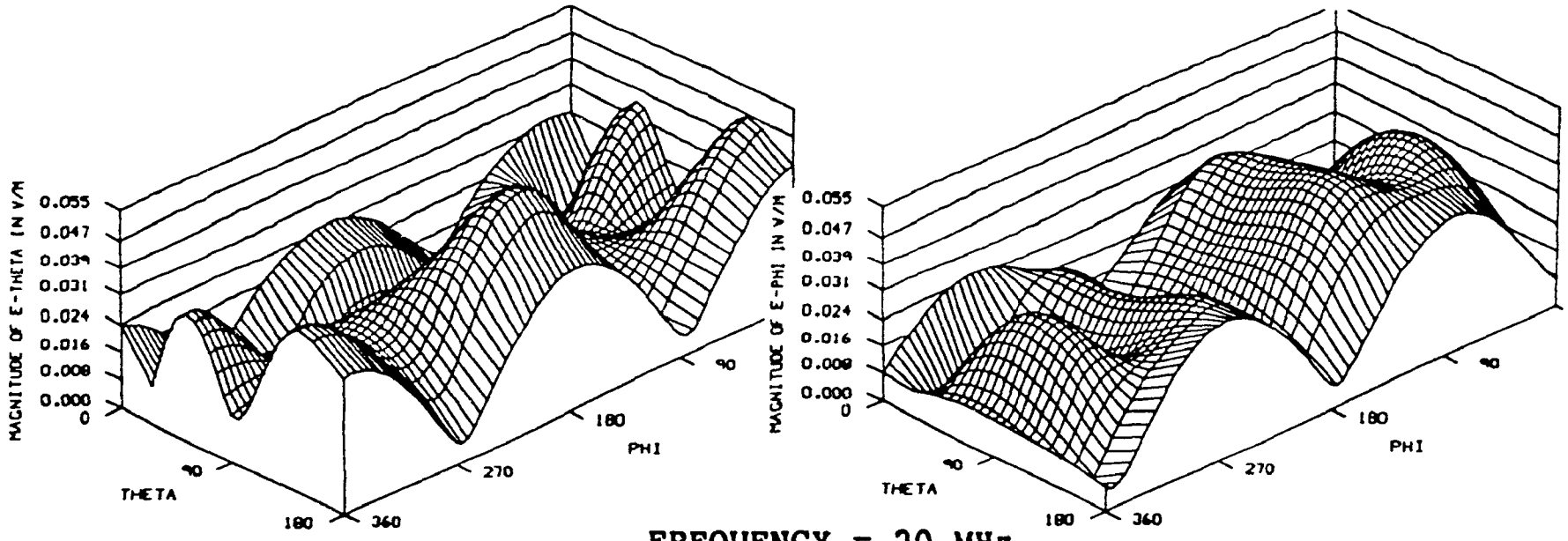

FREQUENCY = 20 MHz

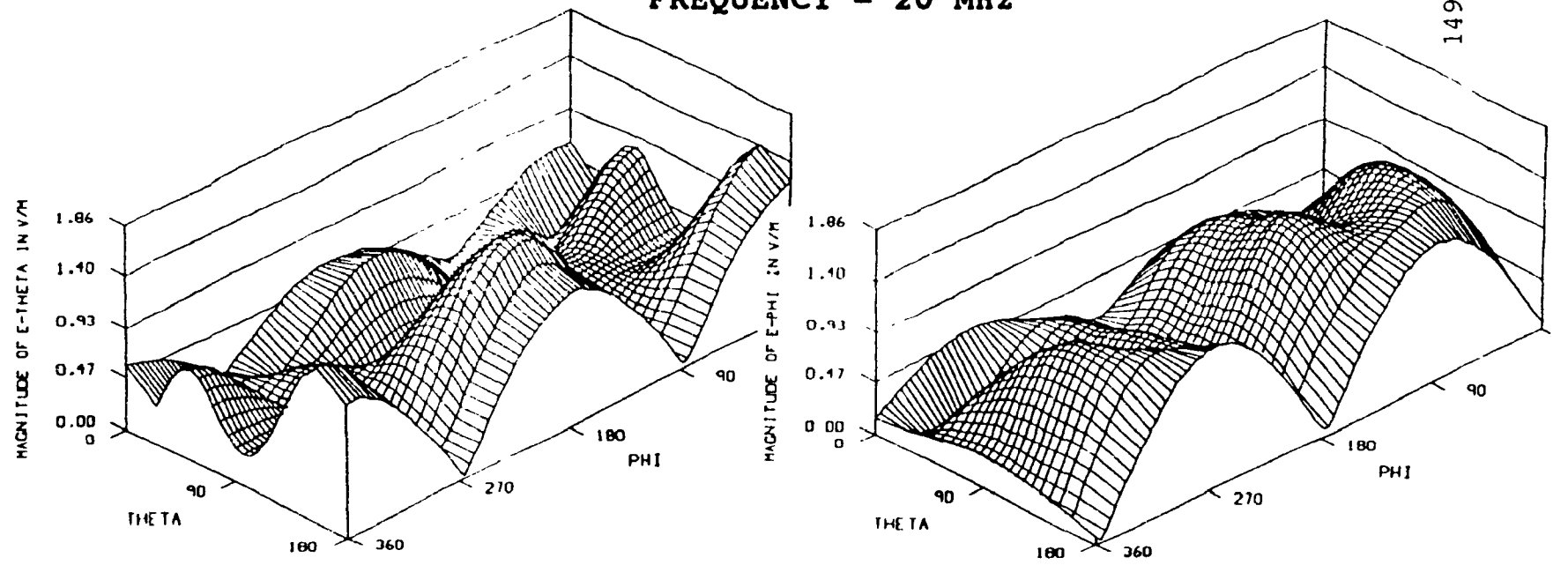

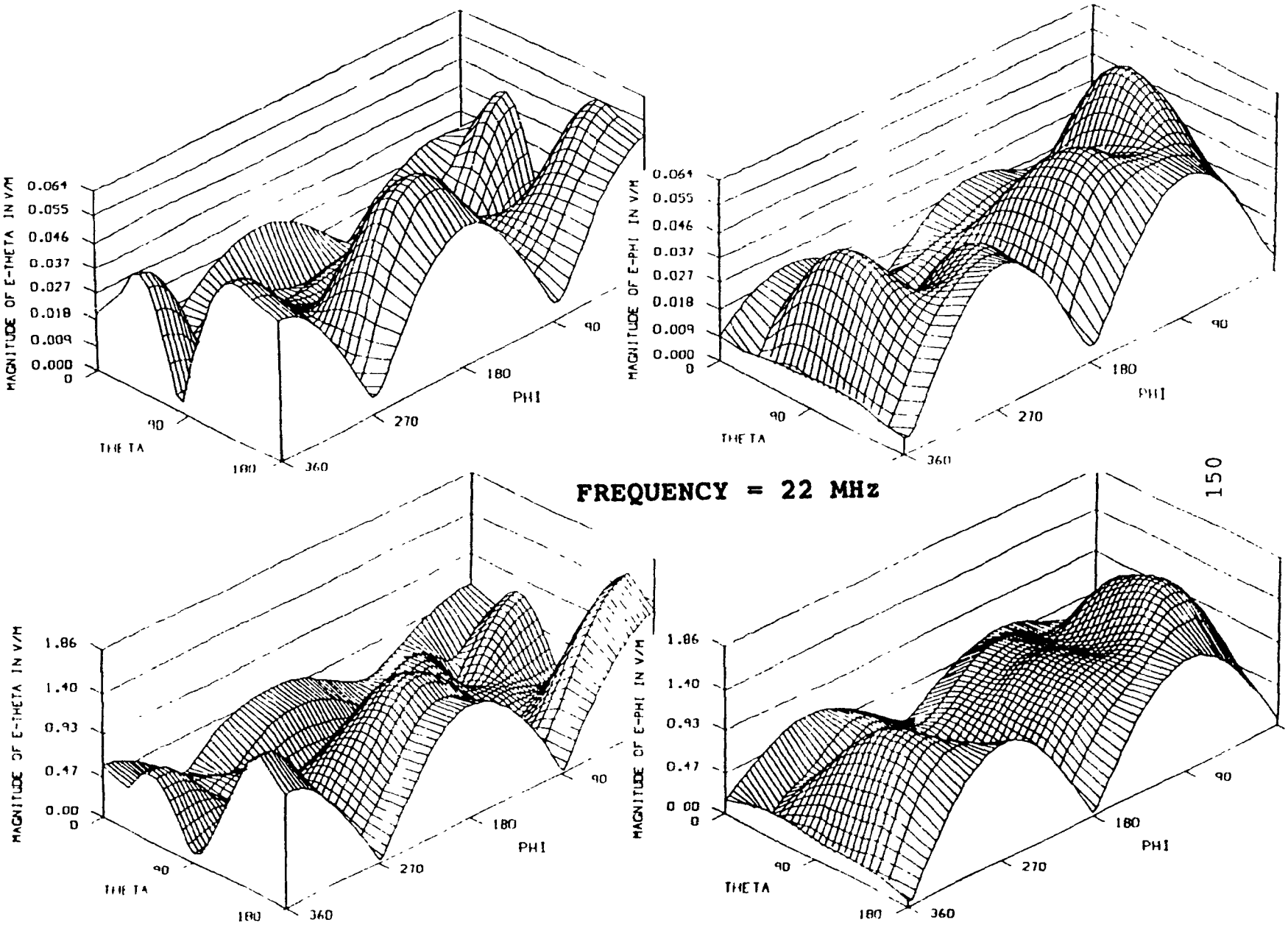
MAGNITUDE OF E-THETA IN V/M
0.064
0.055
0.046
0.037
0.027
0.018
0.009
0.000
0
90
180
360
THETA
90
180
270
PHI
MAGNITUDE OF E-PHI IN V/M
0.064
0.055
0.046
0.037
0.027
0.018
0.009
0.000
0
90
180
360
THETA
90
180
270
PHI
FREQUENCY = 22 MHz
MAGNITUDE OF E-THETA IN V/M
1.86
1.40
0.93
0.47
0.00
0
90
180
360
THETA
90
180
270
PHI
MAGNITUDE OF E-PHI IN V/M
1.86
1.40
0.93
0.47
0.00
0
90
180
360
THETA
90
180
270
PHI

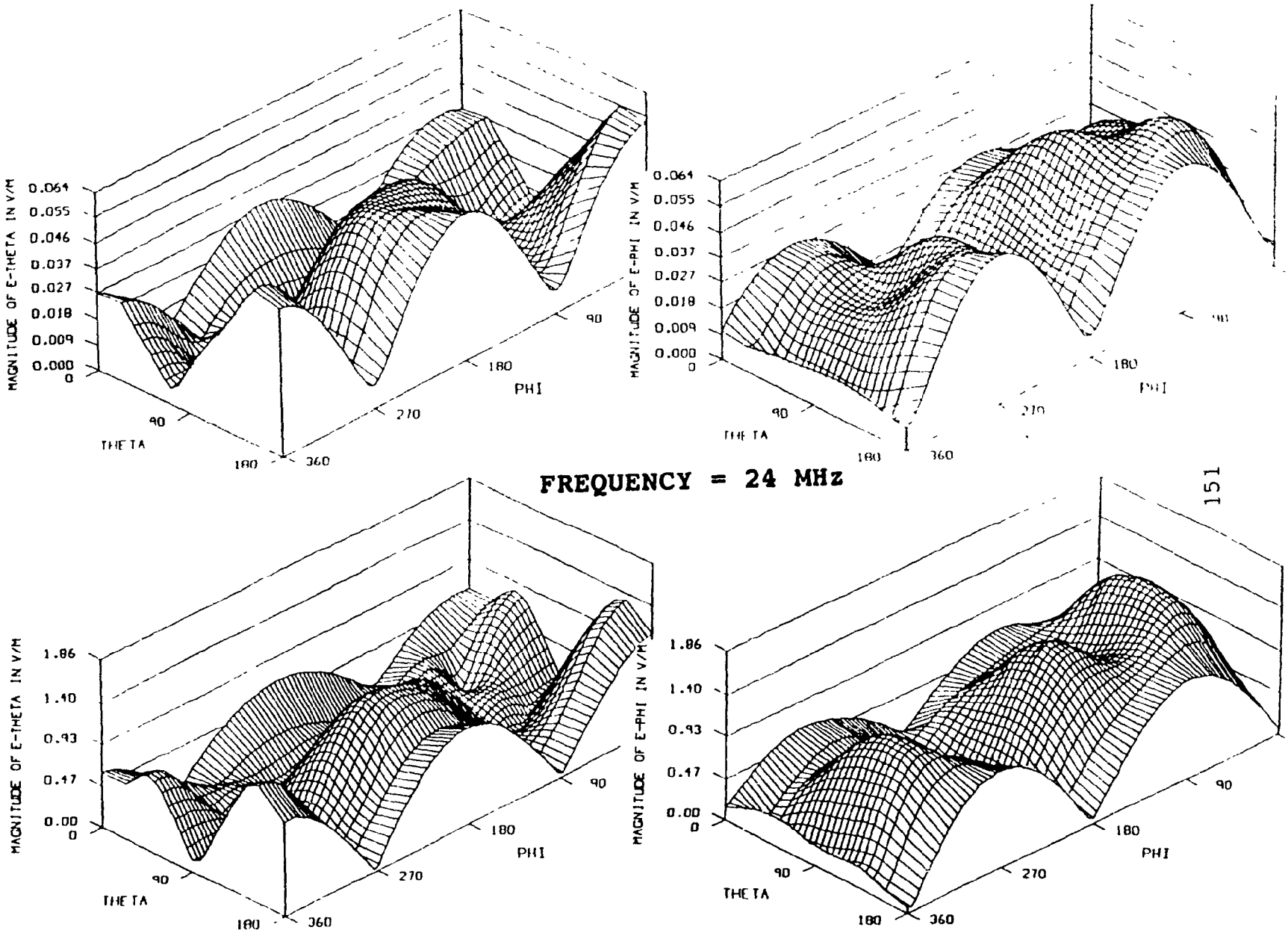

FREQUENCY = 24 MHz

FREQUENCY = 26 MHz

FREQUENCY = 28 MHz

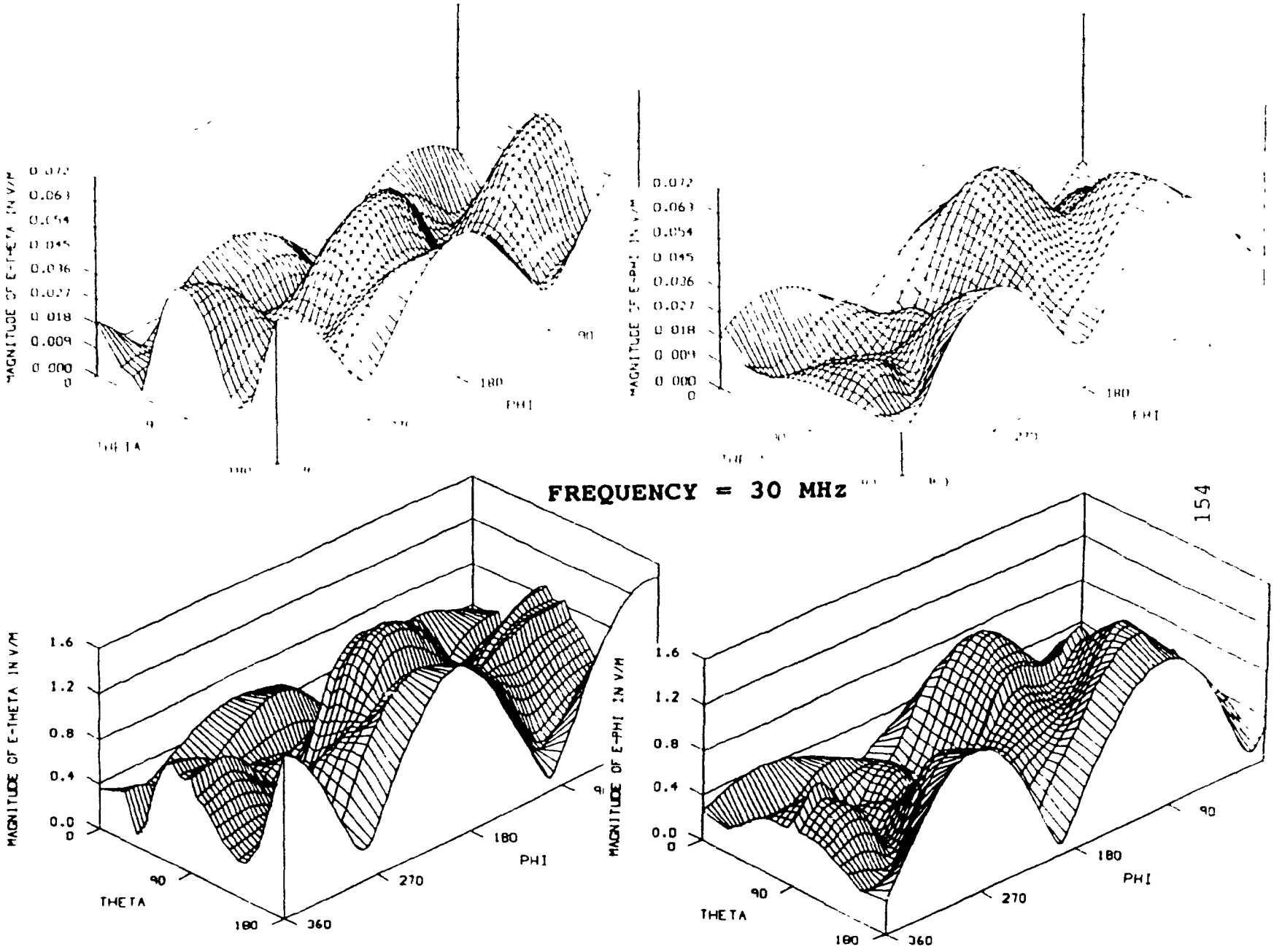
MAGNITUDE OF E-THETA IN V/M
0.072
0.063
0.054
0.045
0.036
0.027
0.018
0.009
0.000
0
90
180
PHI
THETA
MAGNITUDE OF E-PHI IN V/M
0.072
0.063
0.054
0.045
0.036
0.027
0.018
0.009
0.000
0
180
PHI
FREQUENCY = 30 MHz
MAGNITUDE OF E-THETA IN V/M
1.6
1.2
0.8
0.4
0.0
0
90
180
270
360
THETA
PHI
MAGNITUDE OF E-PHI IN V/M
1.6
1.2
0.8
0.4
0.0
0
90
180
270
360
THETA
PHI

Appendix B

Tranline antenna (model 1D with the rod installed) azimuth plane patterns computed and measured in the HF band.

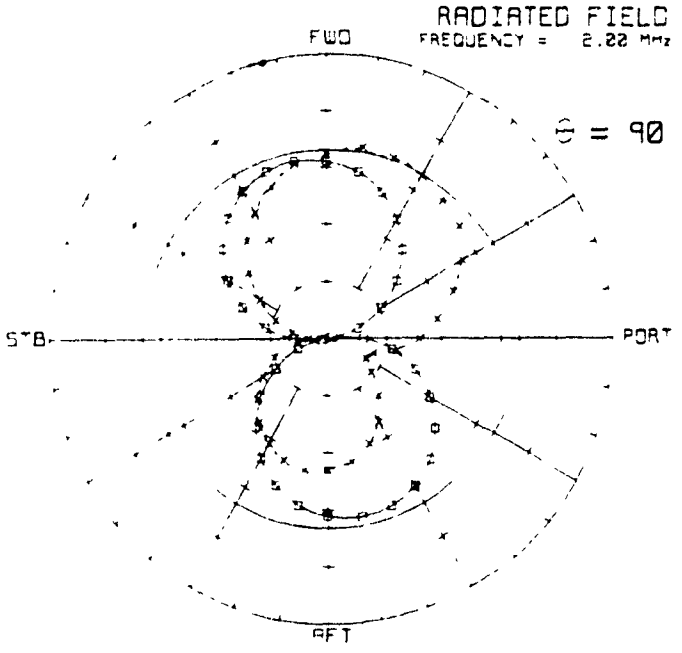
RADIATED FIELD
FREQUENCY = 2.22 MHz
FWD
Θ = 90
STB
PORT
AFT

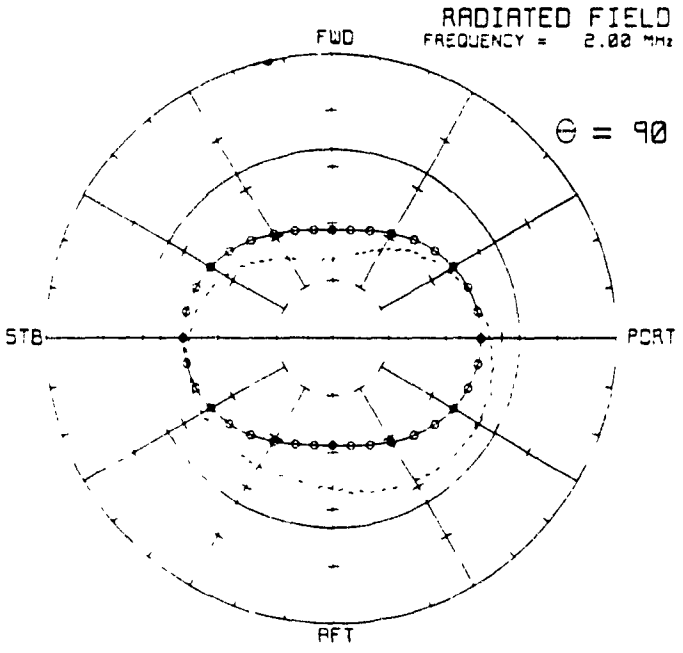
RADIATED FIELD
FREQUENCY = 2.00 MHz
FWD
Θ = 90
STB
PORT
AFT

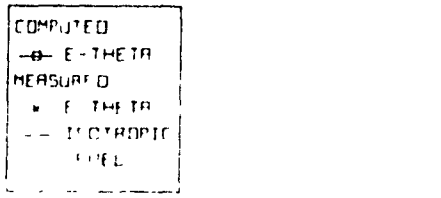
COMPUTED
E-THETA
MEASURED
E-PHI
ISOTROPIC
LEVEL

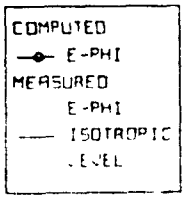
COMPUTED
E-PHI
MEASURED
E-PHI
ISOTROPIC
LEVEL

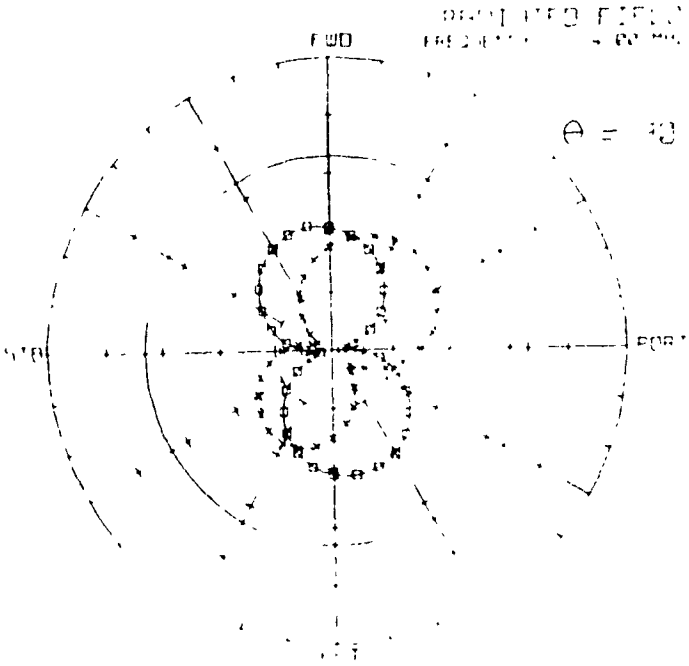
FWD
STB
AFT

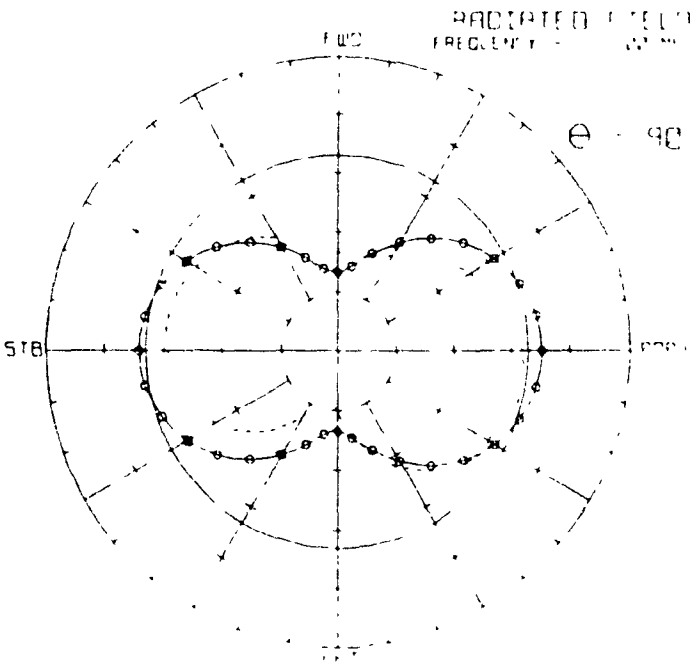
FWD
STB

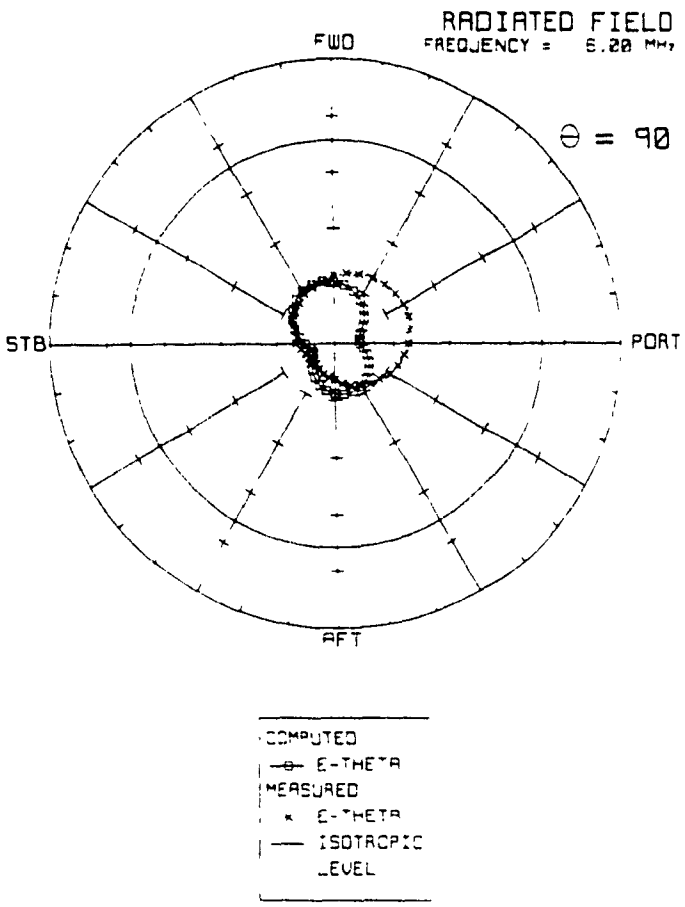
RADIATED FIELD
FREQUENCY = 6.20 MHz
FWD
θ = 90
STB
PORT
AFT
COMPUTED
E-THETA
MEASURED
E-THETA
ISOTROPIC
LEVEL

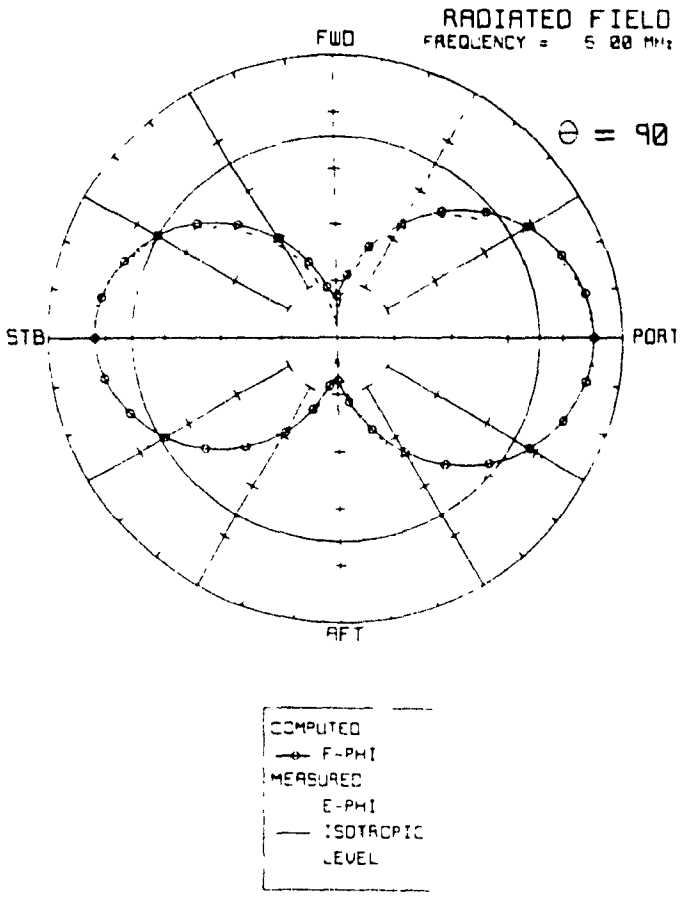
RADIATED FIELD
FREQUENCY = 6 00 MHz
FWD
θ = 90
STB
PORT
AFT
COMPUTED
E-PHI
MEASURED
E-PHI
ISOTROPIC
LEVEL

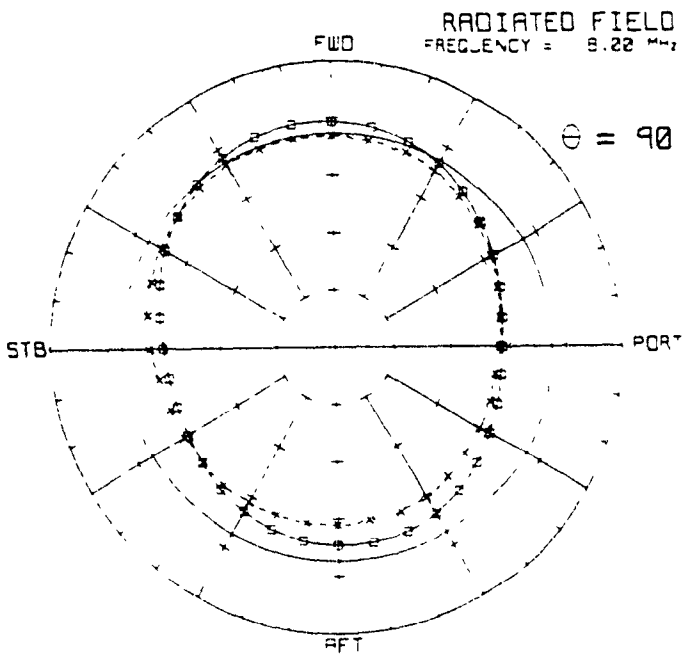
RADIATED FIELD
FREQUENCY = 8.22 MHz
FWD
θ = 90
STB
PORT
AFT

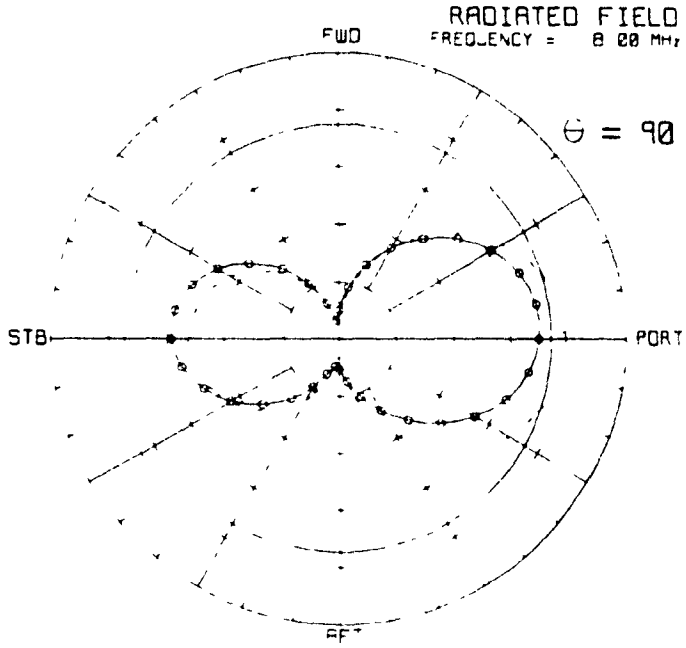
RADIATED FIELD
FREQUENCY = 8 00 MHz
FWD
θ = 90
STB
PORT
AFT

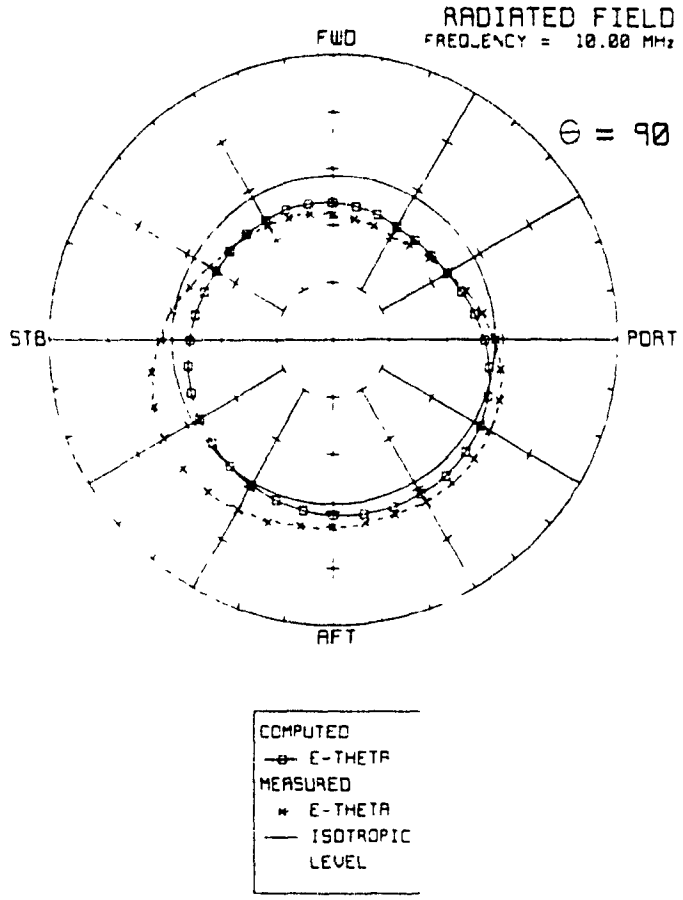
RADIATED FIELD
FREQUENCY = 10.00 MHz
FWD
Θ = 90
STB
PORT
AFT
COMPUTED
E-THETA
MEASURED
E-THETA
ISOTROPIC
LEVEL

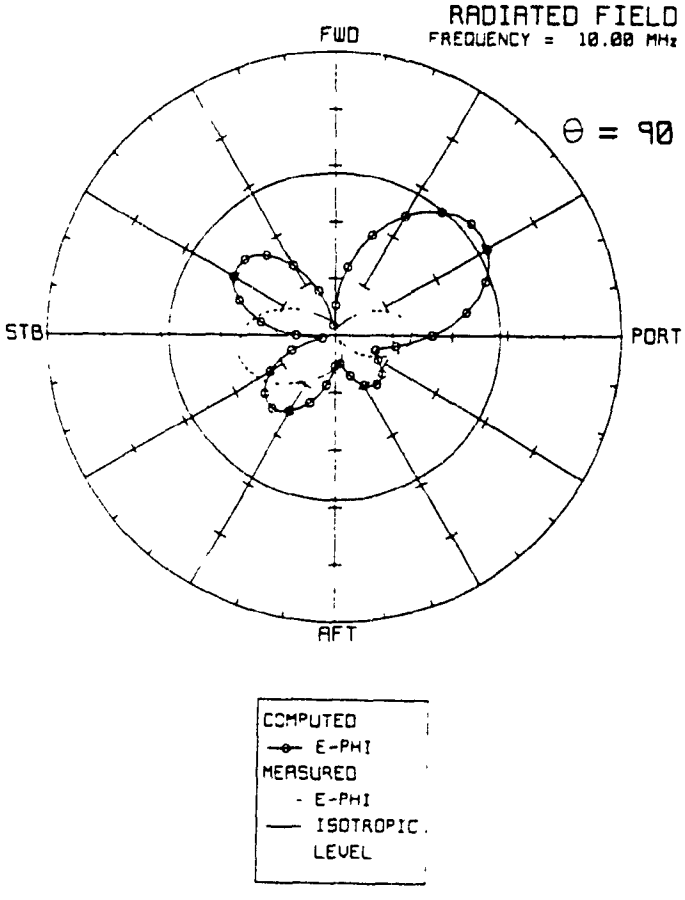
RADIATED FIELD
FREQUENCY = 10.00 MHz
FWD
Θ = 90
STB
PORT
AFT
COMPUTED
E-PHI
MEASURED
E-PHI
ISOTROPIC
LEVEL

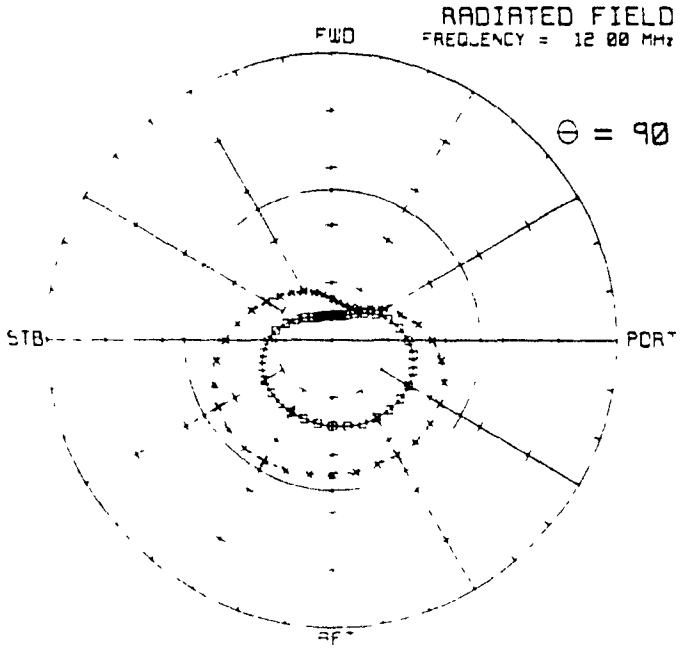
RADIATED FIELD
FREQUENCY = 12.00 MHz
FWD
Θ = 90
STB
PORT

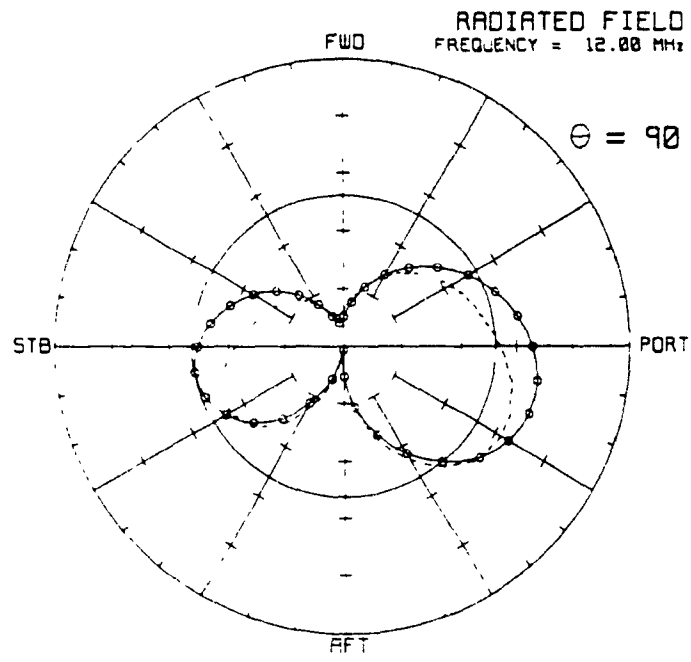
RADIATED FIELD
FREQUENCY = 12.00 MHz
FWD
Θ = 90
STB
PORT
AFT

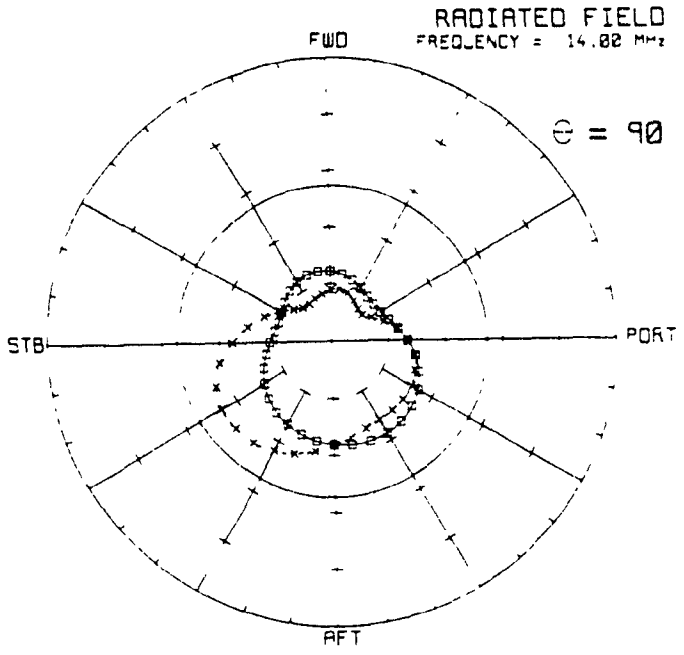
RADIATED FIELD
FREQUENCY = 14.00 MHz
FWD
Θ = 90
STB
PORT
AFT

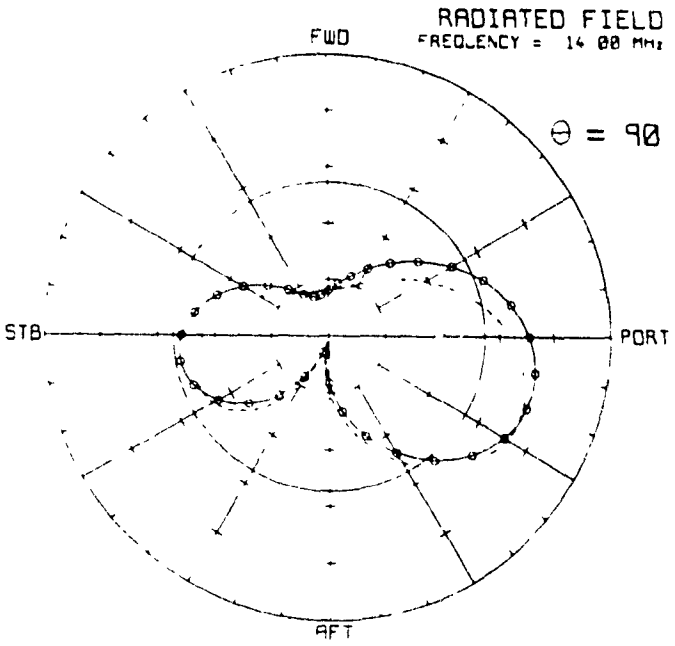
RADIATED FIELD
FREQUENCY = 14 00 MHz
FWD
Θ = 90
STB
PORT
AFT

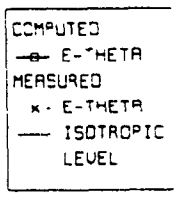
COMPUTED
E-THETA
MEASURED
E-THETA
ISOTROPIC
LEVEL

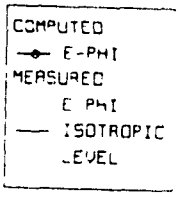
COMPUTED
E-PHI
MEASURED
E PHI
ISOTROPIC
LEVEL

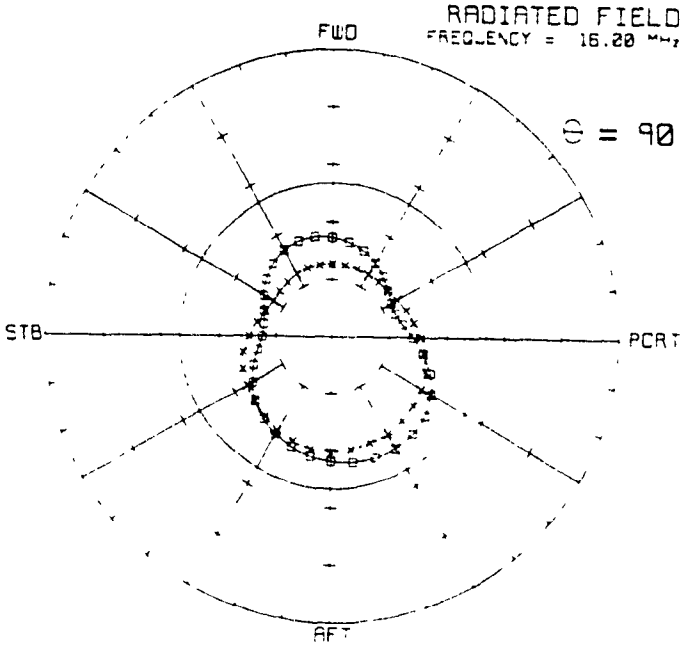
RADIATED FIELD
FREQUENCY = 16.20 MHz
FWD
Θ = 90
STB
PORT
AFT

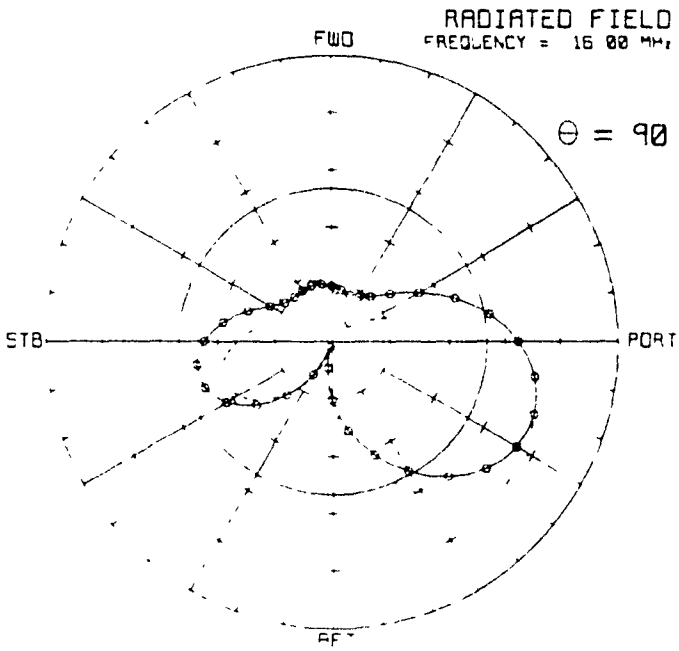
RADIATED FIELD
FREQUENCY = 16 00 MHz
FWD
Θ = 90
STB
PORT
AFT

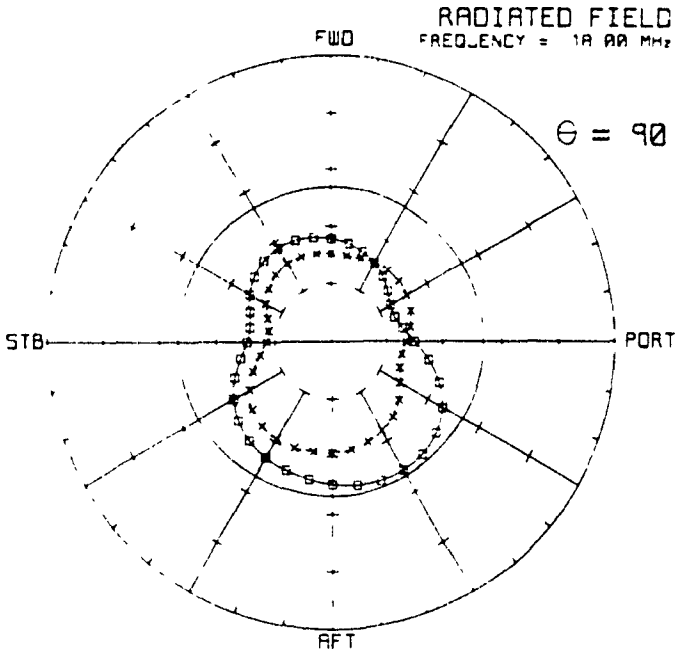
RADIATED FIELD
FREQUENCY = 18.00 MHz
FWD
θ = 90
STB
PORT
AFT

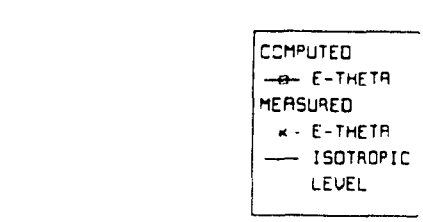
COMPUTED
E-THETA
MEASURED
E-THETA
ISOTROPIC
LEVEL

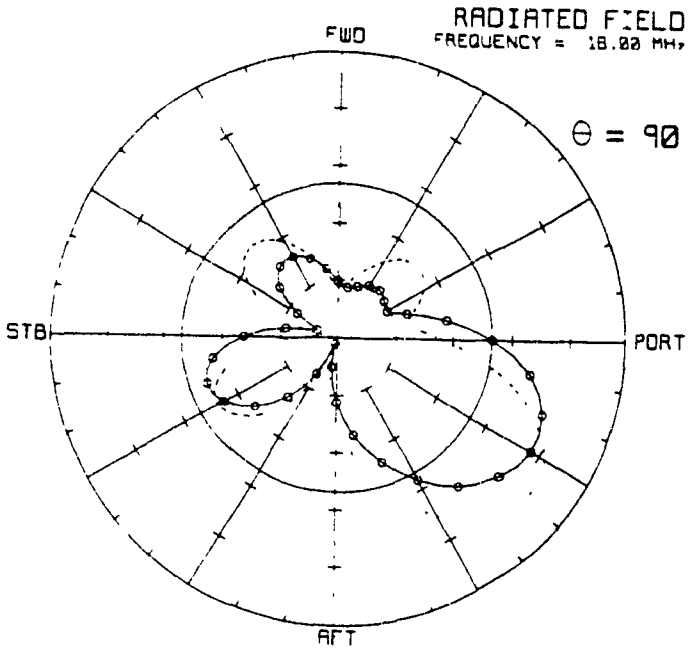
RADIATED FIELD
FREQUENCY = 18.00 MHz
FWD
θ = 90
STB
PORT
AFT

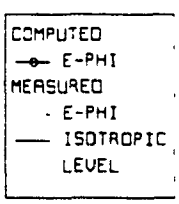
COMPUTED
E-PHI
MEASURED
E-PHI
ISOTROPIC
LEVEL

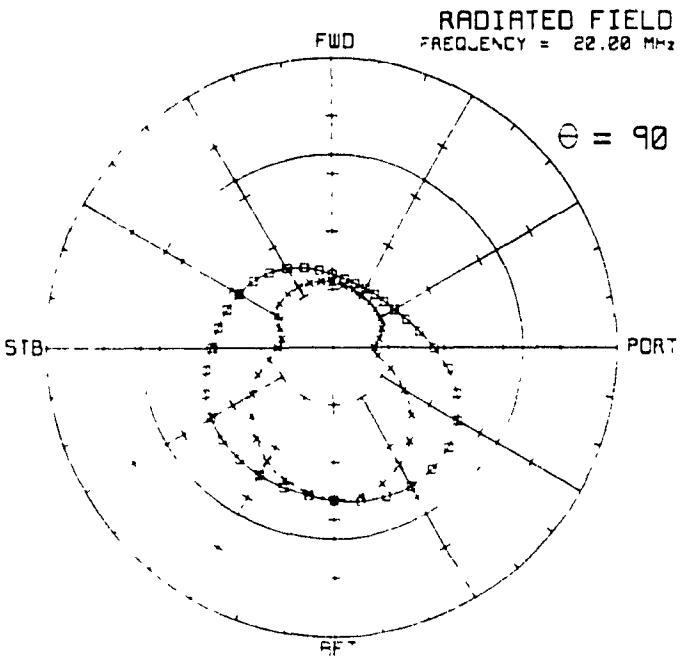
RADIATED FIELD
FREQUENCY = 22.00 MHz
FWD
θ = 90
STB
PORT
AFT

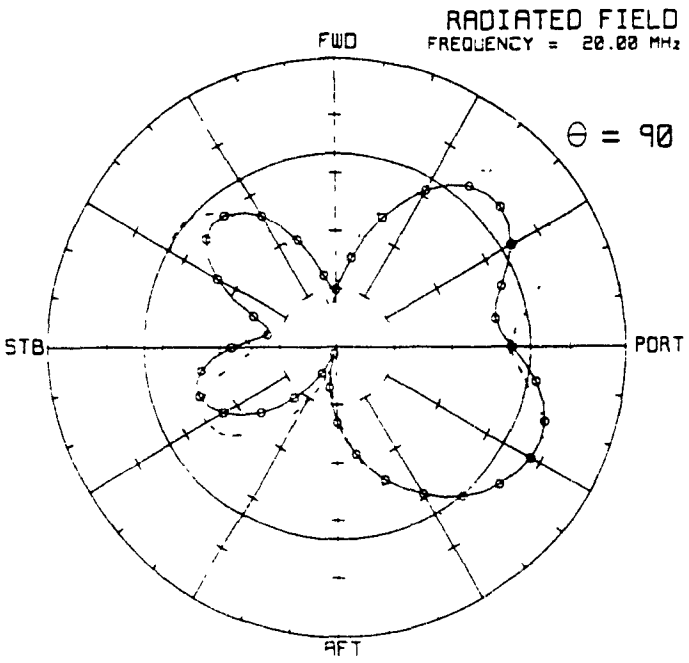
RADIATED FIELD
FREQUENCY = 20.00 MHz
FWD
θ = 90
STB
PORT
AFT

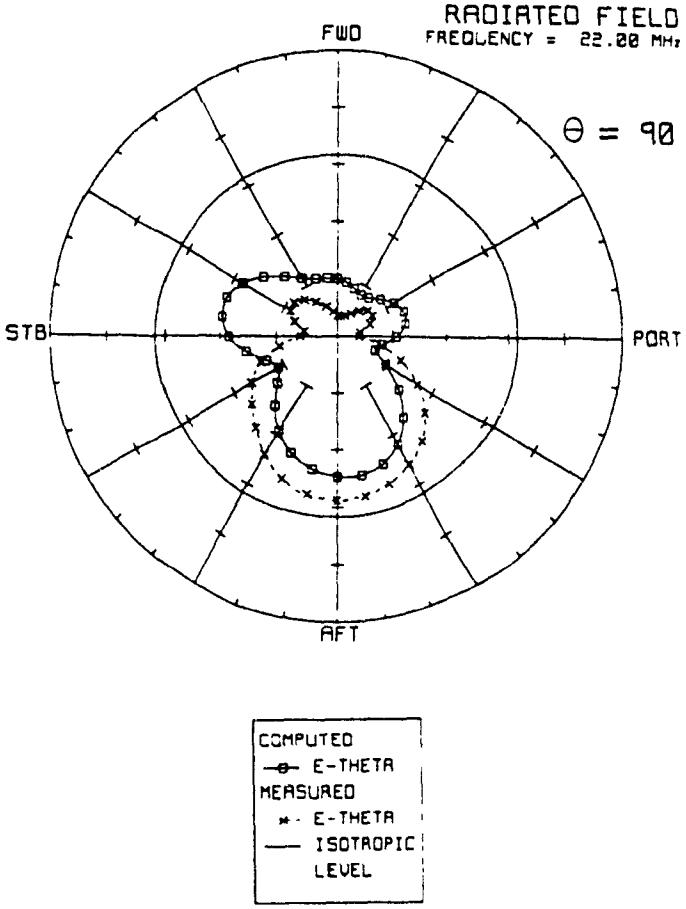
RADIATED FIELD
FREQUENCY = 22.00 MHz
FWD
Θ = 90
STB
PORT
AFT
COMPUTED
E-THETA
MEASURED
E-THETA
ISOTROPIC
LEVEL

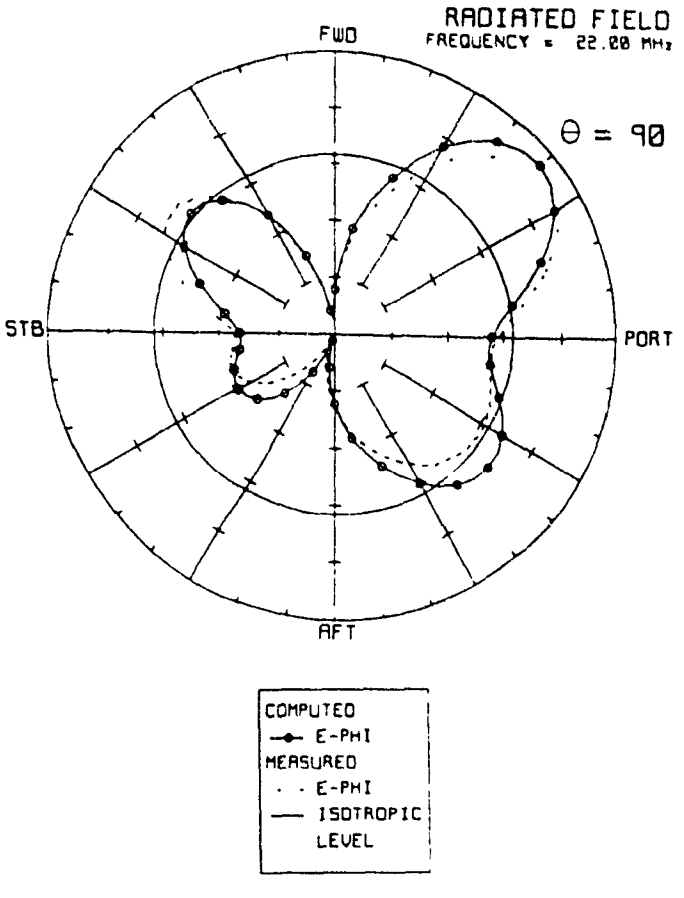
RADIATED FIELD
FREQUENCY = 22.00 MHz
FWD
Θ = 90
STB
PORT
AFT
COMPUTED
E-PHI
MEASURED
E-PHI
ISOTROPIC
LEVEL

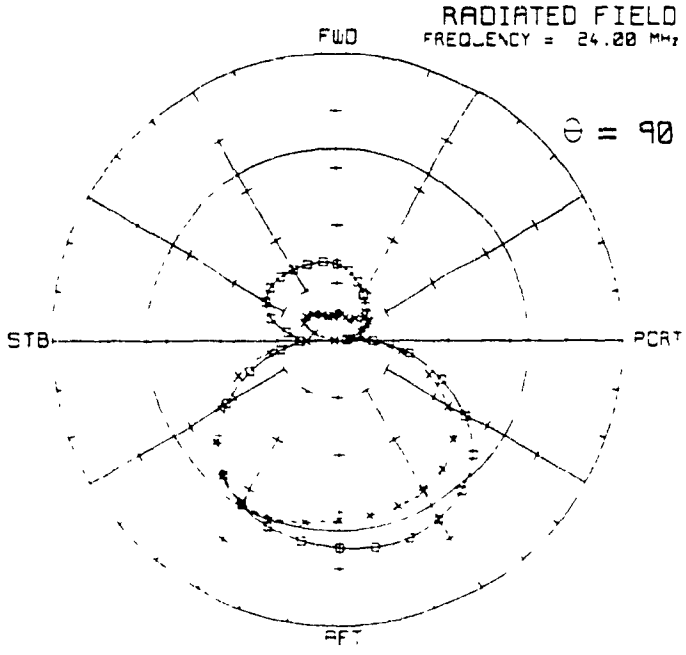
RADIATED FIELD
FREQUENCY = 24.00 MHz
FWD
Θ = 90
STB
PORT
AFT

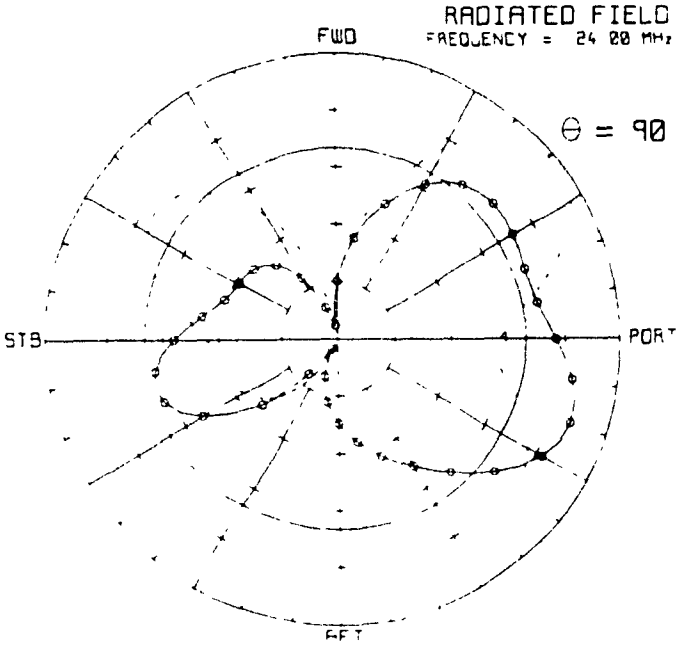
RADIATED FIELD
FREQUENCY = 24.00 MHz
FWD
Θ = 90
STB
PORT
AFT

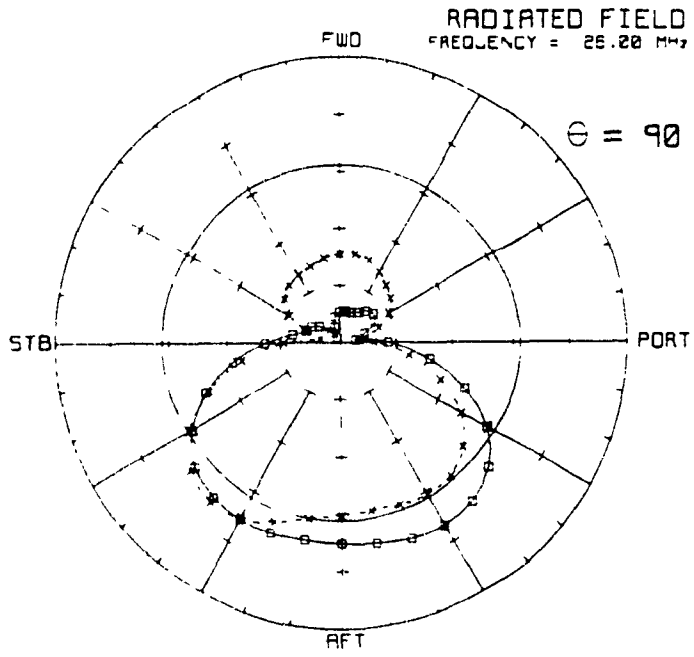
RADIATED FIELD
FREQUENCY = 26.20 MHz
FWD
θ = 90
STB
PORT
AFT

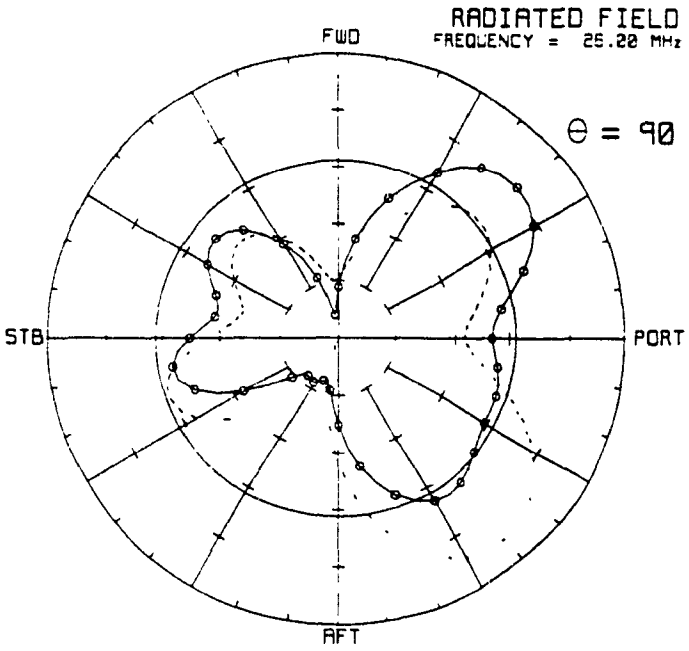
RADIATED FIELD
FREQUENCY = 26.20 MHz
FWD
θ = 90
STB
PORT
AFT

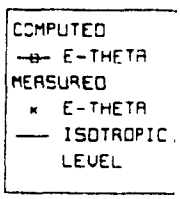
COMPUTED
E-THETA
MEASURED
E-THETA
ISOTROPIC
LEVEL

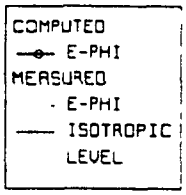
COMPUTED
E-PHI
MEASURED
E-PHI
ISOTROPIC
LEVEL

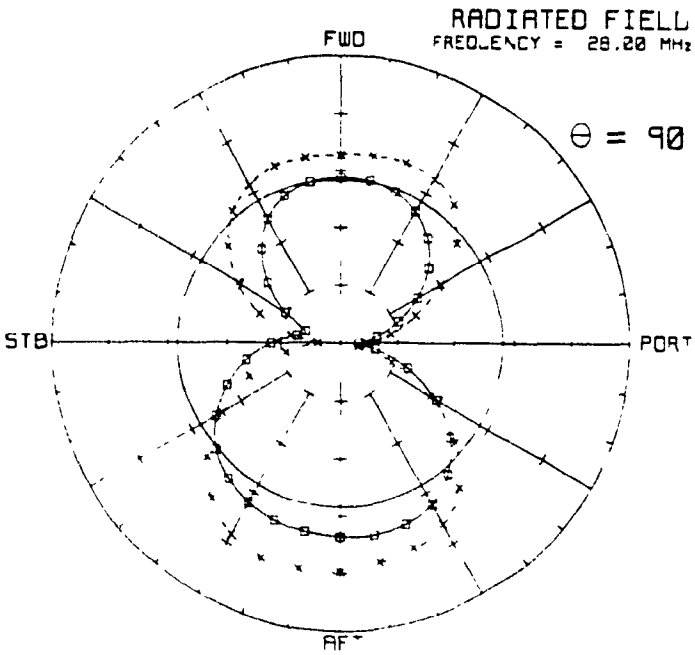
RADIATED FIELD
FREQUENCY = 28.20 MHz
FWD
θ = 90
STB
PORT
AFT

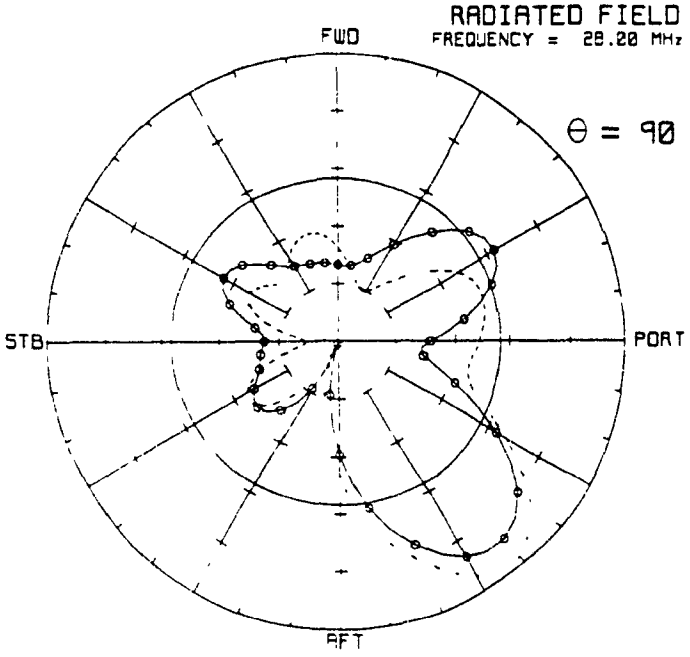
RADIATED FIELD
FREQUENCY = 28.20 MHz
FWD
θ = 90
STB
PORT
AFT

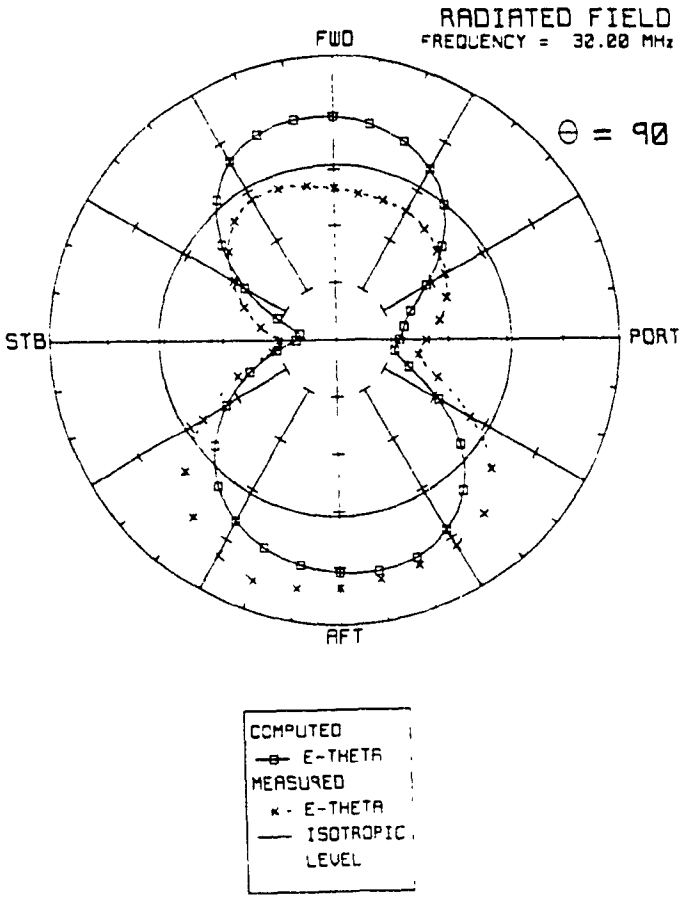
RADIATED FIELD
FREQUENCY = 32.00 MHz
FWD
Θ = 90
STB
PORT
AFT
COMPUTED
E-THETA
MEASURED
E-THETA
ISOTROPIC
LEVEL

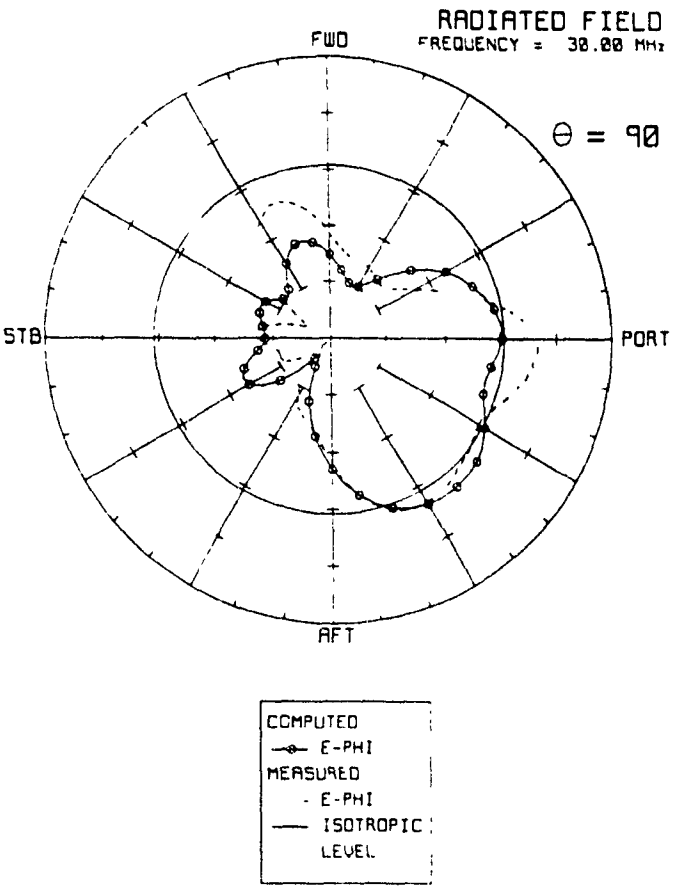
RADIATED FIELD
FREQUENCY = 30.00 MHz
FWD
Θ = 90
STB
PORT
AFT
COMPUTED
E-PHI
MEASURED
E-PHI
ISOTROPIC
LEVEL

REFERENCES

[1]. C. A. Balanis, Advanced Engineering Electromagnetics, Wiley, New york, 1989.

[2]. R. F. Harrington, Field Computation By Moment Methods, Macmillan, Newyork, 1968.

[3]. W. L. Stutzman and G. A. Thiele, Antenna Theory and Design, Wiley, Newyork, 1981.

[4]. J. H. Richmond,"A Wire-Grid Model for Scattering by Conducting Bodies,"*IEEE Trans. Antenn. Propag.*, Vol. AP-14, no.6, pp 782-786, November 1966.

[5]. M. M. Ney,"Method of Moments as Applied to Electromagnetic Problems,"*IEEE Trans. Microwave Theory Tech.*, Vol. MTT-33, no. 10, pp 972-980, October 1985.

[6]. D. S. Jones,"Numerical Methods for Antenna Problems,"*Proc. IEE*, Vol.121, no.7, pp 573-582, July 1974.

[7]. S. A. Schelkunoff and H. T. Friss, Antennas Theory and Practice, Wiley, Newyork, 1952.

[8]. G. A. Thiele,"Wire Antennas," Chapter 2 in *Computer Techniques for Electromagnetics*, Pergm an Press, Newyork, 1973.

[9]. D. R. Wilton and C. M. Butler,"Efficient Numerical Techniques for Solving Pocklington's Equation and Their Relationship to Other Methods,"*IEEE Trans. Antennas Propagat.* pp 83-8 6, January 1976.

[10]. L. L. Tsai,"A Numerical Solution for the Near a nd Far Fields of An Antenna Ring of Magnetic Current,"*IEEE Trans. Antennas Propagat.*, Vol. A P-20, no.5, pp 569-576, September 1972.

[11]. R. F. Harrington,"Matrix Methods for Field Problems,"*Proc. IEEE*, Vol. 55, no.2, pp 136-144

, February 1967.

[12]. R. L. Tanner and M. G. Anderson,"Numerical Solutions Of Electromagnetic Problems,"*IEEE Spectrum*, pp 53-61, September 1967.

[13]. L. W. Pearson and C. M. Butler,"Inadequacies of Collocation Solutions to Pocklington-Type Models of Thin-Wire Structures,"*IEEE Trans. Antennas Propagat.*, pp 295-298, March 1975.

[14]. E. K. Miller,"A Selective Survey of Computational Electromagnetics,"*IEEE Trans. Antennas Propagat.*, Vol. 36, no.9, pp 1281-1304, September 1988.

[15]. G. J. Burke and A. J. Poggio,"Numerical Electromagnetic Code (NEC)-Method of Moments,"*Technical Document 116*, Naval Ocean Systems Centre, San Diago, Calif., September 6, 1981.

[16]. C. A. Klien and R. Mittra, "The Effect of Different Testing Functions In the Moment Method Solution of Thin-Wire Antenna Problem,"*IEEE Trans. Antenna Propagat.*, pp 258-261, March 1975.

[17]. E. K. Miller,"An Evolution of Computer Programs Using Integral Equations For the Electromagnetic Analysis of Thin Wire Structures," UCRL-75566, Lawrence Livermore Laboratory, CA., March 1974.

[18]. C. L. Larose, Advances in Wire-Grid Modelling of Antennas and Auxiliary Computer Graphics System With the CP-140 Case Study, Master's Thesis, Faculty of Engineering, Concordia University, Montreal, Quebec, July 1986.

[19]. T. T. Wu and R. W. P. King,"The Tapered Antenna and Its Application to The Junction Problem for Thin Wires,"*IEEE Trans. Antennas. Propagat.*, Vol. AP-24, no.1, pp 42-45, January 1976.

[20]. R. F. Harrington, Time Harmonic Electromagnetic Fields, McGraw-Hill, Newyork, 1961.

[21]. C. W. Trueman, Wire-Grid Model Construction and Verification Using Programs MESHES, FNDRAD, and

CHECK., Concordia EMC Laboratory, June 1990.

[22]. E. K. Miller and G. J. Burke,"Accuracy-Modellin g Guidelines for Integral-Equation Evaluation of Thin-Wire Scattering Structures,"*IEEE Trans. Antennas Propagat.*, pp 534-536, July 1971.

[23]. E. P. SAYRE,"Junction Discontinuities in Wire Antenna and Scattering Problems,"*IEEE Trans. Antennas Propagat.*, pp 216-218, March 1973.

[24]. H. H. Chao, B. J. Strait and C. D. Taylor,"Radiation and Scattering by Configurations of Bent Wires With Junction," *IEEE Trans. Antennas Propagat.*, Vol. AP-19 p 701, Sept. 1971.

[25]. G. J. Burke," Recent Advances to NEC- Applicati on and Validation," UCRL-100651, Lawrence Livermore National Laboratory, March 3, 1989.

[26]. K. S. H. Lee, L. Marin and J. p. Castillo," Limitation of Wire-Grid Modelling of a Closed Surface," *IEEE Trans. Electromag. Compat.*, Vol. EMC-18, No. 3, pp 123-129, Aug. 1976.

[27]. A. C. Ludwig Wire Grid Modelling of Surfaces," *IEEE Trans. Antennas. Propagat.*, Vol. AP-35, no.9, pp 1045-1048, Sept. 1987.

[28]. A. J. Poggio and E. K. Miller," Integral Equati on Solution of Three-Dimensional scattering Problems," Chapter 4 in *Computer Techniques for Electromagnetics*, Pergaman Press, New York, 197 3.

[29]. D. Gaudine and S. J. Kubina," DIDEC Commands/ Structures/ Installation ," Report no. TN-EMC-8 6-05, Concordia University, Aug. 29, 1986.

[30]. S. Kashyap and M. Dion," An Improved Model-Creation Program for EM Interaction Analysis," Canadian Conference on Electrical and Computer Engineering, Vol. 1, pp 3851-3853, Sept. 1990.

[31]. V. Salvaggio," Development and Test of a Wire-Grid Model of The BELL CH-135 Helicopter," Technical Report Presented to The Department of Electrical Engineering, Concordia University,

Sept. 1985.

[32]. A. C. Ludwig," A Comparison of Spherical Wave Boundary Value Matching Versus Integral Equatio n Scattering Solutions for a Perfectly Conducting Body," *IEEE Trans. Antennas. Propagat.*, Vol. AP-34, no.7, pp 857-865, July 1986.

[33]. G. L. Haller," Aircraft Antennas," *Proc. I.R.E.* , Vol.30, pp 357-362, Aug. 1942.

[34]. G. Sinclair," Theory of Models in Electromagnetic Systems," *Proc. I.R.E.*, pp 1364-1370, Nov. 1948.

[35]. E. D. Sharp, R. L. Tanner," Scale Modelling of High-Frequency Antennas," *IEEE Trans. Antennas. Propagat.*, Communications, pp 810-811, Nov. 196 9.

[36]. G. Sinclair, E. C. Jordan," Measurement of Aircraft-Antenna Patterns Using Models," *Proc. I.R.E.*, pp 1450-1461, Dec. 1947.

[37]. Y. Bahsoun," Evaluation of an HF Helicopter Antenna Measurements and Numerical Techniques," Master's Thesis, Faculty of Engineering, Concordia University, Montreal, Quebec, March 1982.

[38]. IEEE " Test Procedure for Antennas," *IEEE Trans. Antennas. Propagat.*, pp 439-466, May 1965.

[39]. E. C. Jordan, K. G. Balmain," Electromagnetic Waves and Radiating Systems," Prantice Hall, 2n d. Edition, 1968.

[40]. J. Hazell," Modifications to Sinclair Radio Laboratories Model Range Antenna Systems," NRC/ERB-879, Ottawa, April 1973.

[41]. F. Preikschat," Screening Fences for Ground Reflection Reduction," *Microwave Journal*, pp. 4 6-50, Aug. 1964.

[42]. MIL-A-9080 (U.S.A.F.), Military Specification f or Antenna Liaison Communication Equipment, Feb . 1954.

[43]. E. H. Newman, D. M. Pozar," Considerations for

Efficient Wire/Surface Modelling," *IEEE Trans. Antennas. Propagat., vol. AP-28*, No.1, Jan. 198 0.

[44]. G. E. Barker," Measurement of Radiation Patterns of Full-Scale HF and VHF Antennas," *IEEE Trans. Antennas. Propagat., vol. AP-21*, No.4, July 1973.

[45]. H. Jasik," Antenna Engineering Handbook," Mc Gr aw Hill, 1961.

[46]. Y. Bahsoun, S. J. Kubina," A Digital Data Base for the Numerical Calculation of Isotropic Leve l and Radiated power by an Aircraft Antenna," *Concordia University, Layola Campus, EMC Laboratory, TN-EMC-81-06*, Montreal, Aug.1981.

[47]. HF Ccmmunications, Collins-Rockwell Publication, Sept. 1965.

[48]. M. F. Radford," High Frequency Antennas," Chapter 16 in *The Handbook of Antenna Design*, Vol.2, Peregrinus Ltd., London, 1983.

[49]. J. V. Granger," System Consideration in Aircraft Antenna Design," *I.R.E. Trans. on Airborne Elect.*, Vol. AE-1, pp 1-2, Dec. 1951.

[50]. S. J. Kubina," Radiation Characteristics of Vehicle Mounted Antennas and Their Application to Comprehensive System Design," Ph. D. Thesis, Department of Electrical Engineering, Mc Gill University, Montreal, Aug. 1972.

[51]. J. E. Brown," Radiation Pattern Measurements of a Sea-King Loop Aeriel BY Scale Modelling," RAE Technical Report No. 79037, England, 1979.

[52]. Y. Bahsoun and J. Hazell, "Radiation Pattern Measurements of a Tranline Antenna on a Scale Model of CHSS-2 Sea-King Helicopter," ERB-929, NRCCNO. 18883, Ottawa, Dec. 1980.

[53]. S. J. Kubina," Study on Electromagnetic analysis Techniques for Aircraft Antennas" Technical note no. TN-EMC-85-02, Dec. 1984.

[54]. R. E. Collin, Antennas and Radio Wave Propagation, McGrow-Hill, NewYork, 1985.

[55]. D. T. Paris, F. K. Hurd, Basic Electromagnetic Theory, McGraw Hill, 1969.

[56]. J. C. Ratio," Refletion Coefficient Analysis of The Effect of Ground on Antenna Pattern," *IEEE Trans. Antennas. Propagat. Newslatter*, pp 5-11, Feb.1987.

[57]. C. E. Smith," Impedance-Measuring Instrument," *proc. of I.R.E.*, pp 362-364, Aug.1942.

[58]. "IRE Standards on Antennas And Waveguides: Waveguide And Waveguide Component Measurements," *IEEE No. 148*, 1959.

[59]. C. R. Paul and S. A. Naser, Introduction To Electromagnetic Fields, 2nd. Edition, McGraw Hill, 1987.

[60]. J. V. N. Granger, T. Morita," Radio-Frequency Current Distribution on Aircraft Structures," *proc. of I.R.E.*, pp 932-939, Aug.1951.

[61]. G. A. Haller," Aircraft Antennas," *proc. of I.R.E.*, pp 357-362, Aug.1942.

[62]. J. V. N. Granger, J. T. Bolljahn," Aircraft Antennas," *proc. of I.R.E.*, pp 533-550, May 1955.

[63]. J. D. Krauss, Antennas, McGraw Hill, NewYork, 1950.

[64]. J. R. Wait, Antennas And Propagation, Peregrinus Ltd. London, 1986.

[65]. J. W. R. Cox , G. Vongas," Calculated and Measured Radiation Characteristics of an HF Loop Antenna Mounted Upon a Helicopter," **********

[66]. J. Y. Wong and C. A. Muilwyk," Rotor Modulation Studies of an HF Wire Antenna For the CHSS-2 Helicopter," *NRC Report ERB-710*, July, 1965.

[67]. J. I. R. Owen," Wire Grid Modelling of Helicopter HF Arials," *IEEE Trans. Antennas. Propagat., vol. AP-18-10*, pp 792-795, 1980.

[68]. S. R. Seshardi, Fundamentals of Transmission Lines And Electromagnetic Fields, Addison-Wesley,

1971.

[69]. S. J. Kubina and S. Esfandiari," Models for Performance Assessments of HF antennas on the CH-135/Twin Huey Helicopter,"Canadian Conference on Electrical and Computer Engineering, Vol. 1, pp 3851-3853, Sept. 1990.

[70]. A. Sommerfeld, Partial Differential Equations in Physics, Academic Press, NewYork, 1964.

[71]. E. K. Miller, A. J. Poggio, G. J. Burk, E. S. Seldon," Analysis of Wire Antenna in the Presence of a Conducting Half-Space. Part I: The Vertical Antenna in Free Space, *Canadian Journal of Physics*. Vol. 50, pp 879-888, 1972.

[72]. E. K. Miller, A. J. Poggio, G. J. Burk, E. S. Seldon," Analysis of Wire Antenna in the Presence of a Conducting Half-Space. Part II: The Horizontal Antenna in Free Space, *Canadian Journal of Physics*. Vol. 50, pp 2614-2627, 1972.